AD-A043 486 MATHEMATICAL SCIENCES NORTHWEST INC BELLEVUE WASH F/G 20/9
LASER HEATING OF MAGNETICALLY CONFINED PLASMAS FOR X-RAY PRODUC--ETC(U)
APR 76 A L HOFFMAN, E A CRAWFORD DNA001-74-C-0006
UNCLASSIFIED MSNW-76-130-1 DNA-3963F NL

1 OF 2
AD A043486



AD A043486

DNA 3963F

LASER HEATING OF MAGNETICALLY CONFINED PLASMAS FOR X-RAY PRODUCTION

Phase III

Mathematical Sciences Northwest, Inc.
P.O. Box 1887
Bellevue, Washington 98009

April 1976

Final Report

CONTRACT No. DNA 001-74-C- 0006

APPROVED FOR PUBLIC RELEASE;
DISTRIBUTION UNLIMITED.

THIS WORK SPONSORED BY THE DEFENSE NUCLEAR AGENCY
UNDER RDT&E RMSS CODE B324074464 W99QAXPF00128 H2590D.

AU NO.
DDC FILE COPY

Prepared for
Director
DEFENSE NUCLEAR AGENCY
Washington, D. C. 20305

DDC
RECEIVED
AUG 29 1977
A

Destroy this report when it is no longer
needed. Do not return to sender.



UNCLASSIFIED

SECURITY CLASSIFICATION OF THIS PAGE (When Data Entered)

REPORT DOCUMENTATION PAGE

READ INSTRUCTIONS BEFORE COMPLETING FORM

1. REPORT NUMBER: DNA 3963F
2. GOVT ACCESSION NO.
3. RECIPIENT'S CATALOG NUMBER

4. TITLE (and Subtitle): LASER HEATING OF MAGNETICALLY CONFINED PLASMAS FOR X-RAY PRODUCTION. Phase III

5. TYPE OF REPORT & PERIOD COVERED: Final Report, on Phase 3,

6. PERFORMING ORG. REPORT NUMBER: MSNW 76-130-1

7. AUTHOR(s): Alan L. Hoffman, Edward A. Crawford

8. CONTRACT OR GRANT NUMBER(s): DNA 001-74-C-0006

9. PERFORMING ORGANIZATION NAME AND ADDRESS: Mathematical Sciences Northwest, Inc., P.O. Box 1887, Bellevue, Washington 98009

10. PROGRAM ELEMENT, PROJECT, TASK AREA & WORK UNIT NUMBERS: Subtask W99QAXPF001-28

11. CONTROLLING OFFICE NAME AND ADDRESS: Director, Defense Nuclear Agency, Washington, D.C. 20305

12. REPORT DATE: April 1976

13. NUMBER OF PAGES: 176 (12) 174 p.

14. MONITORING AGENCY NAME & ADDRESS (if different from Controlling Office)

15. SECURITY CLASS (of this report): UNCLASSIFIED

15a. DECLASSIFICATION/DOWNGRADING SCHEDULE

16. DISTRIBUTION STATEMENT (of this Report)

Approved for public release; distribution unlimited.

17. DISTRIBUTION STATEMENT (of the abstract entered in Block 20, if different from Report)

18. SUPPLEMENTARY NOTES

This work sponsored by the Defense Nuclear Agency under RDT&E RMSS Code B324074464 W99QAXPF00128 H2590D.

19. KEY WORDS (Continue on reverse side if necessary and identify by block number)

Laser Heated Magnetically Confined Plasma
Soft X-Ray Production
Gain Switched CO_2 Laser
High Field Fast Solenoid

20. ABSTRACT (Continue on reverse side if necessary and identify by block number)

Quantitative experiments ~~have been~~ were carried out on laser heating magnetically confined neon and krypton plasma columns. Approximately 100 J in 50 nsec and up to 300 J in 500 nsec of 10.6 micrometers radiation ~~has been~~ was used to heat 5 mm diameter plasmas at $10^{18}/cm^3$ electron densities to up to 200 eV electron temperatures. Intense soft radiation during the ionization process has limited heating wave propagation into the plasma column to a few centimeters, and restricted the 1 keV K-shell emission from He-like neon to several MW. A detailed hydrodynamic and atomic physics program developed for this project → next page

DD FORM 1473 JAN 73 EDITION OF 1 NOV 65 IS OBSOLETE

UNCLASSIFIED

SECURITY CLASSIFICATION OF THIS PAGE (When Data Entered)

10 to the 18th power/cc

404 058

20. ABSTRACT (Continued)

cont.

gives excellent agreement with the observed radiation levels. Approximately 10% ~~percent~~ conversion efficiencies of laser energies to 2 keV x-radiation are predicted at the highest conventional magnetic fields and 1 kJ laser energies.

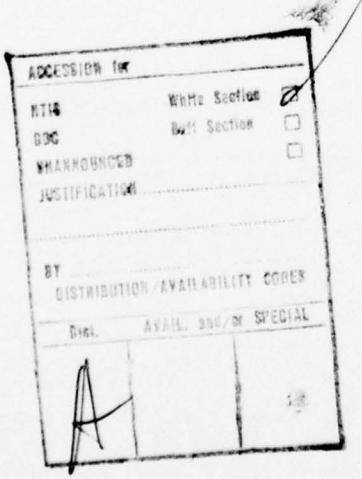


TABLE OF CONTENTS

SECTION		PAGE
I	INTRODUCTION AND CONCLUSIONS	7
II	TEMPERATURE SCALING AND PLASMA LOSSES	9
	1. Plasma Configuration and Laser Intensity	9
	2. Typical Example of Experimental Conditions	13
	3. Plasma Losses	13
	4. Dilution in Low-z Gases	15
III	NUMERICAL CALCULATIONS	19
	1. HOFNEX - Radial Heat Transfer Modification	19
	2. HIRAD	23
	3. Neon Calculations	37
	4. He-like X-ray Conversion Efficiency	50
	5. Krypton Calculations	52
IV	THETA PINCH OPERATION	60
V	HIGH FIELD SOLENOID OPERATION	66
	1. Design of Fast Solenoid	66
	2. Modification of Capacitor Bank	68
	3. Fast Solenoid Performance	69
	4. Summary of Pinch Bank Performance with Various Loads	73
	5. Plasma Production in Fast Solenoid	75
VI	LASER OPERATION	79
	1. Quasi-Steady Performance	79
	2. Oscillator-Amplifier Experiments	81

SECTION		PAGE
VII	LASER HEATING EXPERIMENTS IN THE THETA PINCH	87
	1. Phase III Modifications	87
	2. Neon Line Radiation Using Gain Switched Longer Spikes	94
	3. Long Time Scale Laser Heating	106
	4. Low Z Dilution Effects	110
	5. Backscatter Investigation	111
VIII	LASER HEATING EXPERIMENTS IN THE FAST SOLENOID	118
	1. Holographic Interferometry of Laser Heated Neon and Krypton in the Fast Solenoid	118
	2. X-Ray Emission from Laser Heated Krypton Plasmas in Fast Solenoid	121
	3. Laser Heating of Neon Plasma in the Fast Solenoid	125
	4. Time Integrated Neon X-Ray Spectrums	129
LIST OF REFERENCES		138
APPENDIX		141

LIST OF FIGURES

FIGURE		PAGE
2.1	Basic Laser Heated Magnetically Confined Plasma Configurations	10
2.2	Scaling Parameters for 8 Times Ionized Neon Ions in Low z Diluents	16
2.3	Scaling Parameters for 26 Times Ionized Krypton Ions in Low z Diluents	17
3.1	Rates of Excitation, Deexcitation, and Ionization for Li-Like Neon	28
3.2	Average Gaunt Factors for Oxygen and Nitrogen Excitations	30
3.3	Radiation Limits Based on Excitation Rates, Radiation Rates, and Black Body Rate	35
3.4	Electron Impact Excitation Rate Coefficients for OVII	36
3.5	Time History of Neon Plasma Irradiated by 1 GW CO_2 Laser	40
3.6	Calculated Temperatures and X-Ray Emission Profiles after Laser Heat Addition to Neon Plasma for Various Loss Mechanisms	43
3.7	Calculated Temperature and X-Ray Emission Profiles for Neon Plasmas after 60 nsec Laser Irradiation	45
3.8	Calculated Neon Temperature and Radiation Profiles at Various Times	47
3.9	Numerical Simulation of Laser Heated Neon Experiment	48
3.10	20 nsec - 1 kJ Laser Heating of 10 cm Krypton Column	55
3.11	80 nsec - 1 kJ Laser Heating of 7 cm Krypton Column	56
3.12	Numerical Simulation of Laser Heated Krypton Experiment	58

FIGURE		PAGE
4.1	Theta Pinch Performance with 10 cm x 3.3 cm Diameter and 7 cm x 3.3 cm Diameter Coils	61
4.2	Comparison of Experimental Theta Pinch Waveform with Result Computed Using Time Dependent Resistance	63
4.3	Field Profile of Modified Theta Pinch; C = 9 μV	65
5.1a	Perspective Drawing of Fast Solenoid Including Urethane Envelope	67
5.1b	Drawing of Helical Conductor of Steel for Fast Solenoid	67
5.2	Schematic of Capacitor Bank and Clamp Circuit for Fast Solenoid	70
5.3	Field Profile of Fast Solenoid; C = 9 μf (12 Capacitors)	72
5.4	Unheated Electron Density Profiles at Various Times, Fast Solenoid, 60 kV, 1.4 cm Diameter Plasma Tube	77
6.1	Laser Performance in Tail of Pulse with 3/½/1 Mix	80
6.2a	Schematic of Oscillator-Amplifier System Showing Calorimeter Positions	83
6.2b	Histogram of Fraction of Oscillator Energy Recovered at Various Positions, Amplifier Inactive	83
6.3	Large and Small Signal Gain Characteristics of Amplifier	85
7.1	Silicon PIN Detector X-Ray Diagnostics, (a) Mechanical Assembly, (b) Electrical Schematic	89
7.2a	Sensitivity of Silicon PIN X-Ray Detector	91
7.2b	Transmission of X-Ray Filter Foils	91
7.3	Experiment for Laser Heating of Solid Metal Targets	93
7.4	Peak K-Shell X-Ray Output Power on First Spike as a Function of Magnetic Field at Time of Laser Spike	95

FIGURE		PAGE
7.5	Theoretical and Experimental K-Shell Radiation on First and Second Laser Spikes Irradiating Neon Theta Pinch B_{max} = 100 kG, Fill Pressure 1.2 Torr	100
7.6	Experiment Showing Propagation of Hot Region	105
7.7	Results of Slow Laser Heating Experiment; 3/0.5/1 Mix in Laser; 1.2 Torr Ne in Pinch	107
7.8	Comparison of Theory and Experiment for Laser Heated Neon Theta Pinch Plasma	109
7.9	Result of Slow Laser Heating Experiment on Helium Diluted Neon 0.25 Fraction Neon at Various Fill Pressures; Laser First Spike Energy 65 J, 3/0.5/1 Mix, Pinch B_o = 100 kG	112
7.10	Experimental Setup for Time Resolved Backscatter Diagnostics	113
7.11	Experimental Setup for Spectral Resolution of Backscattered CO_2 Laser Radiation	116
8.1	Neon Density Profiles in Fast Solenoid	119
8.2	Krypton Density Profiles in Fast Solenoid	120
8.3a	Typical Waveforms in Krypton Heating Experiment in Fast Solenoid	123
8.3b	Typical Waveforms in Neon Heating Experiment in Fast Solenoid	124
3.8c	Burn Patterns 12 Inches Behind Laser Vacuum Focus	124
8.4a	Variation of X-Ray Output Energy with Initial Fill Pressure of Neon, B_o, E_{laser} Approximately Constant	128
8.4b	Variation of X-Ray Output Power with Magnetic Field at Time of Laser Firing	128
8.5	Setup of SRI Double Bent Crystal Spectrometer on Fast Solenoid Pinch	132
8.6	Densitometer Tracing of Neon Spectrum with Tentative Identification of Spectral Lines	134
8.7	Theoretical Calibration of KAP Bent Crystal Spectrograph in Near Film Plane	135

LIST OF TABLES

TABLE		PAGE
3.1	Neon Energy Levels and f Numbers	25
3.2	Atomic Data for Neon (VIII)	27
3.3	Gaunt Factor Multiplication Factors - R_g	31
3.4	Atomic Data Used in HIRAD for Neon	38
3.5	Atomic Data Used in HIRAD for Krypton	53
5.1	Performance Characteristics of Theta Pinch Bank with Various Loads	74
7.1	Possible Contributions to XRD Signal Behind Thin Foils at T_e = 0.16 keV	99
8.1	Foil Transmission Intensity Ratios for Krypton Plasma	122
8.2	Ne IX Allowed Transitions	136

SECTION I

INTRODUCTION AND CONCLUSIONS

In the previous two years of the Mathematical Sciences Northwest, Inc. (MSNW) program for DNA, laser heating of magnetically confined plasma columns was demonstrated and moderate Z gases (neon) were stripped down to helium-like configurations. A heating wave program was also developed to model the laser propagation, plasma heating, and magnetohydrodynamics, and atomic physics. In this third phase (third year of work) detailed experiments were conducted using pure neon, neon-helium mixes, and pure krypton plasmas. The numerical program was also significantly improved to use tabulated atomic transition data and excitation rates. Very high threshold energies were found for the neon plasmas, both theoretically and experimentally, before K-shell radiation was produced. Approximately 10 times the energy invested in ionization was lost to soft radiation during the ionization. This factor, coupled with the low laser energies available (several hundred joules) limited the neon conversion efficiencies to a few percent.

Calculations with the new improved code were made for higher Z, neon-like radiators. At high laser powers and magnetic fields conversion efficiencies to x-rays in the 2 keV range were about 10 percent. At lower laser intensities the conversion efficiency is limited by intense soft radiation emitted during the ionization process, and hence a high threshold energy to be overcome before the desired final highly stripped ion conditions were achieved. At higher laser intensities the collisional excitation rates themselves set a limit on the conversion efficiency since end losses are competitive cooling processes with radiation. The calculated conversion efficiency depends on approximate atomic physics, and could

possibly increase by a factor of 2, but the energy range is limited by the solenoidal magnetic field strengths physically achievable.

Section II of this report develops the approximate temperature and radiation scaling with magnetic field and laser energy. The detailed code modifications are described in Section III along with sample calculations for neon and krypton. Section IV describes modifications to the theta pinch to obtain higher fields, and Section V describes the development of a fast solenoid used to obtain up to 200 kG fields. In Section VI the laser performance is discussed in the "long pulse" mode found necessary to surpass the radiation threshold energies, and the attempts at oscillator-amplifier development are described. Section VII contains the detailed x-ray measurements of heated neon plasmas in the theta pinch, and Section VIII describes similar experiments in the fast solenoid for neon and krypton plasmas.

SECTION II

TEMPERATURE SCALING AND PLASMA LOSSES

1. Plasma Configuration and Laser Absorption

The basic plasma configurations used in the present work are shown schematically in Figure 2.1. An axial magnetic field was used to confine the plasma in the radial direction, and also to provide some axial containment through self-mirroring effects. The plasma can be preformed by rapidly rising magnetic fields, as in the theta pinch, or formed entirely by the laser, as indicated for the solenoid. Actually, in the experiments at high fill pressures, in either the theta pinch or solenoid, the magnetic field rose rapidly enough to form a weakly compressed, low temperature, high density plasma.

A rough plasma temperature can be arrived at by integrating the simple laser absorption equation

$$\frac{5}{2} N_T k \frac{\partial T_e}{\partial t} = \frac{P}{\ell_{abs}} \tag{2.1}$$

assuming a constant pressure balance with the magnetic field where P is the laser power, ℓ_{abs} the laser absorption length, and N_T the total plasma line density (particles/cm),

$$N_T = (1 + z)N_p \tag{2.2}$$

where N_p is the ion line density and z the average ion charge.

Two simple scaling models can be used. The first assumes N_p = constant, as would be the case in the theta pinch when all the plasma was heated by the laser (either directly or through radial heat conduction). The second model assumes the laser intensity is constant and $N_T = n_T A$, where

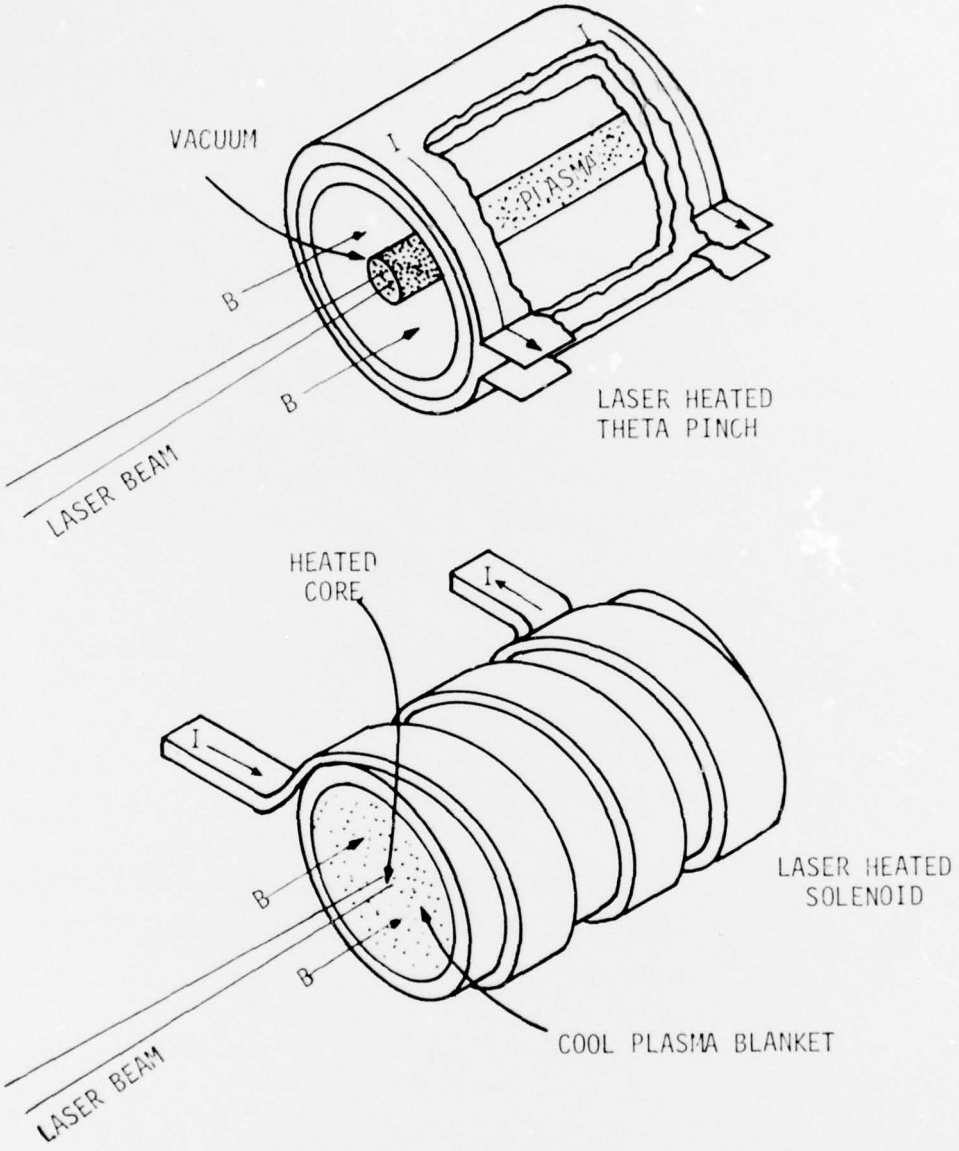


Figure 2.1. Basic Laser Heated Magnetically Confined Plasma Configurations

76 00182

n_T is the total plasma density and A is the area of the laser beam. In each case, pressure balance is assumed,

$$\bar{n}_T(10^{18}/cm^3)T_e(keV) = 0.25\ \beta B^2(100\ kG) \tag{2.3}$$

with β being the ratio of plasma pressure to confining magnetic pressure. The laser absorption length for 10.6 μ radiation is approximately

$$\ell_{abs} = 300\ \frac{T_e^{3/2}}{z^*\bar{n}_e^2}\ cm \tag{2.4}$$

where T_e is given in keV, $\bar{n}_e$ is in units of $10^{18}/cm^3$, and z^* is defined as

$$z^* = \frac{\Sigma n_i z_i^2}{\Sigma n_i z_i} = \frac{\bar{z^2}}{\bar{z}} \tag{2.5}$$

Using Equation (2.3), the absorption length has the form

$$\ell_{abs} = 4800\ \frac{(1 + \frac{1}{z})^2\ T_e^{7/2}}{z^*\beta^2\ B^4}\ cm \tag{2.6}$$

with B in units of 100 kG. In all of the above formulas, it has been assumed that $T_i = T_e$. For short times (O(10 to 100 nsec)) this may not be so; if $T_i << T_e$, the 1/z term can be dropped.

A straightforward integration of Equation (2.1), using Equation (2.6), yields constant line density heating,

$$T_e = 0.257\ \left\{\frac{\beta^2\ z^*}{(1 + \frac{1}{z})^2}\right\}^{2/9}\ B^{8/9}\left\{\frac{\varepsilon_{laser}}{\bar{N}_T}\right\}^{2/9}\ keV \tag{2.7}$$

where ε_{laser} is the incident laser energy in kilojoules, and $\bar{N}_T$ is the particle line density in units of $10^{18}/cm$. The second scaling model with I = P/A yields constant area heating,

$$T_e = 0.242 \left\{ \frac{\beta\, z^*}{(1 + \frac{1}{z})^2} \right\}^{2/7} B^{4/7} \left\{ \frac{\varepsilon_{laser}}{A} \right\}^{2/7} \text{ keV} \qquad (2.8)$$

with the laser beam and heated plasma area A given in cm^2. In this case, the plasma temperature rises less rapidly with magnetic field since the line density contained in A increases with increasing magnetic pressure. In fact, if the substitution $A = N_T/n_T = N_T/(0.25\ \beta B^2/T_e)$ is made in Equation (2.8), the same scaling as given by Equation (2.7) results in <u>constant area heating</u>,

$$T_e = 0.244 \left\{ \frac{\beta^2\, z^*}{(1 + \frac{1}{z})^2} \right\}^{2/9} B^{8/9} \left\{ \frac{\varepsilon_{laser}}{\bar{N}_T} \right\}^{2/9} \text{ keV} \qquad (2.9)$$

with only slightly lower temperature due to the fact that the same laser energy heated more particles in the early heating phase when $\bar{N}_T$ was larger.

The exact form of the heating, whether constant area or constant line density (the area A of the laser beam is assumed to increase as the plasma column expands), is seen to be of minor importance, but the final heated area A, or heated line density $\bar{N}_T$ is critically important. The ideal plasma temperature reached depends only on the laser intensity to the 2/7 power, but the absorption length, or heated column length, is nearly linearly dependent on intensity. Of even greater importance, as will be seen when radiation losses are considered, the heating rate at a given temperature is linearly dependent on intensity.

In all the experiments, a 10 cm diameter annular laser beam was focussed by a 1.5 m focal length mirror onto the front of a plasma column with an initial diameter between 6 and 9 mm, depending on the initial fill pressure. The laser focal spot was about 2 mm in diameter, but in all cases, the heated portion of the plasma column, as measured inteferometrically was about 5 mm in diameter. This was due to plasma expansion and laser beam refraction within the density minimum created by the expansion.

In order to obtain the temperatures given by Equations (2.7) through (2.9), it is necessary that the initial density be high enough so that upon plasma expansion the final densities given by pressure balance (Equation (2.3)) can be achieved. Since at these high densities the initial plasma beta, even in a fast theta pinch, is very low, the initial ion density should be at least twice the desired final ion density in order to achieve a final plasma beta of at least 0.75. In the experiments described in this report, final densities of about $10^{18}/cm^3$ were desired. In 8 times ionized neon, this means ion densities of about $10^{17}/cm^3$, so that initial ion densities of at least $2 \times 10^{17}/cm^3$ were required. These densities could be provided in a theta pinch with about a one torr filling pressure and a density compression of at least six.

2. Typical Example of Experimental Conditions

A typical example of experimental conditions involves heating a 5 mm diameter neon column with 100 J of laser energy in a 100 to 200 kG magnetic field. Assuming a plasma beta of 0.75 and $z = z^* = 8$, Equation (2.8) yields $T_e = 320$ eV at 100 kG and $T_e = 475$ eV at 200 kG. The ability to reach these conditions, however, depends on the plasma losses.

3. Plasma Losses

An exact form of the electron energy equation, assuming a constant ion line density N_p, can be written

$$\frac{\partial}{\partial t}\left(\frac{3}{2} N_e k T_e\right) + p_e \frac{\partial A}{\partial t} = \frac{P}{\ell_{abs}} - \frac{\partial}{\partial t}\left(N_p \varepsilon_{ion}\right)$$

$$- N_p P_{rad} - \frac{3}{2} N_e k \frac{(T_e - T_i)}{\tau_{ei}} - A \frac{\partial q_{\parallel}}{\partial x} - 2\pi r q_{\perp} \qquad (2.10)$$

The electron line density N_e is equal to z times the ion line density, p_e is the electron pressure, ε_{ion} is the total ionization energy per ion, P_{rad} is the radiation rate per ion, τ_{ei} is the electron-ion equilibration time, and $q_{\parallel}$ and $q_{\perp}$ are the parallel and perpendicular heat transfer rates,

respectively. In order to heat the plasma, the power absorption term P/ℓ_{abs} must exceed the remaining loss terms on the right-hand side of Equation (2.10). The most serious losses are those due to initial rapid radiation at lower levels of ionization. Since this radiation occurs at relatively low temperatures, there is little plasma expansion and the process occurs at near constant ion density. It is thus instructive to write the absorption rate as

$$\frac{P}{\ell_{abs}} = 0.0033 \frac{\bar{n}_e z z^*}{T_e^{3/2}} I(\mathrm{Gw/cm^2})\ \bar{N}_p \quad \mathrm{Gw/cm} \tag{2.11}$$

This is just a simple statement of the Coulomb cross-section for "quivering" electrons colliding with ions to absorb the quiver energy of their vibration in the laser electric field.

The plasmas produced by the laser heating are best described by a Coronal model, so that the radiation is given by the electron collisional excitation rate. The radiated power, as will be discussed in detail in Section III, has the form

$$P_{rad} \propto \frac{\bar{n}_e \chi}{T_e^{3/2}} \left\{ \left(\frac{T_e}{\chi}\right) e^{-\chi/T_e} \right\} \bar{N}_p \tag{2.12}$$

where χ is a typical radiation energy. For radiation characteristic of the desired final condition when $T_e \simeq \chi = O(z^2)$, Equation (2.12) has the same functional form as the absorption rate. For those conditions, the laser absorption rate can easily be made to exceed the radiation rate. However, during the initial heating stages, T_e/χ may be very high, especially for $2s^2 2p^n \rightarrow 2s2p^{n+1}$ resonance excitation. This fact, coupled with high f numbers and Gaunt factors, can place stringent requirements on the laser intensity. Fortunately, self-absorption of this resonance radiation tends to alleviate the problem.

Besides the requirement of high laser intensity, there is also a requirement on a threshold energy to reach the desired plasma temperature and ionization state. This can be seen on integrating the significant terms in Equation (2.10),

$$\varepsilon_{threshold} \simeq (\frac{3}{2} zkT_e + \varepsilon_{ion})N_p + \int_o^{\tau_{ioniz}} (N_p P_{rad} + 2\pi r q_\perp)dt \quad (2.13)$$

The first term is just the plasma energy, which is the desirable quantity. ε_{ion} is always much less than $\frac{3}{2} zkT_e$ for highly ionized ions, since only the last few electrons take energies of the order of kT_e to strip off. The significant energies are those represented by the integral in Equation (2.13). The energy radiated during the ionization process can be many times the corresponding ionization energy. The energy lost by radial heat transfer can also be significant for small plasma columns. These threshold energies are discussed in detail in Section III, and are extremely evident in the experiments performed.

4. Dilution in Low-z Gases

It can be seen from Equation (2.9) that the ideal plasma temperature (no losses) depends on the quantity $\{z^*/(1 + 1/z)^2\}^{2/9}$. This quantity, along with z and z* is plotted in Figures 2.2 and 2.3 for neon and krypton diluted in hydrogen and helium. Neon is assumed ionized to a helium-like configuration and krypton to a neon-like configuration. If radiative losses were not a limiting factor on achievable temperature, it would be desirable to maximize $\{z^*/(1 + 1/z)^2\}^{2/9}$ by using pure high-z gases.

When radiative losses are significant, it might be thought that dilution with a low-z gas could result in higher temperatures by reducing radiation losses. Calling fN_p the number of high z ions, the radiation rate given by Equation (2.12) is seen to be

$$P_{rad} \propto \frac{1}{\sqrt{T_e}} \; e^{-\chi/T_e} \left\{ \frac{f}{z(1 + \frac{1}{z})^2} \right\} \bar{n}_T \bar{N}_T \quad (2.14)$$

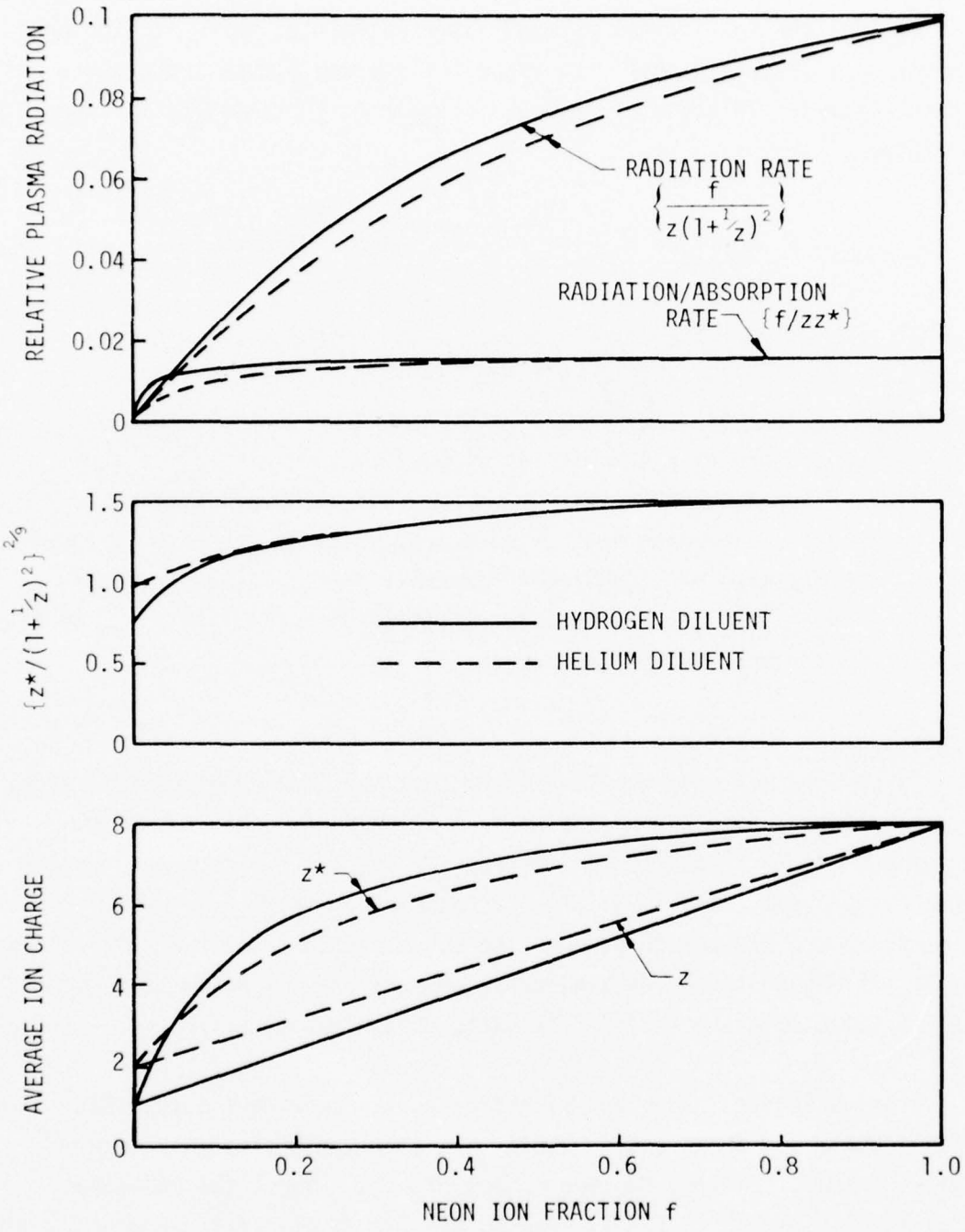


Figure 2.2. Scaling Parameters for 8 Times Ionized Neon Ions in Low z Diluents

76 00183

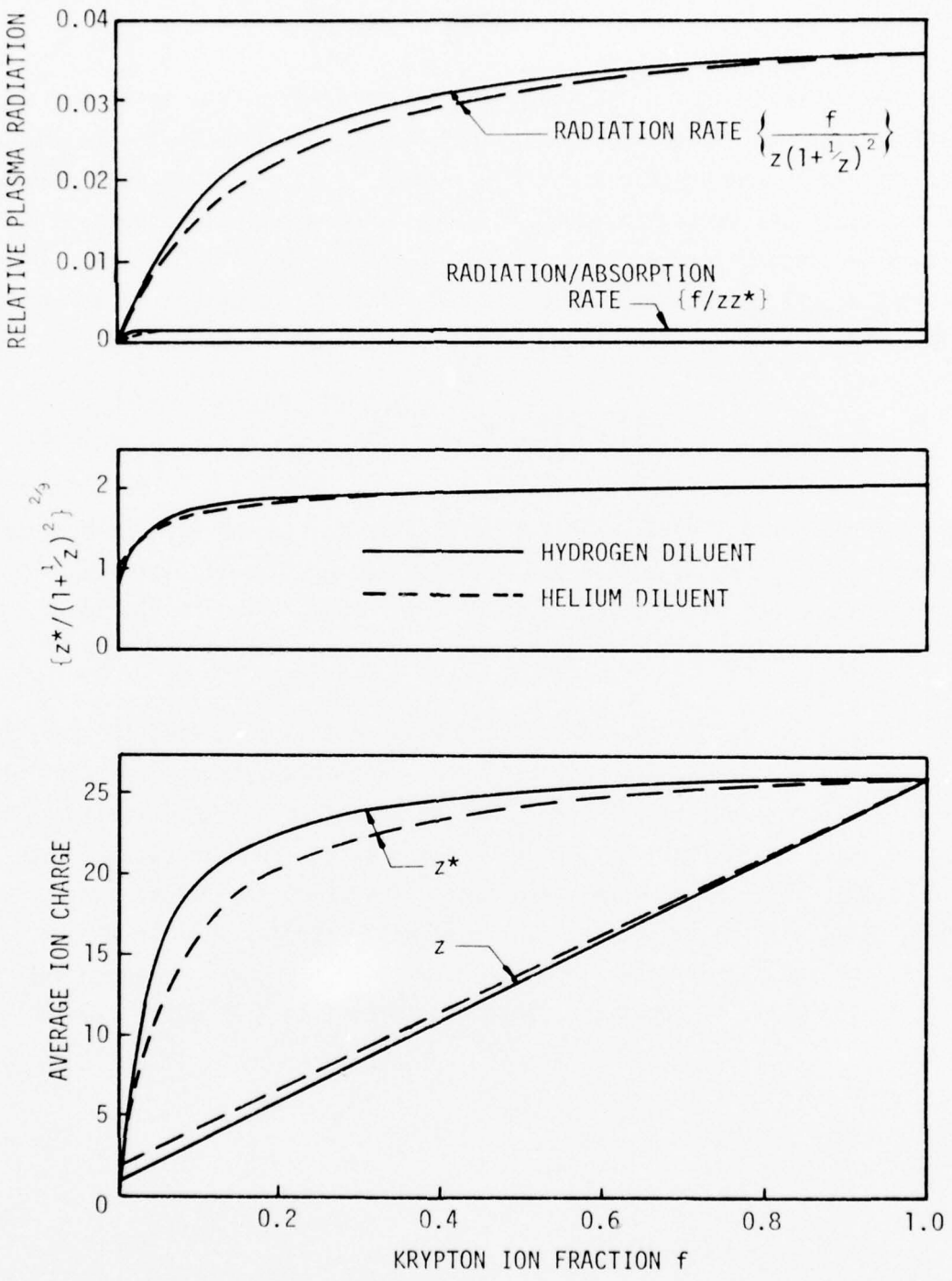


Figure 2.3. Scaling Parameters for 26 Times Ionized Krypton Ions in Low z Diluents

76 00184

with the electron and ion densities written in terms of the total particle densities. For a constant particle density, the effect of dilution is contained in the bracketed quantity, which is also plotted in Figures 2.2 and 2.3. The radiation rate, of course, decreases with dilution, but so does the absorption rate, due to the $\overline{z^2}$ term in Equation (2.11). The ratio of P_{abs}/P_{rad} is simply given by the ratios of Equations (2.12) and (2.11), as

$$\frac{P_{rad}}{P_{abs}} \propto \left\{\frac{f}{zz^*}\right\} T_e \, e^{-\chi/T_e} \tag{2.15}$$

The bracketed quantity $\{f/zz^*\}$ is also plotted in Figures 2.2 and 2.3, and is seen to be unchanged unless the dilution is very great. This is true because the principal contributor to $\overline{z^2} = (1 - f)z_0^2 + fz_1^2$ is the heavy ion for z_1 large.

The exact effect of changing the heavy ion is difficult to predict from scaling arguments. Certainly, higher ideal temperatures are possible due to the $\{z^*/(1 + 1/z)^2\}^{2/9}$ term. For temperatures characteristic of the desired state of ionization z, z^2 will scale as T_e, and the ratio in Equation (2.15) will remain roughly constant. The exact ionization and excitation rates will be important. The threshold energies will be higher for high-z ions and higher laser intensities will be necessary. Higher magnetic fields will, of course, be required to contain the hotter plasmas.

SECTION III

NUMERICAL CALCULATIONS

1. HOFNEX - Radial Heat Transfer and Absorption Coefficient Modifications

The details of the HOFNEX code are given in the previous report "Laser Heating of Magnetically Confined Plasmas for x-Ray Production - Phase II".[1] The basic properties are listed below for reference:

a) one-dimensional (longitudinal), time dependent;
b) laser beam always fills plasma column (constant N_p);
c) classical inverse Bremsstrahlung laser absorption;
d) instantaneous radial pressure equilibration with external magnetic field;
e) no longitudinal motion except for inward propagating area waves at ends;
f) arbitrary initial beta and no magnetic field diffusion (constant $\psi = n_e/B$);
g) ionization, recombination, and radiation given by subroutine HIRAD;
h) classical electron-ion temperature equilibration;
i) classical thermal heat conduction along field lines with flux limited heat conduction at column ends; and
j) cross-section averaged radial cross-field electron heat conduction.

Extensive modifications have been made to the HIRAD subroutine. These modifications to improve the atomic physics are the most significant changes in the HOFNEX calculations, and are described fully in the following subsection. A minor change to HOFNEX was to redefine the speed of the inward propagating area wave as an empirical factor AREDFCT times the acoustic speed,

$$V_{area} = 0.04 \text{ AREDFCT } \sqrt{(T_i + zT_e)/A_i} \quad \text{cm/nsec} \qquad (3.1)$$

where A_i is the average (for gas mixtures) atomic weight. Self-mirroring reduces AREDFCT to about a value of 0.5, and this is observed experimentally.

Inclusion of more accurate atomic physics in HOFNEX led to good enough numerical modeling of experimental results that it was desirable to include a more accurate description of the absorption coefficient than that given by equation (2.4). Johnston and Dawson[2] give an expression for the absorption coefficient as

$$K = \frac{2.5 \times 10^{-3} \, z \, \bar{n}_e^{\,2} \, (10^{18}/\text{cm}^3)}{\nu^2 (10^{13} \text{ sec}^{-1}) \, T_e^{3/2} \text{ (kev)}} \quad \frac{\ell n \, \Lambda \, (\nu)}{(1 - 0.8 \, \bar{n}_e/\nu^2 \, (10^{13} \text{ sec}^{-1}))^{1/2}} \text{ cm}^{-1} \qquad (3.2)$$

where ν is the laser frequency (2.83×10^{13} sec^{-1} for 10.6μ CO_2 radiation) and Λ is given by

$$\Lambda(\nu = 2.83 \times 10^{13} \text{ sec}^{-1}) = \text{minimum of} \begin{cases} 2.6 \, T_e^{3/2} \text{ (eV)}/Z \\ 13.5 \, T_e \text{(eV)} \end{cases} \qquad (3.3)$$

For 10.6 μ radiation and $n_e = 10^{18}/\text{cm}^3$ the square root factor in the absorption coefficient is negligible and Equation (3.2) reduces (when inverted) to Equation (2.4) under the stipulation that $\ell n \, \Lambda = 10$. This is seen to be a poor assumption for high Z ions at moderate temperatures. For typical low temperature final conditions of T_e = 150 eV and Z = 8, $\ell n \, \Lambda = 6.4$ and the absorption length is 56 percent longer than shown in Equation (2.4), with this higher value reflected in the subsequent scaling. At the very beginning of the laser heating

when T_e is low (typically 10 eV, and Z = 2 to 3) $\ell n\ \Lambda$ is even lower and the plasma heating less rapid. This increases the threshold energy required to ionize the plasma to a final desired complete shell configuration. The absorption coefficient given by Equations (3.2) and (3.3) were incorporated in HOFNEX and are reflected in the calculations presented in this report.

A last fundamental change to HOFNEX was the inclusion of radial heat conduction, since in all cases only the central portion of the initial plasma column is heated. The diffusion parameters for electrons and ions were given in Reference 1 as

$$\text{electrons:}\quad D_{\parallel e} = 4.6 \times 10^9\ T_e^{5/2}/(\bar{n}_e + z_i^2\ \bar{n}_i)\ \text{cm}^2/\text{sec} \qquad (3.4)$$

$$\text{ions:}\quad D_{\parallel i} = 1.1 \times 10^7\ T_i^{5/2}/z_i^4\ \bar{n}_i\ \text{cm}^2/\text{sec} \qquad (3.5)$$

For cross-field conduction, these values must be divided by $1 + (\omega\tau)^2$, where $\omega\tau$ is the ratio of the mean free path to the gyro radius,

$$\text{electrons:}\quad \omega_{c_e}\tau_e = 1.8 \times 10^3\ T_e^{3/2}\ B(100\ \text{kG})/(\bar{n}_e + z_i^2\ \bar{n}_i) \qquad (3.6)$$

$$\text{ions:}\quad \omega_{c_i}\tau_i = 4.4\ T_i^{3/2}\ B(100\ \text{kG})/\sqrt{A_i}\ z_i^3\ \bar{n}_i \qquad (3.7)$$

Typical values of these parameters for the conditions of $T_e = T_i = 0.15$ keV, $\bar{n}_e = 1$, $\bar{n}_i = 0.125$, $z_i = 8$, and B = 100 kG are:

$D_{\parallel e} = 4.5 \times 10^6$ cm^2/sec $\qquad$ $\omega_{c_e}\tau_e = 11.6$

$D_{\parallel i} = 2.3 \times 10^2$ cm^2/sec $\qquad$ $\omega_{c_i}\tau_i = 0.011$

$$D_{\perp e} \simeq 3.3 \times 10^4 \text{ cm}^2/\text{sec}$$

$$D_{\perp i} \simeq 2.3 \times 10^2 \text{ cm}^2/\text{sec}$$

It can be seen that, in contrast to the case when $\omega_{c_i}\tau_i$ is greater than unity, cross-field electron heat conduction is dominant and that particle diffusion is limited by the ions.

Using the approximation $D_{\perp e} = D_{\parallel e}/(\omega_{c_e}\tau_e)^2$, the cross-field electron diffusion coefficient is

$$D_{\perp e} = 1.42 \times 10^3 \frac{(\bar{n}_e + z_i^2 \bar{n}_i)}{\sqrt{T_e}\,(1 - \beta)B_o^2\,(100 \text{ kG})} \text{ cm}^2/\text{sec} \qquad (3.8)$$

and an equivalent diffusion length is $\ell_{\perp e} = \sqrt{D_{\perp e} t}$. In HOFNEX, a cross-field thermal conductivity is defined as $k_{th_\perp} = 3/2\, n_e k D_{\perp e}$,

$$k_{th_\perp} = 0.34\, \bar{n}_e^2\, (1 + z^*)/(1 - \beta)B_o^2\, \sqrt{T_e} \text{ MW/cm-keV} \qquad (3.9)$$

The heat flux from a cylinder of radius r is then defined as

$$\ell_{\perp e} < r: \quad 2\pi r q_\perp = 2\pi r\, k_{th_\perp} T_e/\ell_{\perp e} = 57 \frac{\bar{n}_e^{3/2}\, \sqrt{1 + z^*}\, T_e^{3/4}\, r(\text{cm})}{\sqrt{1 - \beta}\, B_o\, \sqrt{t(\mu\text{sec})}} \text{ MW/cm} \qquad (3.10)$$

$$\ell_{\perp e} \geq r: \quad 2\pi r q_\perp = 2\pi r\, k_{th_\perp} T_e/r = 2.1 \frac{\bar{n}_e^2\, (1 + z^*) T_e^{1/2}}{(1 - \beta)B_o^2} \text{ MW/cm}$$

Using the previous typical experimental parameters, $\ell_{\perp e} = 1.8\, \sqrt{t(\mu\text{sec})}/\sqrt{1 - \beta}$ mm, and is always less than r in timescales of interest. Thus,

$$2\pi r q_\perp = \frac{4.1\, r(\text{mm})}{\sqrt{1 - \beta}} \frac{1}{\sqrt{t(\mu\text{sec})}} \text{ MW/cm}$$

For r = 2.5 mm, β = 0.75, and t = 10 nsec, this heat loss becomes 0.2 GW/cm and is significant when compared with typical GW/cm absorption rates. For later times when the diffusion distance increases, the radial heat loss is less important. Thus, the radial heat loss acts as a contribution to the threshold energy, as shown in Equation (2.13).

The above treatment is a conservative attempt to impose a two-dimensional effect on a one-dimensional code. It is conservative in that the outer boundary of the plasma column is assumed to be held at a low temperature by radiative cooling, and approximate internal temperature profiles are derived based on this boundary condition. Actually, the high external field could result from less rapid heat transfer to the cool plasma. HOFNEX, however, uses Equations (3.10) to compute radial heat transfer.

2. HIRAD

The details of HIRAD were given in Reference 1, but it has since been extensively modified to include much more detailed atomic physics. Its basic function to calculate rates of ionization, recombination, and radiation is unchanged, and it still uses a simplified time-dependent Coronal code. However, tabulated f numbers and Gaunt factors are now used and modifications are available to account for multi-step (collisional-radiative model) effects. These effects, however, must be calculated separately and then used to modify the Coronal rates as functions of n_e and T_e. The major features of HIRAD are listed below:

a) Coronal model - all ions in ground state, rates may be modified to account for collisional-radiative effects;
b) single step collisional ionization by hot electrons, inner and outer shell ionization accounted for by separate excitation energies;
c) radiative recombination only;

d) collisional excitation of outer shell (principal quantum number) electrons only, followed by instantaneous radiation to ground state;

e) two excitation levels per ion, one for $\Delta n = 1$ and one for $\Delta n = 0$, except for complete shell configurations; and

f) radiatively thin plasma, except for black body limitation on each line based on Doppler width.

The basic energy levels are either calculated in HIRAD or specified using NBS tables.[3] Absorption f numbers are specified using the NBS tables, and a listing of the energy levels and f numbers used in calculations for neon is shown in Table 3.1. The basic excitation rate is given by McWhirter[4] as

$$\chi_{pq} = 0.5 \langle g \rangle \bar{n}_e \frac{1}{\sqrt{T_e}\, \chi_{pq}} f_{pq}\, e^{-\chi_{pq}/T_e} \quad \text{nsec}^{-1} \qquad (3.11)$$

with $\langle g \rangle$ being the Gaunt factor. The ionization rate from the ground level is given by[4]

$$S_o(i) = 0.05\, \bar{n}_e \frac{\zeta_i}{\chi_i^{3/2}} \sqrt{\frac{T_e}{\chi_i}} \left(\frac{4}{1 + 3T_e/\chi_i} \right) e^{-\chi_i/T_e} \quad \text{nsec}^{-1} \qquad (3.12)$$

where ζ_i is the number of equivalent outer shell electrons and χ_i is the ionization energy in keV. The radiative recombination rate is taken as[5]

$$\alpha(i) = 8.2 \times 10^{-6}\, \bar{n}_e\, z_i^2/\sqrt{T_e} \quad \text{nsec}^{-1} \qquad (3.13)$$

To account for the possibility of inner shell ionization, the following scheme is used. Equation (3.12) is used to compute an additional inner shell contribution with a value ζ_i' equal to the number of subshell electrons, and χ_i' equal to either the ionization energy of these electrons with

Table 3.1
Neon Energy Levels and f Numbers

NEON	CONFIGURATION	χ_i(eV)	LEVEL 1 CONFIGURATION	χ_1(eV)	f_{10}	LEVEL 2 CONFIGURATION	χ_2(eV)	f_{20}
1	$1s^2\ 2s^3\ 2p^6$	21.6	--	--	--	$2p^5\ 3s$	16.8	0.17
2	$1s^2\ 2s^2\ 2p^5$	41.1	$2s\ 2p^6$	26.8	0.33	$2p^4\ 3s$	31.0	1.74
3	$1s^2\ 2s^2\ 2p^4$	63.5	$2s\ 2p^5$	25.3	0.26	$2p^3\ 3s$ $2p^3\ 3d$	43.0 50.0	0.14 0.21
4	$1s^2\ 2s^2\ 2p^3$	97.0	$2s\ 2p^4$	22.8	0.34	$2p^2\ 3s$	59.3	0.10
5	$1s^2\ 2s^2\ 2p^2$	126.3	$2s\ 2p^3$	24.0 35.0	0.26 0.14	$2p\ 3d$	86.0	0.81
6	$1s^2\ 2s^2\ 2p$	157.9	$2s\ 2p^2$	22.1 29.0	0.14 0.28	$2s^2\ 3d$	101.2	0.54
7	$1s^2\ 2s^2$	207.2	$2s\ 2p$	26.6	0.57	$2s\ 3p$	126.0	0.05
8	$1s^2\ 2s$	239.0	$1s^2\ 2p$	16.0	0.15	$1s^2\ 3p$	140.3	0.30
9	$1s^2$	1195.0	--	--	--	$1s\ 2p$ $1s\ 3p$	918.0 1070.0	0.72 0.15
10	1s	1362.0	--	--	--	2p	1017.0	0.42

the outer electrons removed, or the lowest level excitation energy of those electrons if it is high enough for an Auger process to occur.

This Coronal model will only apply when the radiative decay rate of all excited states is faster than all other rates. The radiated power per line would then be

$$P_{oq} = k\chi_{oq} X_{oq} n(i) \qquad (3.14)$$

The radiation decay rate from state q to state p is given in terms of the absorption f number as

$$A_{qp} = 6.67 \times 10^{15} \frac{g_p}{g_q} \frac{f_{pq}}{\chi^2_{pq}(\text{Å})} = 4.34 \times 10^{13} \frac{g_p}{g_q} f_{pq} \chi^2_{pq}(\text{keV}) \ \text{sec}^{-1} \qquad (3.15)$$

where g_i is the level degeneracy. The de-excitation rate of level q by electron impact is just $(g_p/g_q)\exp(\chi_{pq}/T_e)$ times the excitation rate, or

$$X^{\star}_{qp} = 0.5 \langle g \rangle \bar{n}_e \frac{1}{\sqrt{T_e}\, \chi_{pq}} \frac{g_p}{g_q} f_{pq} \ \text{nsec}^{-1} \qquad (3.16)$$

For typical conditions with $T_e \simeq \chi_{pq}$ and $\bar{n}_e = 1$, the radiative decay rate will exceed the collisional decay rate for $\chi_{pq} > 0.025$ keV. Table 3.2 lists some typical atomic quantities for Li-like neon. The excitation and de-excitation rates connecting these levels are shown in Figure 3.1, along with the ionization rates. The ionization rate from an excited level p is given by[6]

$$S^{\star}_p(i) = 0.085 \bar{n}_e \left\{ \frac{1 + 2\, T_e/\chi^{\star}_{i,p}}{3} \right\} \frac{1}{\chi^{\star}_{i,p} \sqrt{T_e}} e^{-\chi^{\star}_{i,p}/T_e} \ \text{nsec}^{-1} \qquad (3.17)$$

with the minimum value of the term in brackets being unity, and $\chi^{\star}_{i,p}$ being the ionization energy of level p of ion i.

Table 3.2

Atomic Data for Neon (VIII)

LEVEL	CONFIGURATION	ε_i (eV)	g_i	ABSORPTION f NUMBERS	RADIATION DECAY RATES (sec^{-1})
0	$1s^2$ 2s	0	2	$f_{01} = 0.152$ $f_{02} = 0.298$	--
1	$1s^2$ 2p	16	6	$f_{13} = 0.667$	$A_{10} = 5.64 \times 10^8$
2	$1s^2$ 3p	140	6	$f_{23} = 0.038$	$A_{20} = 8.53 \times 10^{10}$
3	$1s^2$ 3d	142	10	--	$A_{31} = 2.76 \times 10^{11}$ $A_{32} = 2.14 \times 10^6$

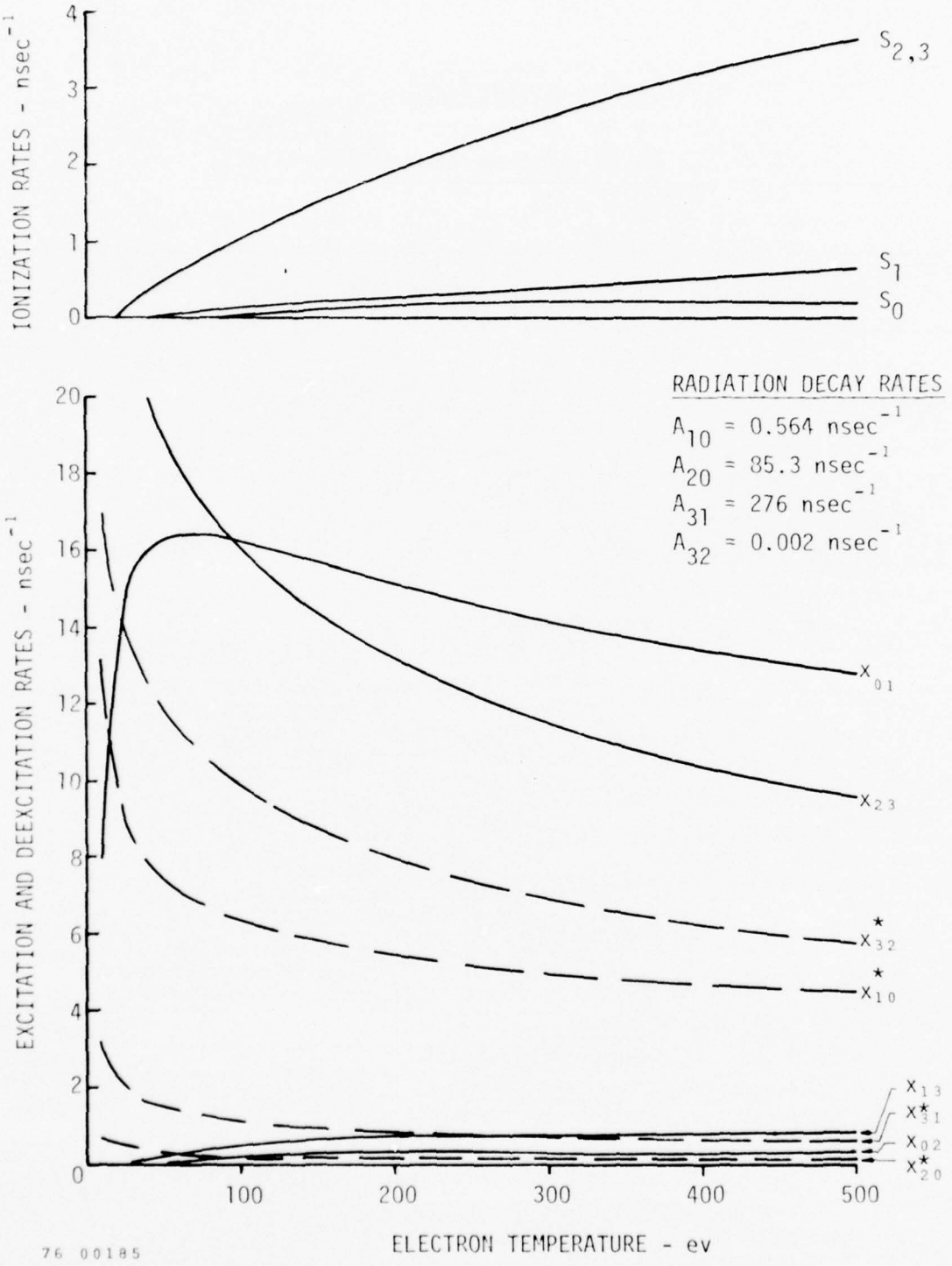


Figure 3.1. Rates of Excitation, Deexcitation, and Ionization for Li-Like Neon

$n_e = 10^{18}/cm^3$ for x_{01}: $\langle g \rangle = 4\langle g_{std} \rangle$

The Gaunt factor $\langle g \rangle$ is taken as a constant value times $\langle g_{std} \rangle$, where $\langle g_{std} \rangle$ is given by Allen[7] and can be approximated as

$$\langle g_{std} \rangle = 0.2 + 0.8\, e^{-4(\chi_{pq}/T_e)^{.7}} \qquad (3.18)$$

The ratio $R_g = \langle g \rangle / \langle g_{std} \rangle$ has been computed by Davis[8] and is reproduced in Figure 3.2 for certain transitions in oxygen and nitrogen ions. The transitions labeled (1) are the resonance 2s - 2p transitions, and those labeled (2) are 2s - 3p transitions. The approximation $\langle g \rangle = R_g \langle g_{std} \rangle$ is seen to be valid. In HIRAD, R_g is chosen as unity for all non-resonance transitions, and the values of R_g used for resonance transitions are listed in Table 3.3. The rates χ_{01} and χ^*_{10} in Figure 3.1 thus have $R_g = 4$.

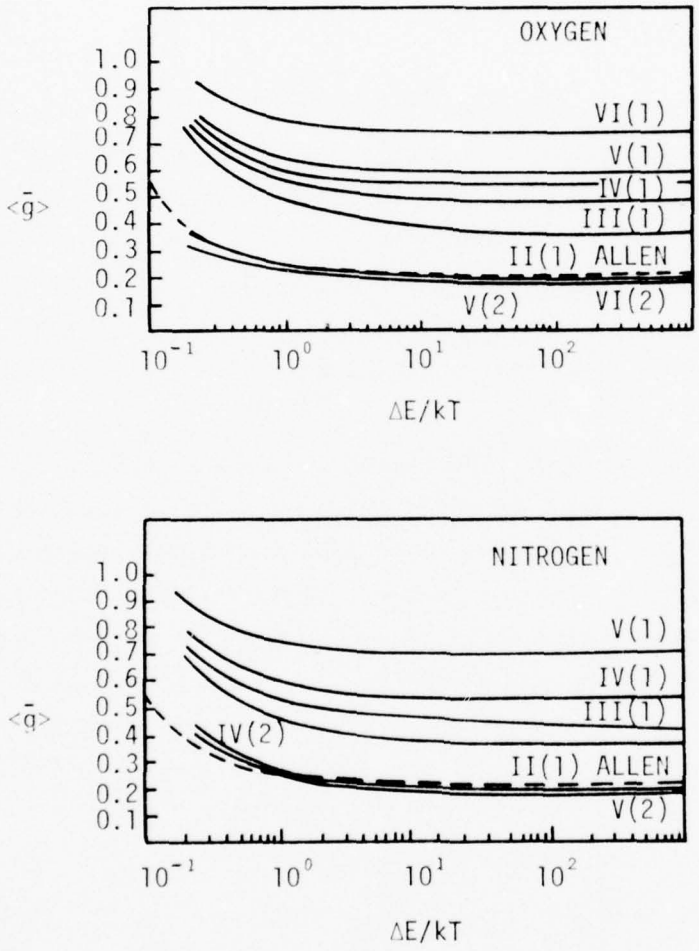
In order to judge the applicability of the Coronal model, the excited level populations n_1, n_2... must be estimated. For Li-like ions (and even Be-like and B-like ions, as seen from Table 3.1) with low-lying 2p states, the radiative decay rate A_{10} for the 2p level is much slower than the excitation rate χ_{01} and de-excitation rate χ^*_{10}. For the higher-lying levels, this situation is reversed and a modified Coronal model may be used. Ignoring ionization out of and recombination into level 1, and using the fact that $A_{31} \gg \chi_{13}$, the ratio of n_1/n_0 is given by

$$\frac{n_1}{n_0} = \frac{\chi_{01}}{\chi^*_{10} + A_{10}} \simeq \frac{(g_1/g_0)}{1 + A_{10}/\chi^*_{10}} \quad \text{for } T_e \gg \chi_{10} \qquad (3.19)$$

For Li-like neon, $n_1/n_0 \simeq 1/3$ over the temperature range of interest, and the combined levels n_0 and n_1 can be considered a separate ground state with a Coronal radiation rate given by

$$P_{0,1\text{-}2,3} = (0.25\, k\chi_{02}\chi_{02} + 0.75\, k\chi_{13}\chi_{13})n_0 \qquad (3.20)$$

Effective Gaunt Factors for Electron Impact Excitation



76 00186

Figure 3.2. Average Gaunt Factors for Oxygen and Nitrogen Excitations

Table 3.3

Gaunt Factor Multiplication Factors - R_g

ION	TRANSITION	R_g
$1s$	$1s - 2p$	1.0
$1s^2$	$1s^2 - 1s\ 2p$	1.25
$1s^2\ 2s$	$2s - 2p$	4.0
$1s^2\ 2s^2$	$2s^2 - 2s\ 2p$	3.0
$1s^2\ 2s^2\ 2p$	$2s^2\ 2p - 2s\ 2p^2$	2.75
$1s^2\ 2s^2\ 2p^2$	$2s^2\ 2p^2 - 2s\ 2p^3$	2.5
$1s^2\ 2s^2\ 2p^3$	$2s^2\ 2p^3 - 2s\ 2p^4$	2.0
$1s^2\ 2s^2\ 2p^4$	$2s^2\ 2p^4 - 2s\ 2p^5$	1.0
$1s^2\ 2s^2\ 2p^5$	$2s^2\ 2p^5 - 2s\ 2p^6$	1.0

In HIRAD, the f number and Gaunt factor used for X_{02} are just adjusted accordingly. Likewise, the ionization rate is also modified as $S_{0,1} = 0.25\ S_0 + 0.75\ S_1^*$. Generally, in HIRAD, just the simple rate S_0 was used. A multi-step ionization rate increase would be given by $(n_2/n_0)S_2^* \simeq (X_{02}/A_{20})S_2^*$. The ratio X_{02}/A_{20} or X_{13}/A_{31} never exceeds 3×10^{-3}, and $S_{2,3}^*$ does not exceed S_0 by more than 20 for temperatures above 100 eV, so that multi-step ionization is generally not important except at low temperatures. Multi-step ionization was not accounted for in the HIRAD calculations used in this report.

The only important remaining non-Coronal effect is the rate of resonance radiation for Li-like and less highly stripped ions. The Coronal rate would be given by Equation (3.14), but the actual rate will be $kX_{01}A_{10}n_1(i) \simeq 0.75\ kX_{01}[A_{10}/(1 + A_{10}/X_{10}^*)]\ n(i)$. For Li-like neon, this is lower than the Coronal rate by approximately the ratio $0.75\ A_{10}/X_{01} \simeq 1/40$ in the range of interest.

The one remaining modification to the Coronal model concerns the optical depth of the plasma. The absorption cross-section given by Griem[9] is

$$\int \sigma_{pq}^a\ d\omega = ?\ \pi^2\ r_o c f_{pq} = 0.166\ f_{pq}\ cm^2/sec \qquad (3.21)$$

where r_o is the classical electron radius $r_o = e^2/4\pi\varepsilon_o mc^2 = 0.282 \times 10^{-12}$ cm. For a Doppler broadened line,

$$\frac{\Delta\omega}{\omega} = 2.43 \times 10^{-3}\sqrt{T_i/A_i} \quad \text{Doppler Broadening} \qquad (3.22)$$

and using the relationship $\nu_{pq}(sec^{-1}) = 3 \times 10^{18}/\lambda(\mathring{A}) = 2.4 \times 10^{17}\ \chi_{pq}(keV)$,

$$\sigma_{pq}^a = \frac{\int \sigma_{pq}^a\ d\omega}{\Delta\omega} = 4.5 \times 10^{-17}\ f_{pq}/\sqrt{T_i/A_i}\ \chi_{pq}\ cm^2 \qquad (3.23)$$

Typically, for T_i = 0.2 keV, A_i = 20, $n_i = 10^{17}$/cm, the absorption coefficient $k_a = \sigma^a_{pq}\, n_i$ is equal to 45 f_{pq}/χ_{pq} cm^{-1}.

The effect of strong line absorption will depend on the ratio of $A_{pq}/(\chi^*_{pq} + S^*_p)$. If this quantity is larger than $k_a r_p$, where r_p is a typical plasma dimension, the absorbed radiation will be simply re-emitted with no change in plasma energy balance. This is always the case in the laser heated solenoid plasma ($r_p \simeq 2$ mm) for $\chi_{pq} > 0.1$ keV. Energy levels below 0.1 keV will tend toward LTE due to the strong self-absorption. The 2s - 2p resonance levels will already be in LTE since A_{10}/χ^*_{10} in Equation (3.19) is small (if it was not, then strong self-absorption would negate this factor). This radiation would then be limited (as of course would all radiation) to the black body value

$$B_\nu(T) = \frac{2h\nu^3}{c^2}/(e^{h\nu/kT} - 1) = 5.06 \times 10^6\, T_e^3 \left\{ \frac{(\chi/T_e)^3}{e^{\chi/T_e} - 1} \right\} \text{ GW/cm}^2\text{-keV} \quad (3.24)$$

The radiated flux is then limited to $B_\nu \Delta\nu 2\pi r_p$, with $\Delta\nu$ given by Equation (3.22), or

$$P_{\text{rad-max/line}} = 1.23 \times 10^4\, T_e^4 \left\{ \frac{(\chi/T_e)^4}{e^{\chi/T_e} - 1} \right\} \sqrt{T_i/A_i}\; 2\pi r_p \text{ GW/cm} \quad (3.25)$$

This value is used in HIRAD with a multiplication factor BBMFCT to account for the number of distinct lines in a given n,ℓ state.

The excitation limited radiation rate given by Equations (3.11) and (3.14), the LTE radiation rate given by Equation (3.15) and the equation

$$P = k\chi_{pq} A_{qp} \left\{ 1 + \frac{g_q}{g_p}\, e^{\chi_{pq}/T_e} \right\}^{-1} n(i), \quad (3.26)$$

and the black body limited rate given by Equation (3.25) are plotted on Figure 3.3 for typical experimental conditions. For $\chi_{pq} < 0.025$ keV, the LTE radiation rate is lower than the excitation rate, which means that Coronal conditions do not apply (similar to $A_{qp} < X^{\star}_{qp}$). However, line radiation below 0.025 keV will be strongly black body limited even for values of BBMFCT as high as 100, except for the final heating stages when only small fractions of Li-like ions are present. HIRAD will be in error there in computing low energy resonance radiation, but the arbitrary choice of BBMFCT will still be a dominant factor in determining the low energy resonance radiation contribution to the system energy balance. At the final quasi-steady conditions, the Li-like ion fraction may be influenced by a more exact model of recombination, including dielectronic recombination, that is beyond the scope of this model. Dielectronic radiation will be important only for temperatures greater than 20 percent of the first excited state energy.

For electron temperatures above 0.1 keV, radiation above 0.1 to 0.15 keV will not be black body limited even for values of n_i as high as $10^{17}/cm^3$ and BBMFCT as low as 1 or 2, and all $\Delta n = 1$ line radiation will be accurately determined by the Coronal model. The modification of Equation (3.20) should be used to determine an effective f number and Gaunt factor.

One additional factor is important in determining the radiative flux over the region where the Coronal model is applicable, and that is the effect of forbidden transitions whose excitation rates can not be approximated by the simple formula given by Equation (3.11). Davis, Kepple, and Blaha[10] have made distorted wave calculations for both allowed, forbidden, and spin exchange transitions in various ionization states of carbon, nitrogen, and oxygen. Figure 3.4 is a reproduction of their calculations for He-like oxygen. For the allowed singlet S - singlet P excitation, use of Equation (3.11) with $f_{01} = 0.69$ yields a ratio of $R_g = \langle g \rangle / \langle g_{std} \rangle \simeq 1.25$.

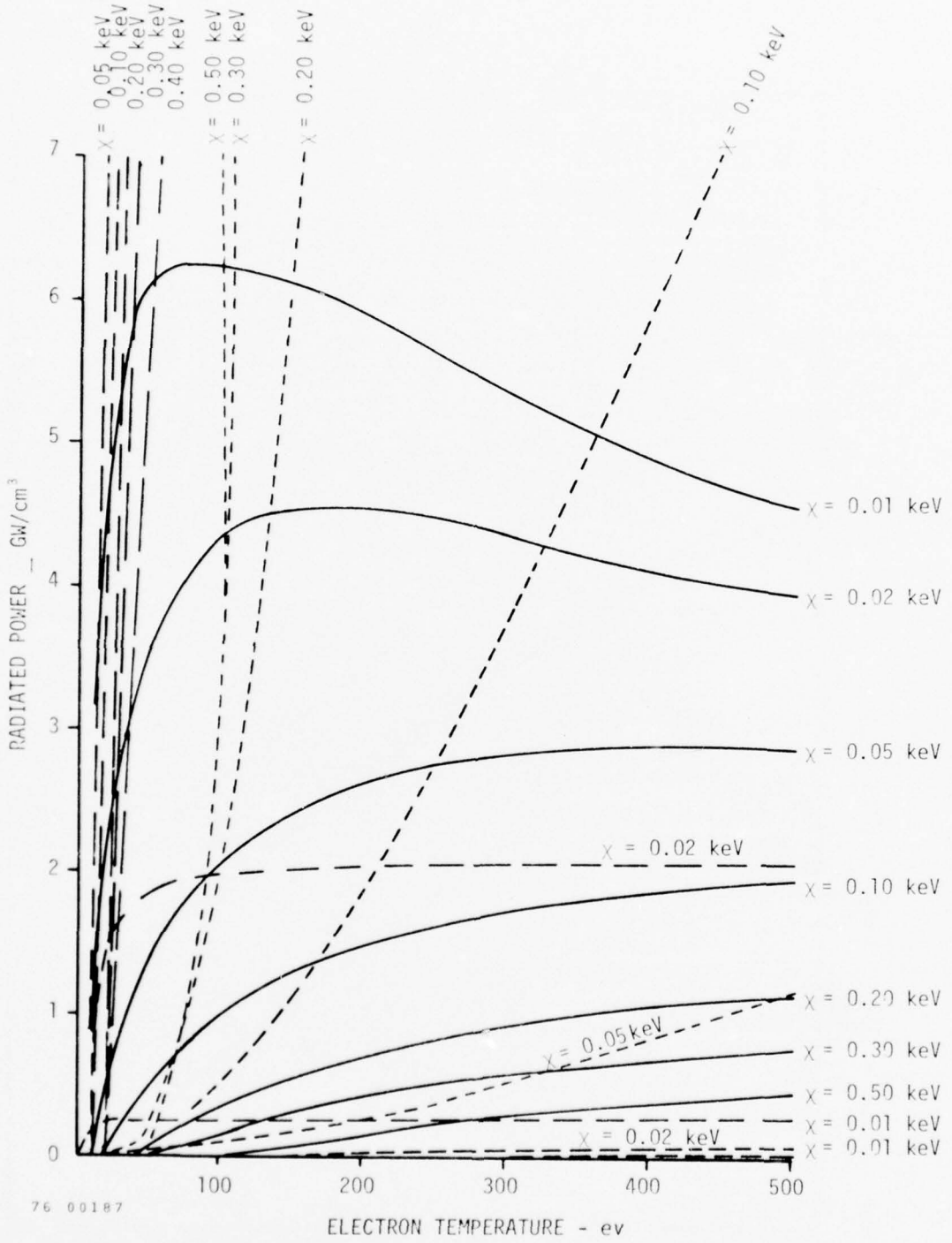


Figure 3.3. Radiation Limits Based on Excitation Rates, Radiation Rates, and Black Body Rate

$n_e = 10^{18}/cm^3$ $n_i = 10^{17}/cm^3$ ——— Excitation Limited

$f_{pq} = 0.5$ $R_g = 1$ $g_p/g_q = 3$ — — — Radiation Rate Limited

$T_e = T_i$ $A = 20$ $r = 0.2$ cm - - - Black Body Limited

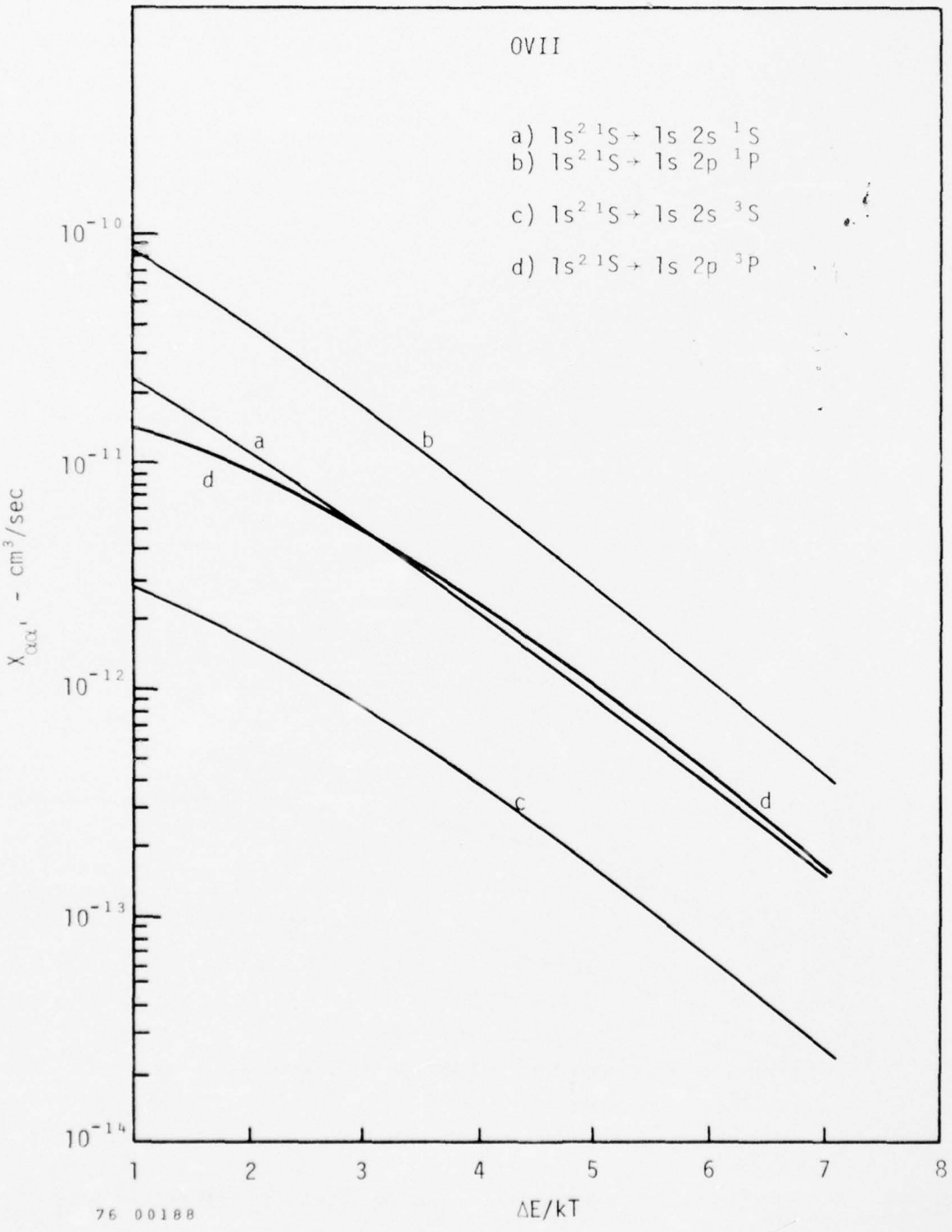


Figure 3.4. Electron Impact Excitation Rate Coefficients for OVII

Although this ratio is not entirely constant with $\Delta E/kT$, it is used in the calculations as displayed by Table 3.3. Of even greater importance is the magnitude of the forbidden singlet S - singlet S excitation, and the spin exchange singlet S - triplet P excitation. Each of these rates is about one-third of the allowed excitation rate. The triplet P - triplet S multiplet will be strongly coupled (its radiation will be observable in the vacuum UV for the He-like ions of higher z than carbon and, for high z ions, the triplet S state will radiate to the ground, giving a strong intercombination line. Thus, the effective f number used in HIRAD for $\Delta n = 1$ He-like excitation should be about (1 + 2/3) times the f number for the allowed transition alone.

3. Neon Calculations

A series of calculations using HOFNEX and HIRAD were run to attempt to explain the experimental results. The f-numbers used for the $\Delta n = 0$ and $\Delta n = 1$ transitions are shown in Table 3.4, along with the Gaunt factor multiplication factor R_g for the lowest energy transition. The multistep ionization factor, R_s, was used according to the formula

$$S_{total} = IRF \{1 + MSF(R_s - 1)\}S_o \qquad (3.27)$$

where S_o is given by Equation (3.12) and IRF (ionization rate factor) and MSF (multistep factor) are arbitrary program inputs. MSF was always set to zero (except for one example) based on the previous discussions for Li-like ions where any ionization rate bottleneck would occur and modifications to the standard (Equation 3.12) Coronal ionization rate would be critical.

The f-numbers listed are in all cases somewhat higher than the tabulated values (Table 3.1) to account for transitions to higher energy levels and for forbidden transitions. For exam , the tabulated He-like f-numbers for the 1s-2p and 1s-3p transitions are .723 and .149 with

Table 3.4

Atomic Data Used in HIRAD for Neon

No. of Electrons Remaining	Configuration	f-number $\Delta n = 0$	f-number $\Delta n = 1$	Gaunt Factor Multiplication R_g	Multi-Step Ionization Rate Factor - R_s
1	$1s$	--	0.5	1.0	1
2	$1s^2$	--	1.0	1.25	1
3	$1s^2 2s$	0.2	0.3	4.0	4
4	$1s^2 2s^2$	0.6	0.6	3.0	3
5	$1s^2 2s^2 2p$	0.5	0.5	2.75	2
6	$1s^2 2s^2 2p^2$	0.5	0.8	2.5	2
7	$1s^2 2s^2 2p^3$	0.4	0.2	2.0	2
8	$1s^2 2s^2 2p^4$	0.3	0.4	1.0	1
9	$1s^2 2s^2 2p^5$	0.3	2.0	1.0	1
10	$1s^2 2s^2 2p^6$	--	3.0	1.0	1

transition energies of .918 and 1.070 keV respectively. HIRAD allows just one $\Delta n = 1$ transition, and this was chosen as the 1s-2p transition with an effective f-number of 1.0 in calculating radiative losses.

Figure 3.5 displays a calculation for a plasma sample using HIRAD alone with correct absorption and plasma expansion, but no radial or end losses. A line density of $.025 \times 10^{18}$ ions/cm was chosen as representative of the final heated plasma conditions with $n_T = 10^{18}/cm^3$, $z = 8$, and $r_p = 2.7$ mm. A 1 GW power level is also typical of experimental conditions. The self absorption factor (SAF) is an arbitrary program input whose inverse BBMFCT = SAF^{-1} multiplies Equation (3.25) to set a black body limit per line. A value of SAF = 0.01 is very conservative in estimating radiation losses since it assumes that the low energy 2p-2s resonance radiation is spread over 100 distinct lines.

With the above choice of SAF the non-resonance $\Delta n = 1$ L-shell radiation is never black body limited, and is always set by the collisional excitation rate. The peaks and valleys in the radiation rate are typical of ionization processes where succeeding ions radiate strongly at a given temperature and then are replaced by the next ion state, with a higher excitation energy and lower collisional excitation until the temperature increases further. These peaks could constitute radiation barriers to further ionization if they exceeded the absorbed power curve for any significant time. In this calculation, and in the present experiments they just constitute a large energy sink which must be overcome.

Even with the low self absorption factor, the resonance radiation is strongly black body limited for most ions with fractions above five percent. It increases very rapidly initially with increasing temperature, levels off, and then decreases to a lower value corresponding to the disappearance of Ne_{VII} and the remaining of only one ion (Ne_{VIII}) with a 2s-2p resonance line. This Ne_{VIII} resonance radiation is black body limited to 100 MW/cm until the Ne_{VIII} fraction drops below five percent and the excitation rate becomes the limiting factor.

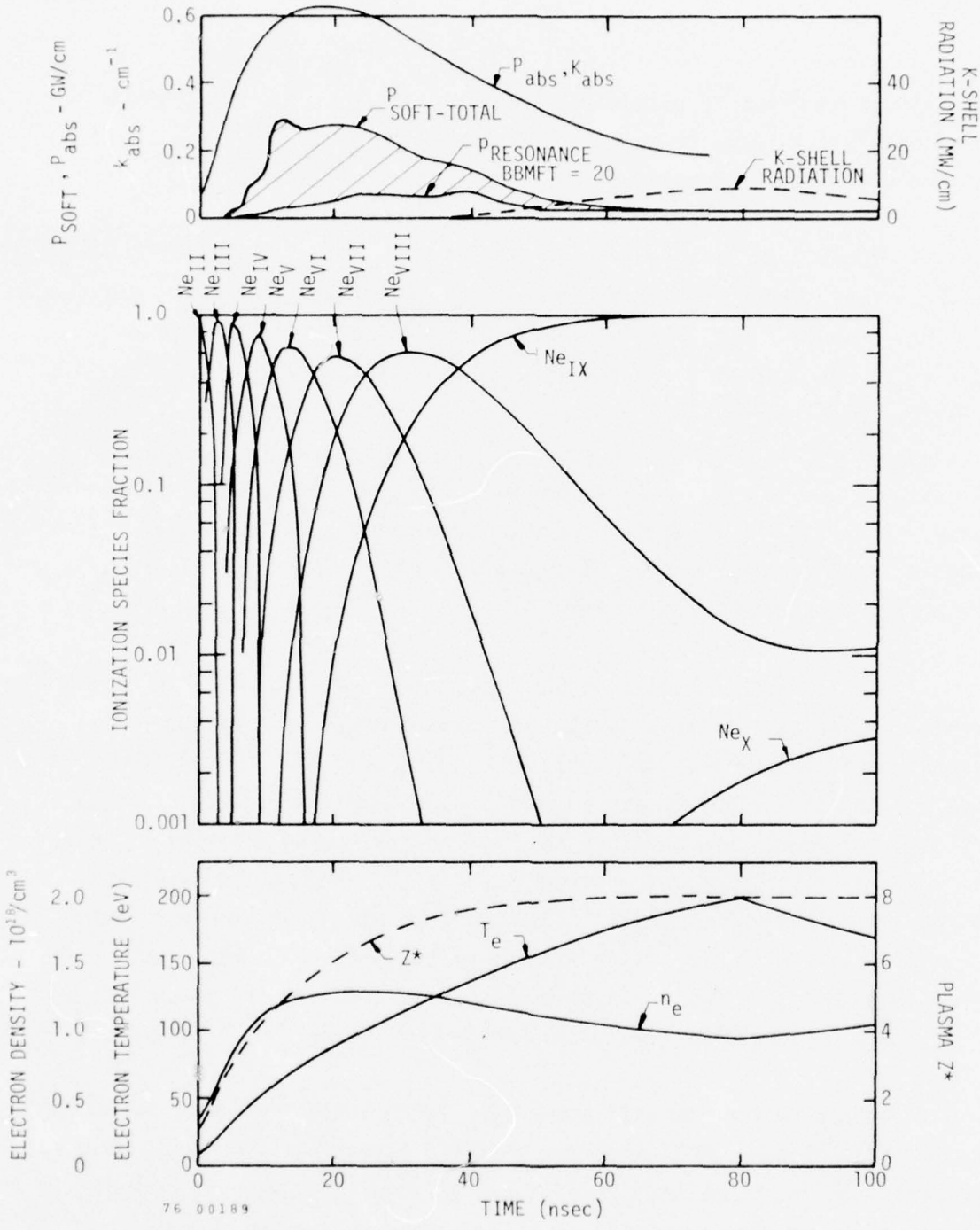


Figure 3.5. Time History of Neon Plasma Irradiated by 1 GW CO_2 Laser

Steady 100 kG Magnetic Field
$N_p = 0.025 \times 10^{18}$ cm^{-1}
No End-Losses
Standard Radial Heat Transfer

A rough approximation often used for determining when steady Coronal equilibrium conditions are achieved is that $n_e \tau = 10^{12}$ sec/cm^3. When this density-time product is reached, collisional ionization is balanced by radiative recombination and ionization states are produced with ionization energies between 2 and 10 times the value of the electron temperature (higher values occurring at lower temperatures). However, quasi-steady conditions may be produced for shorter density-time products when large differences exist in the ionization energies of adjacent ions. An important feature of Figure 3.5 is the time to reach a Ne_{IX} ion fraction of about 95 percent, at which time the $\Delta n = 1$ L-shell radiation essentially ceases and the resonance radiation decreases markedly. This time of 50 nsec corresponds to an $n_e\tau$ product of only 5×10^{10} and, although the plasma is not in true Coronal equilibrium (as evidenced by the nonsteady Ne_X population), it has reached steady ionization conditions for all practical purposes. This behavior is typical of ionization processes through many shells, and is a desirable feature of laser heated plasma radiation schemes since the He-like radiation is at a peak for density time products between $n_e\tau = 5 \times 10^{10}$ and 5×10^{11} sec-cm^{-3}. At later times (and slightly higher temperatures) the H-like, or even bare ion will predominate and the desirable kilovolt radiation will be lower.

The strong 10 MW/cm K-shell radiation shown in Figure 3.5 is not achieved experimentally on a 100 nsec timescale due to several additional loss mechanisms. Figure 3.6 shows several different HOFNEX calculations for a 5 cm long plasma column irradiated by a 80 J laser spike in 80 nsec. A Gaussian profile $P = P_o e^{-\{(t-40)/40\}^2}$, with t starting at 0 and given in nsec, is assumed. The top two curves (with the hatched area between them) are calculations for a neon plasma initially in the He-like state, and not recombining or ionizing. The solutions are simple bleaching waves which can be derived analytically,[11] except for end losses, and in the case of the lower of the two curves, radial heat transfer. Radial heat transfer lowers the ideal temperature by about 15 percent which, due to the exponential nature of the excitation rate, lowers the K-shell radiation by about 40 percent. If this radiation can be measured accurately, and if the Gaunt factor and f-number is well known, the $1s2p$-$1s^2$ resonance line radiation serves as a very sensitive measurement of electron temperature.

The remaining curves in Figure 3.6 were calculated with the neon initially singly ionized. The highest curve has no soft radiation ($\Delta n = 0$ or $\Delta n = 1$) whatsoever, and the difference between it and the curve above just reflects the energy going into ionization and the lesser absorption rate at the initially lower z. The ionization process alone, with no radiation, is seen to be a small factor in the total energy balance.

The remaining curves have varying degrees of soft radiation. They all have full $\Delta n=1$ L-shell radiation, and $\Delta n = 0$ resonance radiation limited by the value given in equation (3.25) multiplied by BBMFCT. Obviously the greater the amount of resonance radiation escaping from the plasma, the lower the final temperature achieved. The threshold laser energy needed to heat the plasma enough to produce K-shell radiation is a function of both the low energy radiation rates and the ionization rate, since the latter determines the time the plasma spends in a strongly radiating low z configuration. This effect is shown by the dashed temperature curve which includes the most rapid radiation rates, but also allows for multistep ionization in accordance with equation (3.27) and Table 3.4. At least in front of the column, the temperature is almost as high as for the calculation with no soft radiation. Since experimentally observed temperatures (as inferred from the K-shell radiation rates) are even lower than those shown for the calculations without multistep ionization and the lowest resonance radiation self absorption (highest value of BBMFCT) no further calculations were made using multistep ionization.

Two additional calculations are shown on Figure 3.6. The one labeled AREDFCT = 1.0 allows for free expansion of the plasma out the ends, with no self mirroring effects. Since self mirroring is observed experimentally, and free expansion does not reduce the plasma temperature for these short laser spikes, all subsequent calculations were made with AREDFCT = 0.5. The curves labeled $A_{min} = .15$ cm^2 probably come closest to a realistic explanation of the observed first spike behavior. The $N_p = .025 \times 10^{18}$ ions/cm value corresponds to a column area of about .25 cm^2

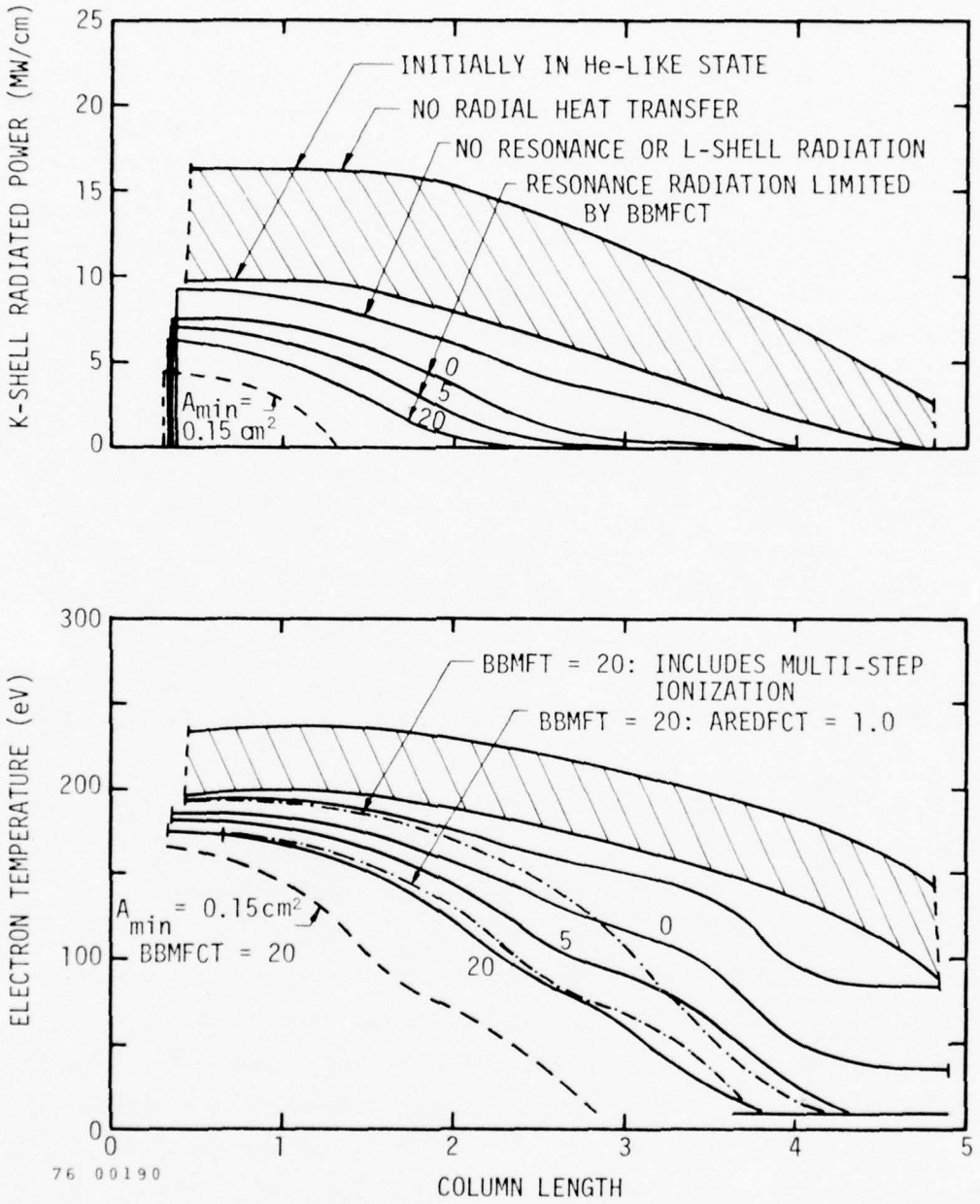


Figure 3.6. Calculated Temperatures and X-Ray Emission Profiles after Laser Heat Addition to Neon Plasma for Various Loss Mechanisms

B_{max} = 100 kG $\quad$ ε_{LASER} = 80 J

N_p = 0.025 x 10^{18}/cm $\quad$ 80 nsec Gaussian Pulse

A_{min} = 0 $\quad$ AREDFCT = 0.5

at the final heated conditions, but only an area of .08 cm^2 at the initial unheated condition where n_p = .3 x 10^{18} ions/cm^3. HOFNEX usually assumes that the laser beam size always matches the changing plasma column size, which should be true due to refraction once a density minimum is formed since the laser focal spot size is only 2 mm in diameter. However, during the initial heating process rapid ionization at the center of a Gaussian laser beam profile will lead to unfavorable density profiles and refractive losses. This is approximated by the A_{min} = .15 cm^2 calculation which specifies that the laser beam area can never be less than .15 cm^2, and the incident power used in HOFNEX is reduced by A_{column}/A_{min} for conditions where $A_{column} < A_{min}$. This stipulation has only been used on first spike calculations since it is unduly restrictive for subsequent heating when density peaks on center will not exist. Calculations such as shown on Figure 3.6 with A_{min} = .15 cm^2 are used in the experimental section (Figure 7.5) to compare first spike data with theory. They make a significant impact on first spike K-shell radiation levels and threshold energies.

A series of calculations are shown in Figure 3.7 for varying intensity laser spikes with the standard Coronal ionization rate and BBMFCT = 20. The integrated K-shell radiation rates are displayed on Figure 7.5 for comparison with experimental measurements. The exponential increase in radiation is due to both the exponential dependence of the excitation rate with electron temperature, and the increase in heated column length with increasing laser energy. A threshold behavior is exhibited with an energy (in this case about 40 J) below which no measurable K-shell radiation occurs. For the A_{min} = .15 calculations this threshold energy increases by another 20 joules due to the initial reduction in laser intensity. The threshold behavior is very evident experimentally, but it exhibits some variation due to small changes in focal patterns and initial plasma density profiles. A definite energy sink exists during the ionization process, which must be overcome before significant plasma heating can occur. The exact ionization rate and soft radiation rate (including self absorption effects) is critical in determining this energy since the plasma is radiating strongly in the UV during this time.

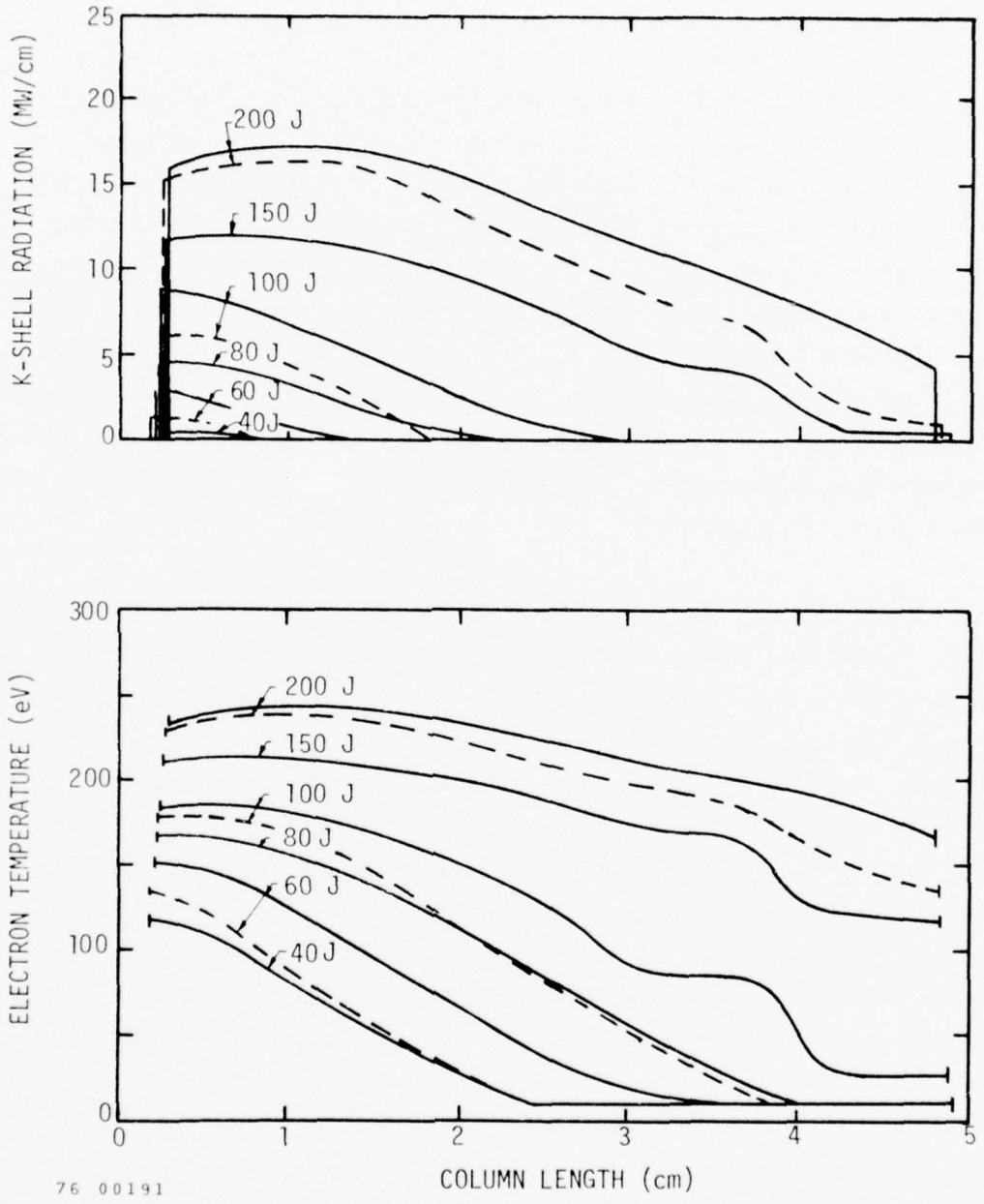


Figure 3.7. Calculated Temperature and X-Ray Emission Profiles for Neon Plasmas after 60 nsec Laser Irradiation

B_{max} = 100 kG — 80 nsec Triangular Pulse

N_p = 0.025 x 10^{18}/cm — AREDFCT = 0.5

——— A_{min} = 0 — BBMFCT = 20

– – – – A_{min} = 0.15 cm^2

Normal gain switched laser operation results in a strong first spike, with at least one afterspike due to the initial gain being driven below the cavity loss level. (This is sometimes accentuated by back reflection from induced parametric instabilities as will be discussed in Section VII). Figure 3.8 shows a calculation for the typical laser power history displayed in the upper corner of one of the graphs. Radiation and temperature profiles are shown every 100 nsec for comparison with later experiments on area wave propagation into the plasma column. The predicted inward movement of the radiating region will be seen to agree well with the experimental measurements, and thus the AREDFCT = 0.5 value has been adapted for all calculations.

The central set of curves shows laser absorption and soft radiation profiles at 280 nsec, which corresponds to the peak of the second afterspike intensity. The absorption rate exceeds the soft radiation rate throughout the heated region and the plasma temperature will increase. This is not the case for later times as evidenced by the decrease in temperature between 380 nsec and 480 nsec. Energy and radiation plots integrated over the total plasma column are shown in Figure 3.9 for the same laser irradiation as shown in Figure 3.8. The plotted values of T_e and z^* are those at the front of the plasma column. Laser powers of between .25 Gw and .40 Gw are needed to maintain plasma temperatures between 130 eV and 170 eV even when quasi-steady ionization levels are reached.

The bulk of the absorbed laser energy is seen to go into soft L-shell and resonance radiation. $\Delta n = 1$ L-shell radiation dominates initially due to self absorption of resonance radiation at low temperatures, but at higher temperatures the resonance radiation dominates. These effects can be seen from the radiation profile on Figure 3.8. At higher temperatures the plasma loss rate is about equally divided between radial heat conduction and resonance radiation. The former rate increases with temperature in accordance with equations (3.10), and actually sets a

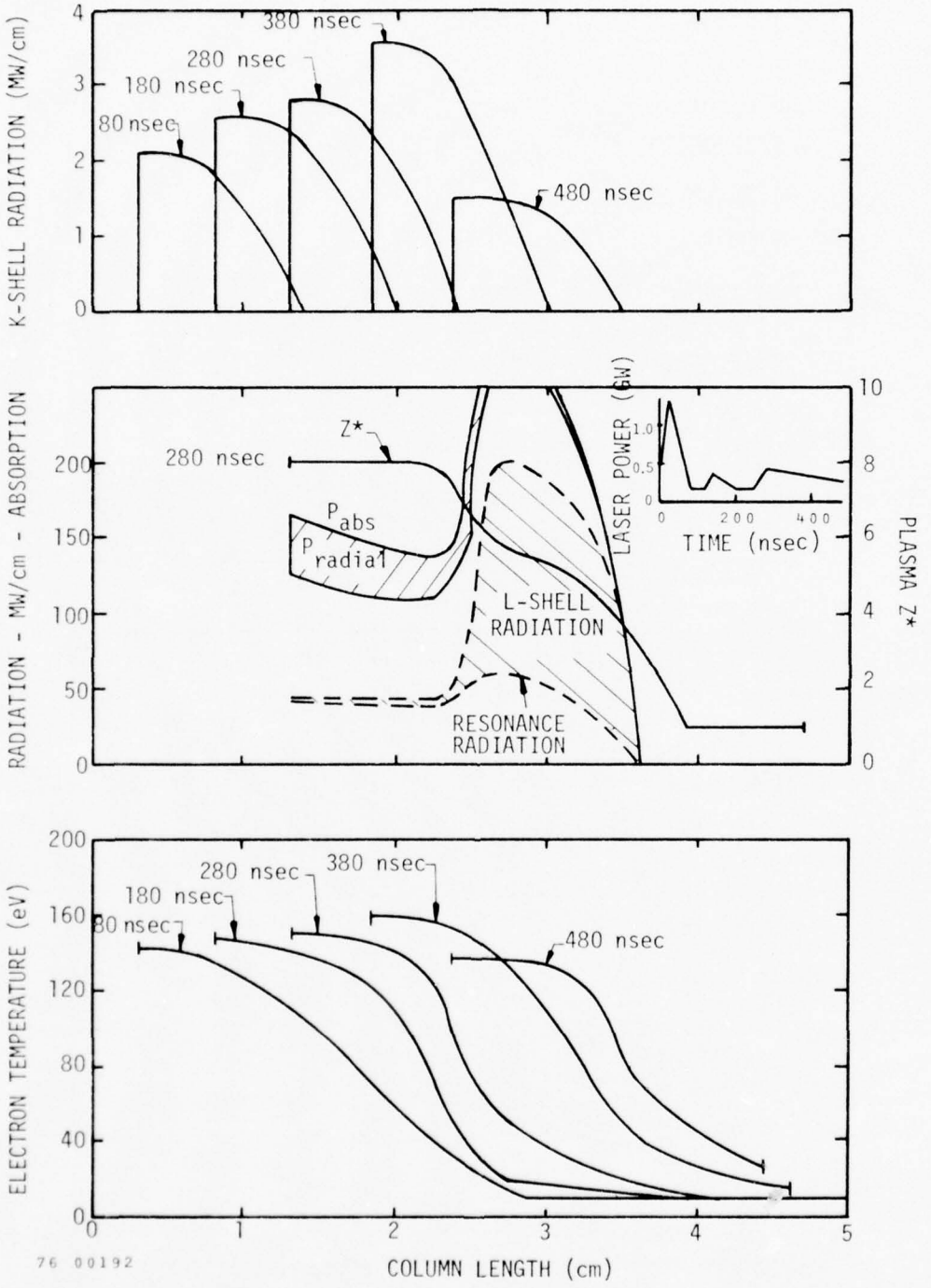


Figure 3.8. Calculated Neon Temperature and Radiation Profiles at Various Times

B_{max} = 100 kG $\quad$ ϵ_{LASER} = 170 J

$t_{1/4}$ = 800 nsec $\quad$ AREDFCT = 0.5

N_p = 0.025 x 10^{18} cm^{-1} $\quad$ BBMFCT = 20

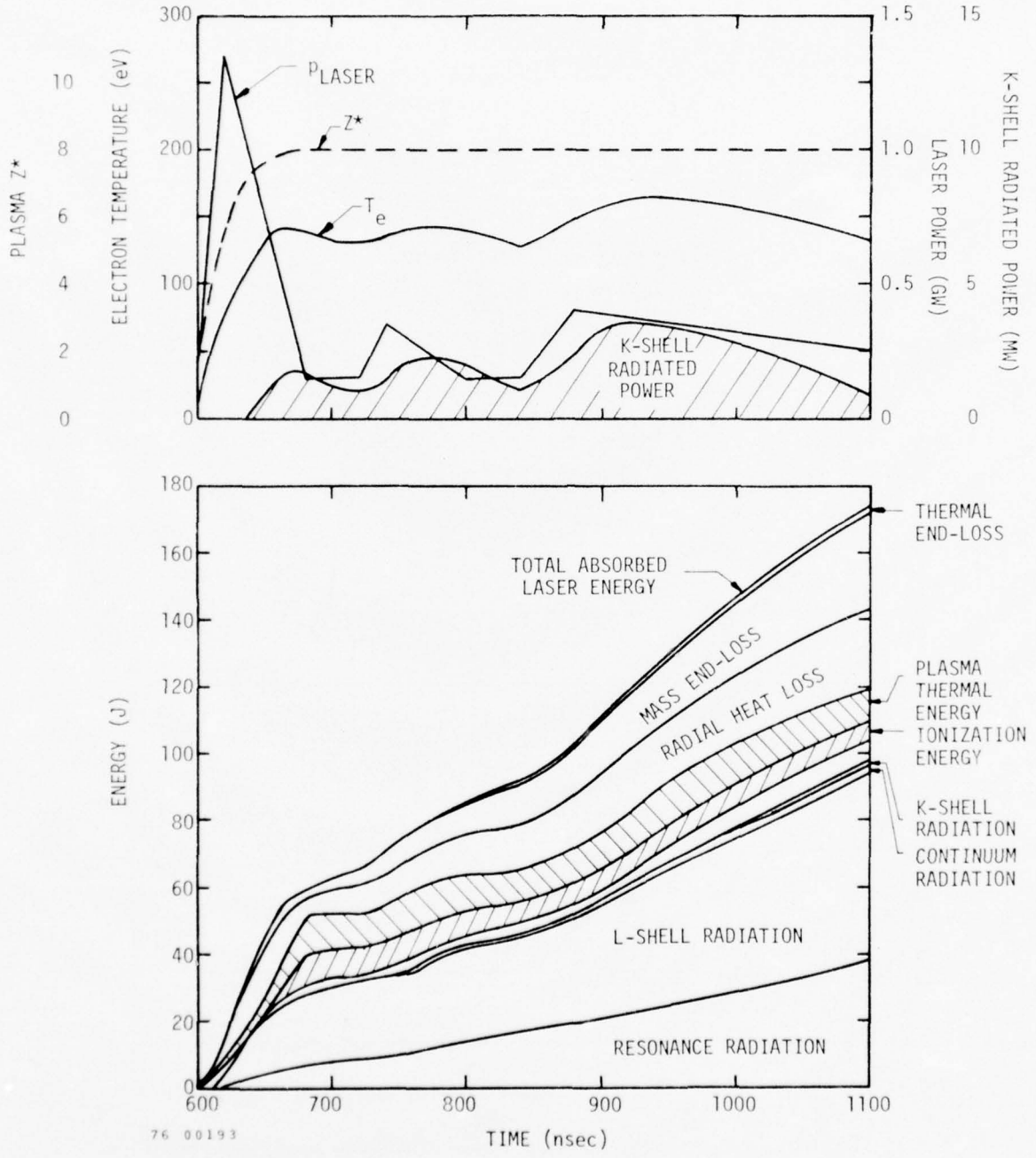


Figure 3.9. Numerical Simulation of Laser Heated Neon Experiment

B_{max} = 100 kG AREDFCT = 0.5

N_p = 0.025 x 10^{18}/cm BBMFCT = 20

steady temperature corresponding to a given laser power level. This effect is accentuated due to the inverse dependence of the laser radiation absorption coefficient on temperature.

The resonance radiation shown in Figure 3.8 at high temperatures is due to remaining fractions of Ne_{VIII}. The quasi-steady Ne_{VIII} population is given with respect to the Ne_{IX} population by the ratio of the recombination rate of Ne_{IX} to the ionization rate of Ne_{VIII}. Using Equations (3.12) and (3.13), this ratio is

$$\frac{X(Ne_{VIII})}{X(Ne_{IX})} = 6 \times 10^{-4} \frac{1 + 3T_e/0.24}{4T_e} e^{0.24/T_e} \qquad (3.28)$$

For T_e = 0.15 keV the ratio is 0.014 and for T_e = .24 keV, the ratio drops in half to 0.007. In Figure 3.5 it is seen to take approximately 80 nsec to reach the quasi-steady value given by Equation (3.28). The resonance radiation in this BBMFCT = 20 case is not black body limited, and is thus overestimated as seen from Figure 3.3. It dominates the $\Delta n = 1$ radiation by a factor of 13 (compare χ = 0.016 keV radiation rates to χ = 0.140 keV radiation rates in Figure 3.3 allowing for the f-numbers and Gaunt factors of Table 3.4) and thus the rapid cooling calculated in Figure 3.9 is something of a numerical artifact (especially since the radial heat loss rates are also conservatively high).

The rapid plasma cooling is especially noticed after all laser spikes for conditions where the laser power between spikes is low (see oscilloscope traces on Figures 7.4 and 7.5) and the copious soft radiation must thus be due to higher Ne_{VIII} fractions than calculated from Equation (3.28). It is only for this ion that the exact recombination rate becomes important, since the ionization rate completely dominates recombination for less highly stripped ions. Elton[6] gives estimates of three body and

dielectronic recombination which, in a simplified form, can be written

$$\text{Three Body Recombination:} \quad 12 \times 10^{-6} \overline{n_e}^{-2} \frac{\chi_i^2}{T_e} \ \text{nsec}^{-1} \tag{3.29}$$

$$\text{Dielectronic Recombination:} \quad 76 \times 10^{-6} \overline{n_e} \ \frac{z^2}{T_e^{3/2}} f_{oj} e^{-E_{oj}/T_e} \text{nsec}^{-1} \tag{3.30}$$

E_{oj} is the transition energy for a state j of the recombined ion, and f_{oj} is the f number to ground. For z = 8, χ_i = 1.2 keV, T_e = 0.15 keV, E_{oj} = 0.14 keV and f_{oj} = 0.3, the respective values of radiative, three body, and dielectronic recombination at $n_e = 10^{18}$ cm^{-3} are 1.4 x 10^{-3} nsec^{-1}, 0.77 x 10^{-3} nsec^{-1}, and 9.8 x 10^{-3} nsec^{-1}. Dielectronic recombination can thus be extremely important in setting quasi-steady plasma radiation losses, and can account for experimentally observed cooling rates.

4. He-like X-ray Conversion Efficiency

The X-ray conversion efficiency consists of two parts. A definite amount of energy must be invested in stripping the plasma down to the He-like state. This can be represented as

$$\eta_{\text{stripping}} = \left\{ 1 + \frac{\chi_T + \varepsilon_{\text{radT}}}{\frac{3}{2}(z+1)T_e} \right\}^{-1} \tag{3.31}$$

where χ_T is the total ionization energy per ion, ε_{radT} is the total radiated energy per ion during the stripping process, and z is the final ion charge. From Figure 3.9 it can be seen that ε_{radT} can be 10 times greater than χ_T if radiation trapping is not significant. $\frac{3}{2}(z+1)T_e$ can also exceed χ_T by a factor depending on the final temperature. For example, the total ionization energy involved in stripping down to Ne_{IX} is about 1 keV. This is close to $\frac{3}{2}(z+1)T_e$ for the examples calculated, but would be a factor of five lower if the plasma were heated to optimal temperatures to maximize hard radiation.

In the previous example the soft radiation was still significant even at the final heated conditions, but this will not be so at higher temperatures. An additional efficiency can then be defined as the percentage of the thermal energy content radiated in the allotted time interval. Using Equation (3.11) with $\langle g_{std} \rangle = 0.2$, and assuming pressure balance, the radiation timescale is

$$\tau_{rad} = \frac{1}{\chi_{pq}} \frac{\frac{3}{2}(1+z)T_e}{\chi_{pq}} = \frac{60(1+z)}{B^2(100\ kG)R_g f_{pq}} \chi_{pq}^{5/2} \left\{ \left(\frac{T_e}{\chi_{pq}}\right)^{5/2} e^{\chi_{pq}/T_e} \right\} \text{ sec} \tag{3.32}$$

The bracketed expression has a minimum of 1.23 at $T_e = 0.4\ \chi_{pq}$, and the above time becomes

$$\tau_{rad} = 75(1+z)\chi_{pq}^{5/2}/R_g f_{pq} B^2(100\ kG)\ \text{nsec} \tag{3.33}$$

For z = 9, χ_{pq} = 1 keV, R_g = 1, f_{pq} = 1 and B = 100 kG, the above time is 750 nsec. For a higher z = 24 ion, with χ_{pq} = 2 keV, R_g = 1, f_{pq} = 2.5 and B = 400 kG, the radiation timescale would be 265 nsec. The pulse efficiency can be defined as $\eta_{pulse} = \tau_{pulse}/\tau_{rad}$ where τ_{pulse} is the shorter of the desired maximum pulse time, or the end flow time, and the total X-ray conversion efficiency is approximately equal to $\eta_{stripping}\ \eta_{pulse}$. Of course, τ_{pulse} must be shorter than τ_{rad} for this analysis to be applicable.

For the experiments in neon, with $T_e \approx 0.15$ keV and $\chi_{pq} = 0.93$ keV, τ_{rad} is about 2.3 μsec. Pulsed radiation times during the laser tail are about 1/10 this long, yielding $\eta_{pulse} \approx 0.1$. Combining this with stripping efficiencies of 10 percent gives ideal total conversion efficiencies of 1 percent, or 1 J of X-rays for each 100 J of laser energy. This corresponds to 4 MW for a 250 nsec pulse width, and is in rough agreement with the detailed calculation shown in Figure 3.9.

5. Krypton Calculations

A few experiments were run with krypton in a fast solenoid and, surprisingly, a small amount of relatively hard (above 1.5 keV) radiation was measured. Numerical calculations were run at both low field and laser energy experimental conditions, and at high field and laser energy conditions corresponding to the previous calculations in Reference 1. The previous calculations assumed an f-number equal to the number of equivalent electrons, ignored many low energy resonance transitions, and used a constant specified Gaunt factor. Inner shell ionization was also treated in a manner to increase the effective ionization rate.

The present calculations use the atomic data listed in Table 3.5. HIRAD only can handle 20 stages of ionization, and the plasma was thus always assumed to be initially 8 times ionized. This is about twice the value produced by the fast solenoid, but the lower ionization stages should have only a minor influence on the total energy balance. The excitation energies for the lower stages of ionization are very approximate, being set from empirical scaling factors in HIRAD. The ionization energies are also set by empirical scaling factors, but should be reasonably accurate. The f-numbers and Gaunt factor multiplicative factor R_g for the 3s and 3p states were chosen identical to the respective 2s and 2p neon quantities for lack of a better method. The 3d data are not critical for the higher energy runs, and were chosen

Table 3.5

Atomic Data Used in HIRAD for Krypton

No. of Electrons Remaining	Configur-ations	f-Number $\Delta n=0$	Excitation Energy $\chi\Delta n=0$(eV)	f-Number $\Delta n=1$	Excitation Energy $\chi\Delta n=1$(eV)	Gaunt Factor Multiplicator Rg	Ionization Energy χi(eV)
9	$2s^2\ 2p^5$	0.3	235	5.0	1768	1.0	3065
10	$2s^2\ 2p^6$	--	--	4.8	1691	1.25	2927
11	3s	0.2	64	0.3	589	4.0	1197
12	$3s^5$	0.6	102	0.6	550	3.0	1147
13	$3s^2\ 3p$	0.5	109	0.5	515	2.75	1046
14	$3s^2\ 3p^2$	0.5	83	0.8	458	2.5	990
15	$3s^2\ 3p^3$	0.4	79	0.2	440	2.0	942
16	$3s^2\ 3p^4$	0.3	106	0.4	417	1.0	878
17	$3s^2\ 3p^5$	0.3	122	2.0	404		827
18	$3s^2\ 3p^6$	0.2	144	3.0	400		785
19	3d	0.5	58	0.5	288		638
20	$3d^2$		74	1.0	281		597
21	$3d^3$		81	1.5	264		549
22	$3d^4$		80	2.0	242		497
23	$3d^5$		86	2.5	228		454
24	$3d^6$		67	3.0	192		391
25	$3d^7$		67	3.5	173		347
26	$3d^8$		56	4.0	145		296
27	$3d^9$		52	4.5	127		255
28	$3d^{10}$	--	--	5.0	107		217

as indicated. The $\Delta n = 1$ f-numbers and R_g values for the $2p^5$ and $2p^6$ states are critical in that they determine the radiation rates once the desired neon-like configuration is reached. The f-number value for the $2p^6 - 2p^5 3s$ and $2p^6 - 2p^5 3d$ transitons can be obtained from Wiese[3] by plotting the f-numbers as a function of z for lower z elements and extrapolating. This method gives an f-number of 0.03 for the 3s transition and approximately 3 for the 3d transition. A value of $R_g = 2$ was somewhat arbitrarily assumed yielding an fR_g product of 6, equal to the number of equivalent electrons. An fR_g value of 5 was then chosen for the $\Delta n=1$ $2p^5$ excitation rate.

Figure 3.10 shows the results of a calculation for the same conditions used in Figure 3.9 of Reference 1. The L shell radiated power peaks at 1.8 GW instead of 6.0 GW due to a reduction in fR_g by a factor of 2, and an increase in the threshold energy due to longer ionization times for the 3s electrons. The actual x-ray conversion efficiency depends so critically on the detailed ionization and excitation rates, scaling in the same manner as described for He-like radiators, that the 10 percent conversion depicted can only be regarded as an order of magnitude estimate. It does seem reasonable, however, based on the results we have obtained in this program.

Higher densities are obviously desirable to decrease the ionization time, but this will not reduce the threshold energy unless self-absorption reduces the soft radiation rates. There was no significant self absorption in the Figure 3.10 calculation due to the high temperature and relatively low densities. The calculations shown are at about the highest densities practicable within the solenoid confinement framework. If longer pulse times are acceptable, higher efficiencies are possible by matching the laser pulse time to the ionization time. This is illustrated in Figure 3.11 using an 80 nsec laser pulse with all other conditions identical to Figure 3.10, except that the column length is chosen as only 7 cm to match the absorption length at the lower final temperatures. The curves labeled "front" and "rear" refer to conditions

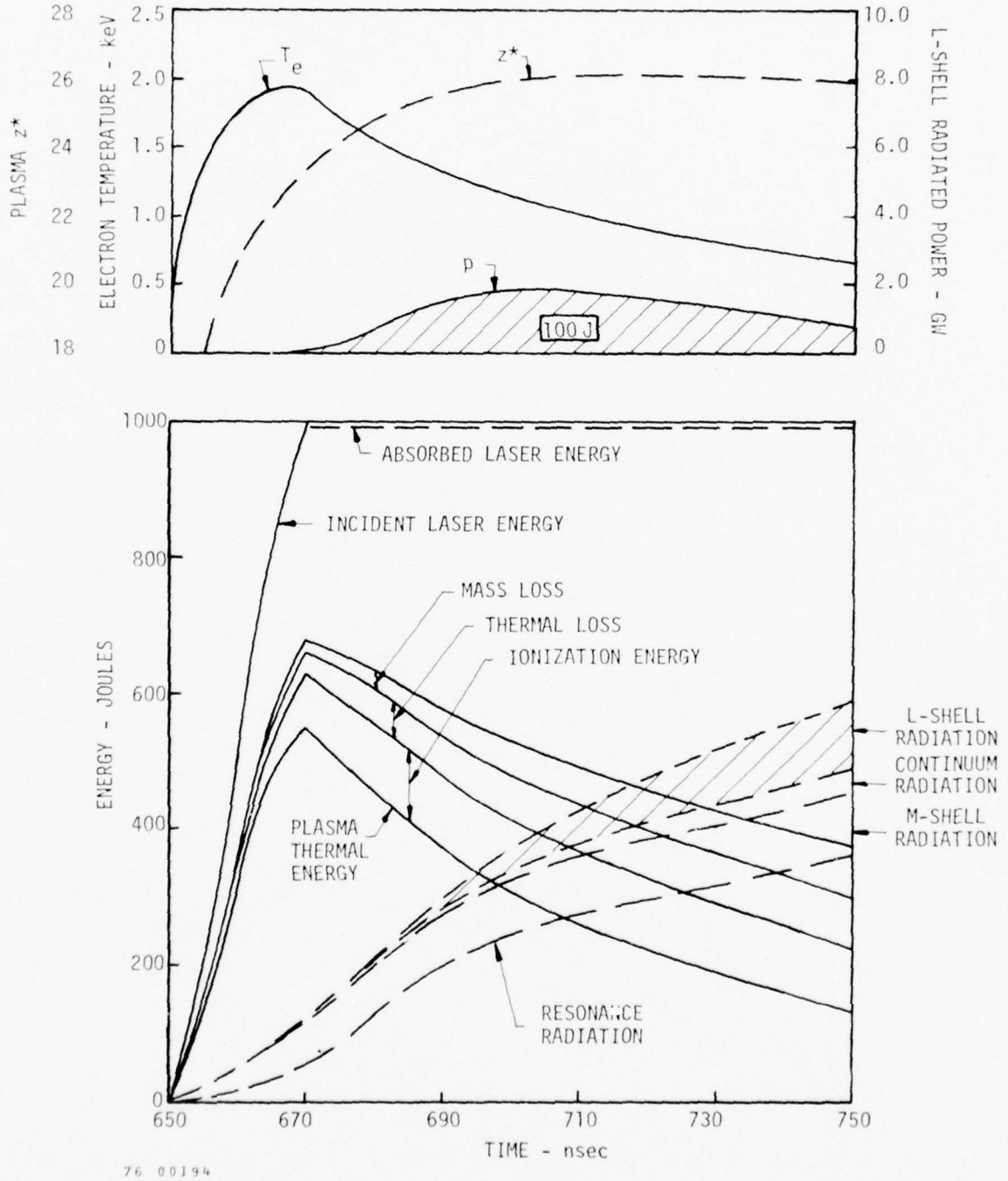


Figure 3.10. 20 nsec - 1 kJ Laser Heating of 10 cm Krypton Column

$\bar{N}_p = 0.0067$ $B_{peak} = 400$ kG $t_{1/4} = 750$ nsec

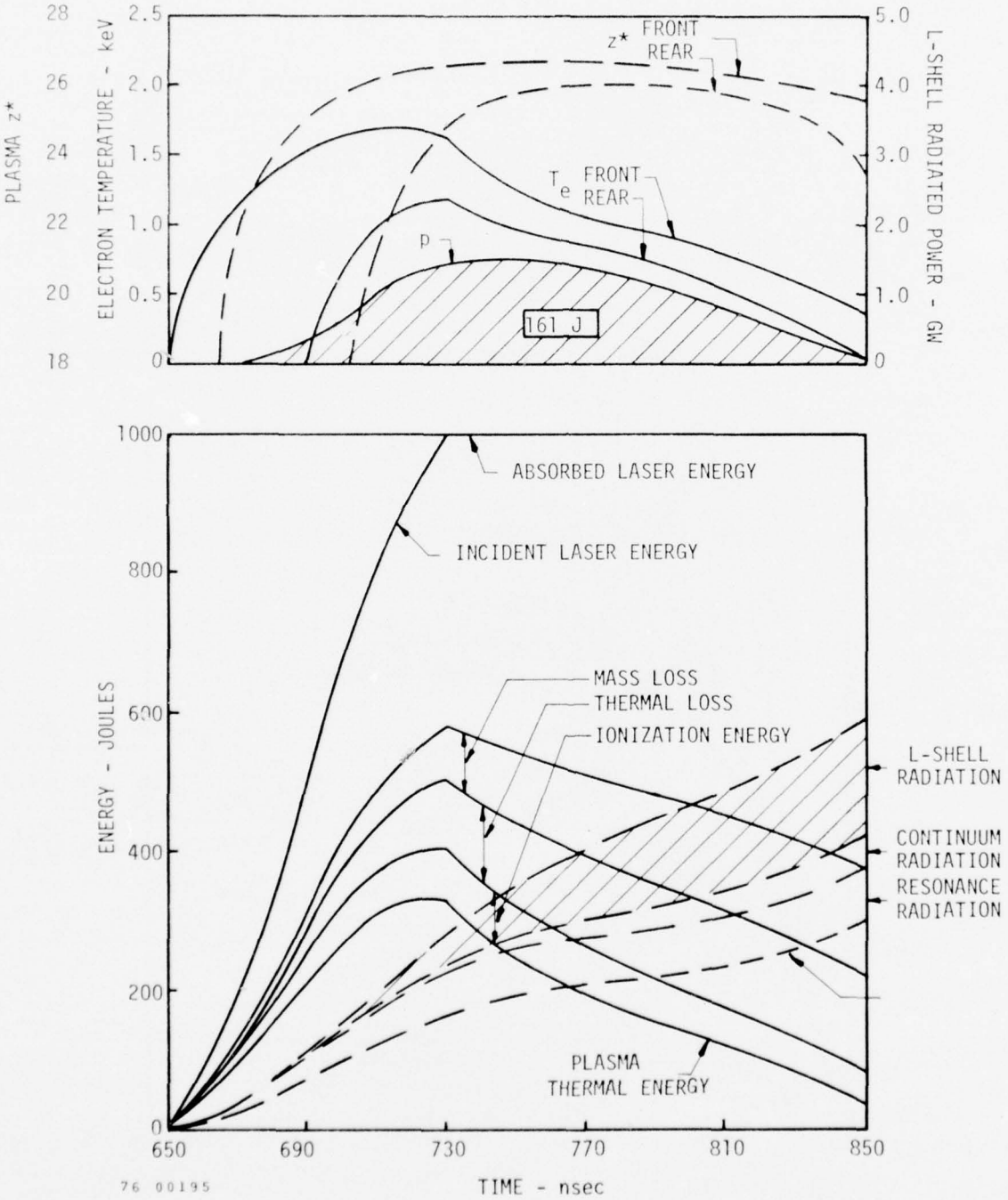


Figure 3.11. 80 nsec - 1 kJ Laser Heating of 7 cm Krypton Column

$\bar{N}_p = 0.0067$ $B_{peak} = 400$ kG $t_{1/4} = 750$ nsec

1 cm in from these ends, except for the "front" curve after the end of the laser pulse, at which time the column length has decreased by 1 cm in front and the actual front temperature and z* are plotted. Lesser amounts of laser energy are converted to thermal energy with the longer pulse time, but this energy is used more efficiently since peak temperatures coincide with peak plasma z*. However, the atomic physics model does not provide for inner shell "satellite" radiation from lower z states, and this would enhance the short pulse radiation. Most likely it is best to heat as rapidly as possible, and this will certainly maximize the peak radiation rate and minimize the rise time.

The calculation shown on Figure 3.12 is an attempt to simulate some actual heating experiments at much lower fields (160 kG) and lower laser energy (80 J in an 80 nsec pulse). The ion line density of $0.01 \times 10^{18} cm^{-1}$ and a stipulated initial ion density of $0.1 \times 10^{18} cm^{-2}$ correspond to an initial column diameter of 3.6 mm. The electron density increases upon heating due to ionization, but the column area remains nearly constant, and the plasma β remains low. For the assumed 80; laser spike with a 500 MW tail, the front of the plasma column reaches a steady temperature and ionization level. The heating wave progresses into the column at the same rate as the area wave and quasi-steady conditions are reached. Thus, after the initial spike, all radiation rates are constant and the radiated energy curves are straight lines.

The degree of ionization reached is only 15, which corresponds to the $3d^3$ configuration. The plasma is thus in a condition where the radiation rate is decreasing strongly with increasing temperature and ionization (due to the $\Delta n = 1$ f-number dependence in Table 3.5). The laser absorption rate decreases less rapidly in this regime, and exceeds the radiation rate. The quasi-steady temperature reached is only a

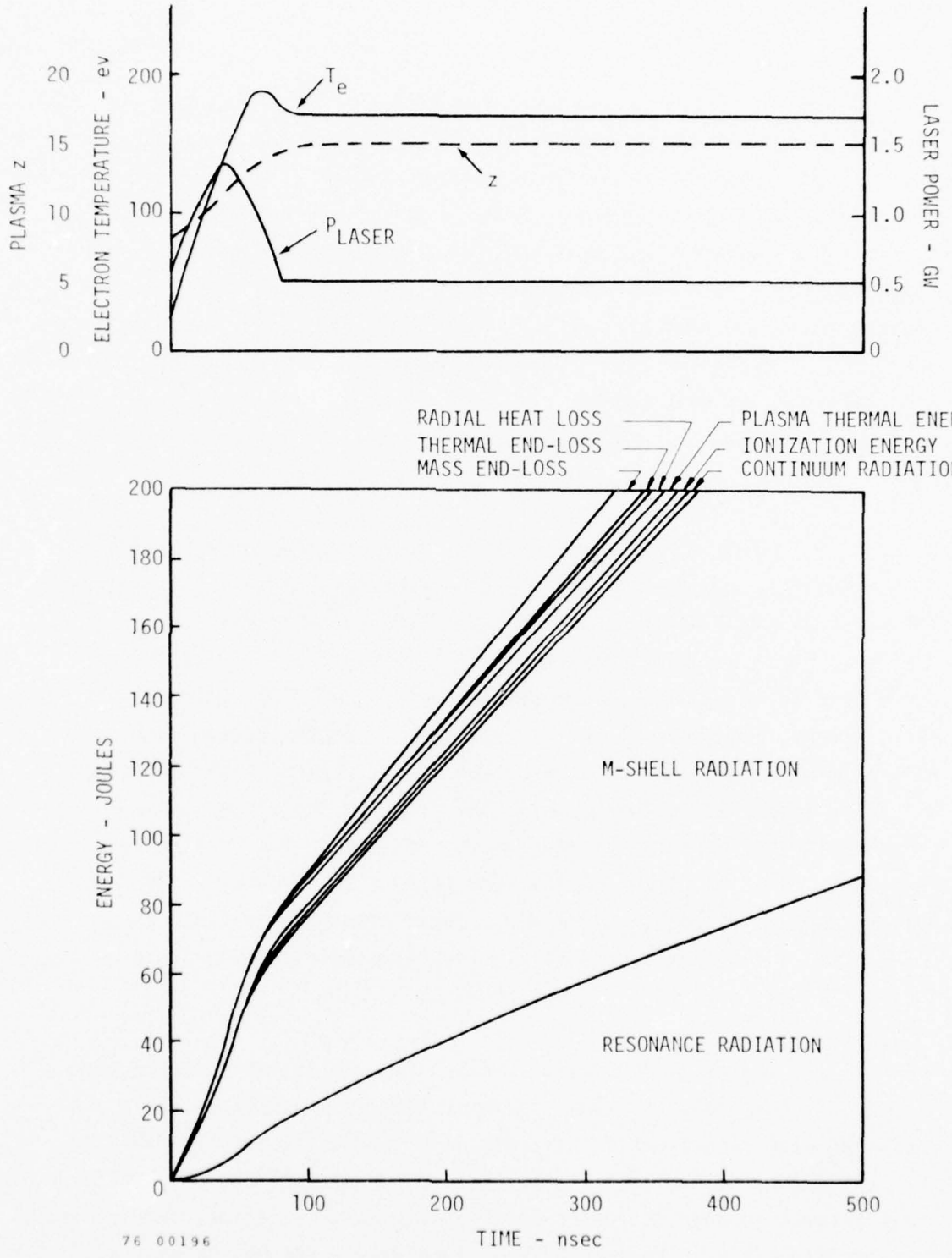


Figure 3.12. Numerical Simulation of Laser Heated Krypton Experiment

B_{max} = 160 kG AREDFCT = 0.5

N_p = .01 x 10^{18}/cm BBMFCT = 20

reflection of the time the plasma is heated before it escapes out the end. The soft radiation emitted at between 81 and 264 eV will not be detected by thin foil-XRD combination detectors, and any detected signal should be due to continuous-recombination radiation.

SECTION IV

THETA PINCH OPERATION

The design of the theta pinch in its Phase I and Phase II configurations has been discussed extensively in References 1. In the course of plasma heating experiments discussed in this report, it was discovered that the central magnetic field strength in the 10 cm long by 3.3 cm diameter theta pinch coil was actually lower than had been previously assumed. A careful series of magnetic field measurements was made, taking special care to control the dimensions of the magnetic probe, and to calibrate the integrator and oscilloscope carefully when taking measurements. The linear dimensions of the search coil could be controlled to within a few percent, thus giving a probe calibration accuracy of about five percent, and an overall accuracy for the probe, integrator, and scope of better than ten percent.

The result of this series of measurements is shown in Figure 4.1. The peak field measured in the 10 cm pinch coil was 90 kG with the capacitor bank charged to its maximum operating voltage of 65 kV. In contrast, the value of the peak field for these conditions was calculated in Reference 1 using linear circuit theory and a constant damping resistance of 5 mΩ to be 117 kG. The 5 mΩ value of the damping resistance was determined from the long term damping constant 2L/R. The large discrepancy between the calculated and measured field on the first quarter-cycle has proved to be quite difficult to explain satisfactorily.

Possible explanations for this observation include (1) measurement error from some as yet unexplained source, including a possible offset of the oscilloscope baseline at t = 0 on the pinch cycle, (2) resistive behavior of the pinch switches during the first quarter-cycle, and (3) lack of sufficient synchronism in the firing of the pinch switches, resulting in large circulating currents in the capacitor bank and a low current delivered to the load.

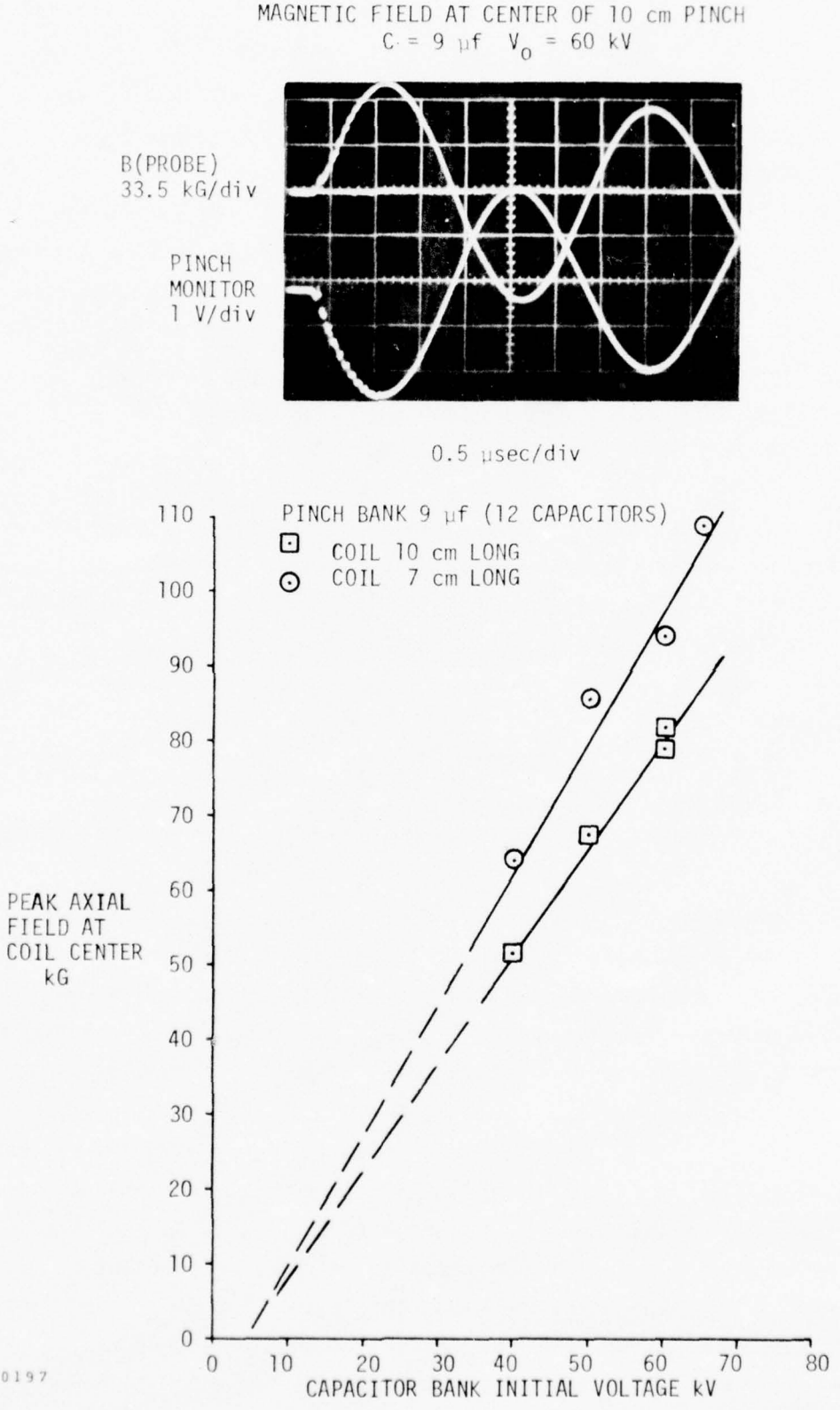


Figure 41. Theta Pinch Performance with 10 cm x 3.3 cm Diameter and 7 cm x 3.3 cm Diameter Coils

These possible explanations for the low field observation were explored in several ways. Experiments were done in which a "zero area probe", i.e., the entire magnetic probe assembly including twisted pair leads shorted at the probe location, was inserted in the pinch coil. This should test for the effect of stray electrostatic pickup and any ground loop in the measuring circuit. The maximum signal seen under normal pinch operation was only 1 percent of the normal probe signal; however, about half of this signal was in the form of a DC offset. If this offset were caused by a nonlinear response of the oscilloscope to high frequency noise, it might have been more severe with the probe loop in place.

The second possibility, that of resistive switch behavior, was explored by modeling the circuit behavior using a time dependent resistance. The circuit equation was solved in finite difference form on a computer using the following lumped circuit parameters:

V_o = 60 kV
C = 9 μf (12 0.75 μf capacitors)
L_T = 0.024 μh (10 cm pinch)
$R_T = .0833(0.06 + 0.5\ e^{-t/0.75})\Omega$

The time dependent resistance value was chosen with a constant 5 mΩ component to agree with the observed long time decay constant of the pinch bank of 9.5 μsec, with the exponentially decaying part chosen to provide agreement with the early time period and peak amplitude. The resistance coefficients in the parentheses are, of course, those for a single switch.

The result of this calculation is shown in Figure 4.2, and may be compared directly with an experimental waveform plotted from the oscilloscope trace shown in Figure 4.1. Agreement is quite good on the first quarter-cycle peak, and at the zero crossing points. The subsequent peaks, however, are much higher than predicted, indicating that this model does not offer the complete explanation. Possibly a combination of resistive switch behavior and lack of switch synchronization explains the observed result.

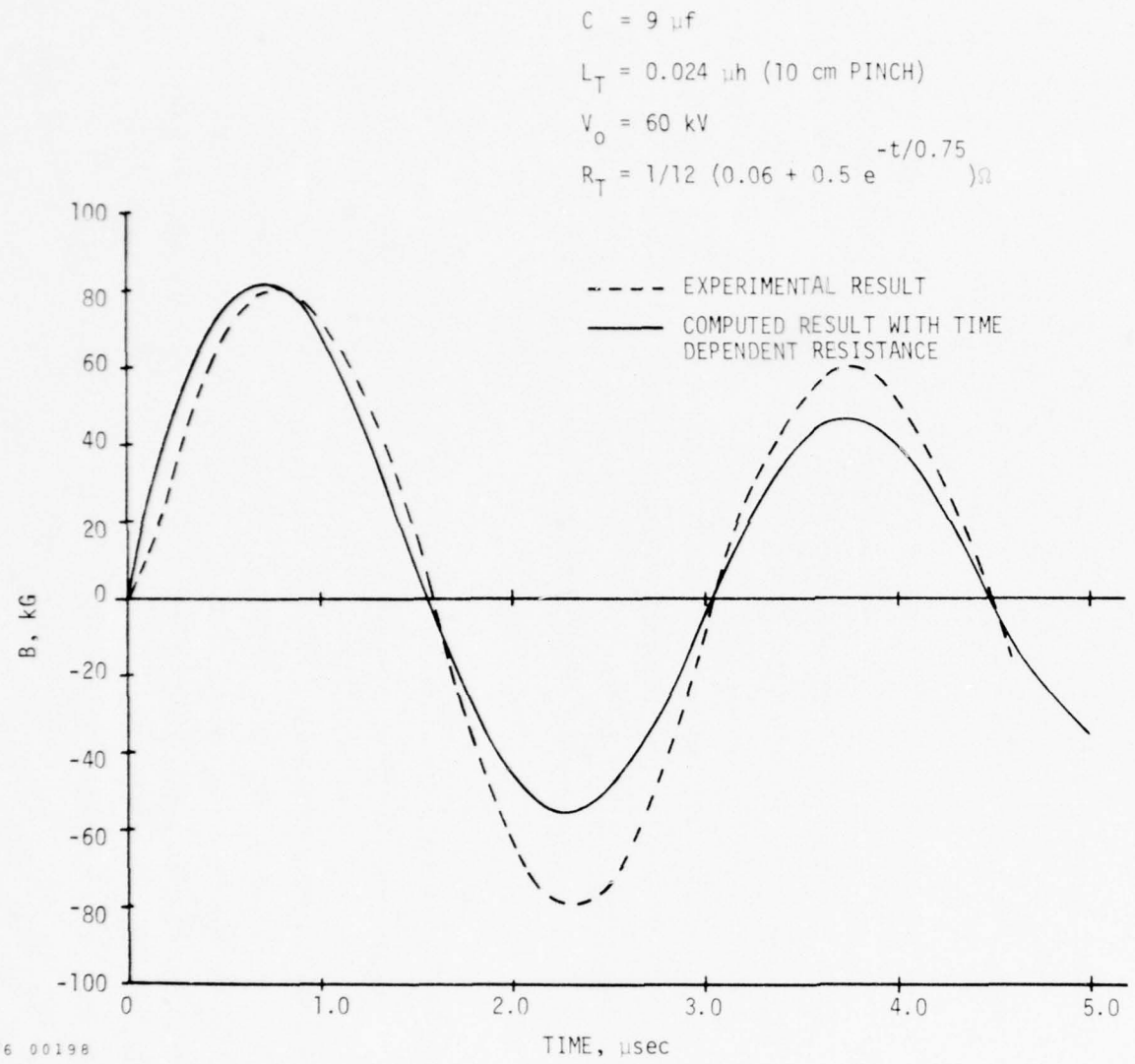
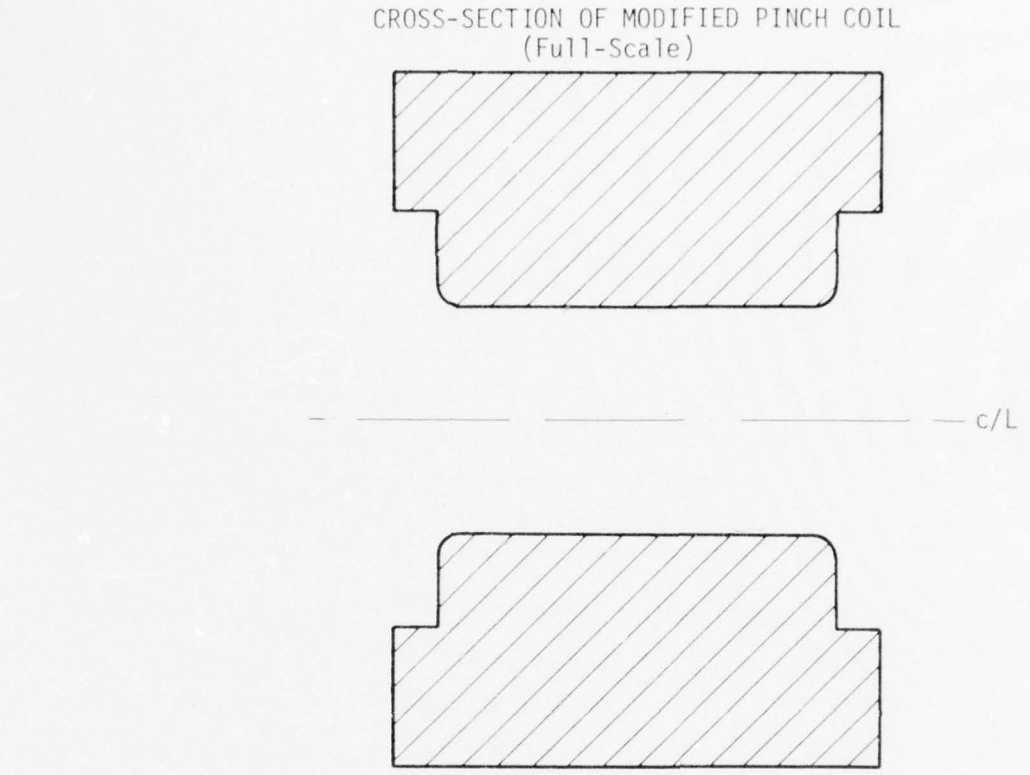


Figure 4.2. Comparison of Experimental Theta Pinch Waveform with Result Computed Using Time Dependent Resistance

In any case, it was decided to accept the low value of the peak field in the theta pinch as correct and to modify the coil by shortening it in order to increase the line current density and thus the peak field. At the same time, changes were incorporated in the profile to allow closer placement of the ends of the pinch to the ends of the coil, by allowing space to fold the insulating material from the feed slot. The resulting profile is shown in Figure 4.3. It consists of a 5.7 cm long straight section of 3.3 cm bore with a 6 cm diameter by 0.65 cm deep counter bore on either end for insulation space. The overall length of the coil block was shortened to 7 cm. The coil profile, along with the resulting field profile on the center line, is shown in Figure 4.3.

These changes in the coil geometry increased the quarter-cycle time to 825 nsec compared to a quarter-cycle time of 770 nsec for the old 10 cm coil. These figures, which were obtained with the 9 μf capacitor bank imply a total inductance of 26.8 nh for the bank with the new coil. The peak field in the center of the 7 cm coil is shown in Figure 4.1 as a function of initial capacitor bank voltage. The fact that neither line on Figure 4.1 extrapolates to the origin is additional evidence that an excess resistive drop occurs in the switches. A further discussion of the performance of the pinch bank with various load devices is given at the end of Section V.

Before using the modified theta pinch coil in plasma heating experiments, end-on image converter camera pictures were taken of the neon plasma produced on the first quarter-cycle. These pictures verified that the plasma produced by the shortened coil assembly was not substantially different from that produced in the 10 cm long coil and which was analyzed in some detail in Reference 1. In particular, a symmetrical collapse of the pinch plasma occurred with a density minimum on-axis. The density minimum persisted at least until the first quarter-cycle peak, thus allowing laser heating with a favorable density profile.



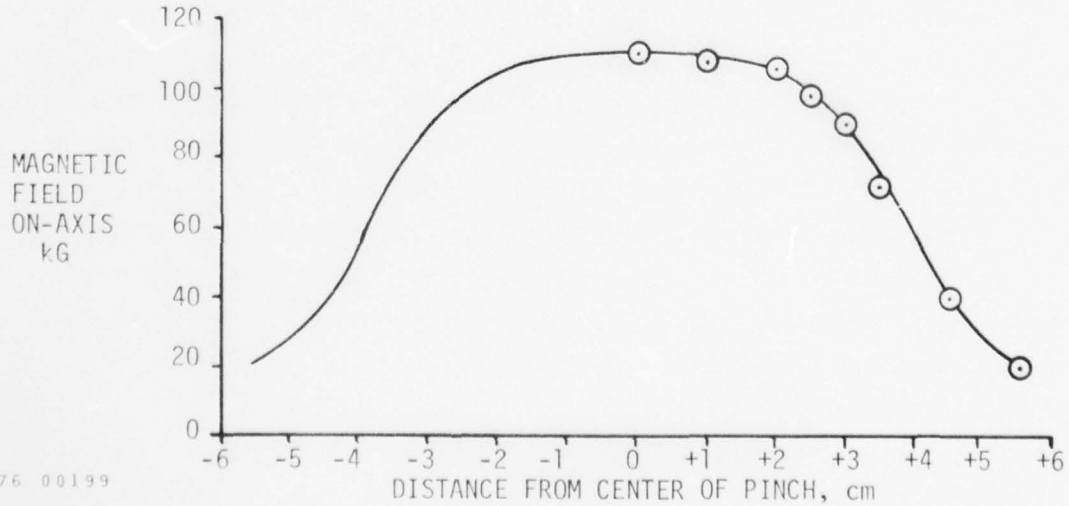


Figure 4.3. Field Profile of Modified Theta Pinch; C = 9 μf (12 Capacitors, V_o = 65 kV).

SECTION V

HIGH FIELD SOLENOID OPERATION

1. Design of Fast Solenoid

An option included in the Phase III laser heating program was that of using the existing capacitor bank to drive a multi-turn fast solenoid to make more efficient use of the bank energy and produce peak confinement fields approaching 300 kG. It was decided to use this option to increase the confinement field rather than the more expensive option of increasing the size of the capacitor bank.

Although the operation of pulsed, high field magnets in the 300 kG range is now routine, the construction of a solenoid to operate at the high voltage levels (65 kV) of the capacitor bank presented some unique design problems. A 300 kG magnetic field produces a "magnetic pressure" $B^2/2\mu_0$ of about 3600 atm acting on the enclosing conductors. This pressure can be statically confined using conductors of high strength steel or beryllium copper without great difficulty. The difficult problem, in this case, was to support the axially compressive force on a multi-turn solenoid. Conventional solenoid magnet design supports this force by using a high strength, rigid insultating material between turns of the magnet, and uses precompression of the coil to prevent motion of the conductors and consequent damage to the insulation. In the present case, the 65 kV operating voltage and 17 kV turn-to-turn voltage for a 4-turn coil forced the use of a continuous layer of either solid or liquid insulating material in the current feed to the coil and between turns. Additionally, a precompression scheme would restrict access to the end of the coil and compound the ablation problem discussed in Reference 1.

The design that was decided upon is shown in Figure 5.1. The 4-turn helical conductor was fabricated of type 1144 steel by milling a slot of the shape shown in a piece of cylindrical stock. The ends were made as

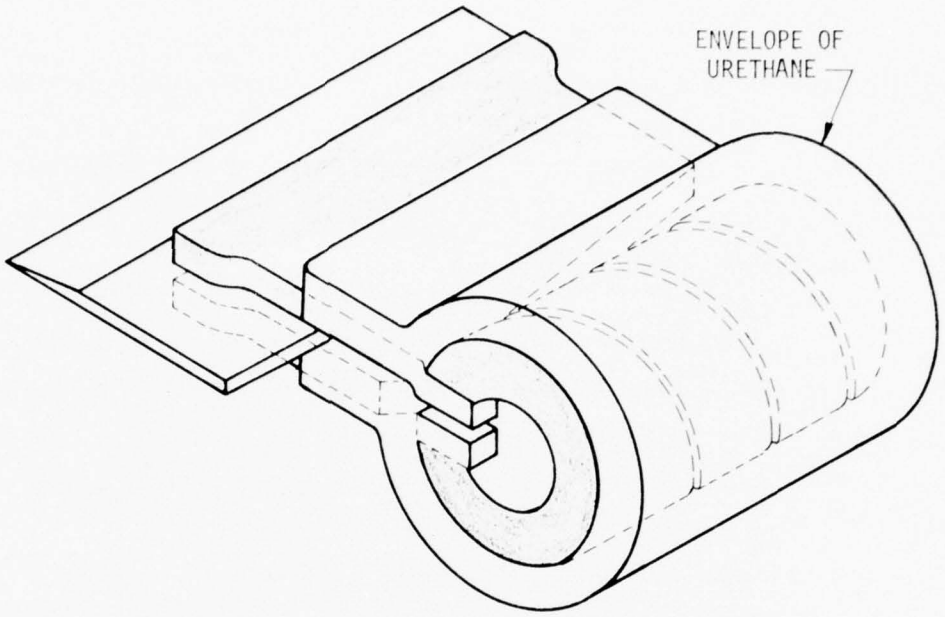


Figure 5.1a. Perspective Drawing of Fast Solenoid Including Urethane Envelope

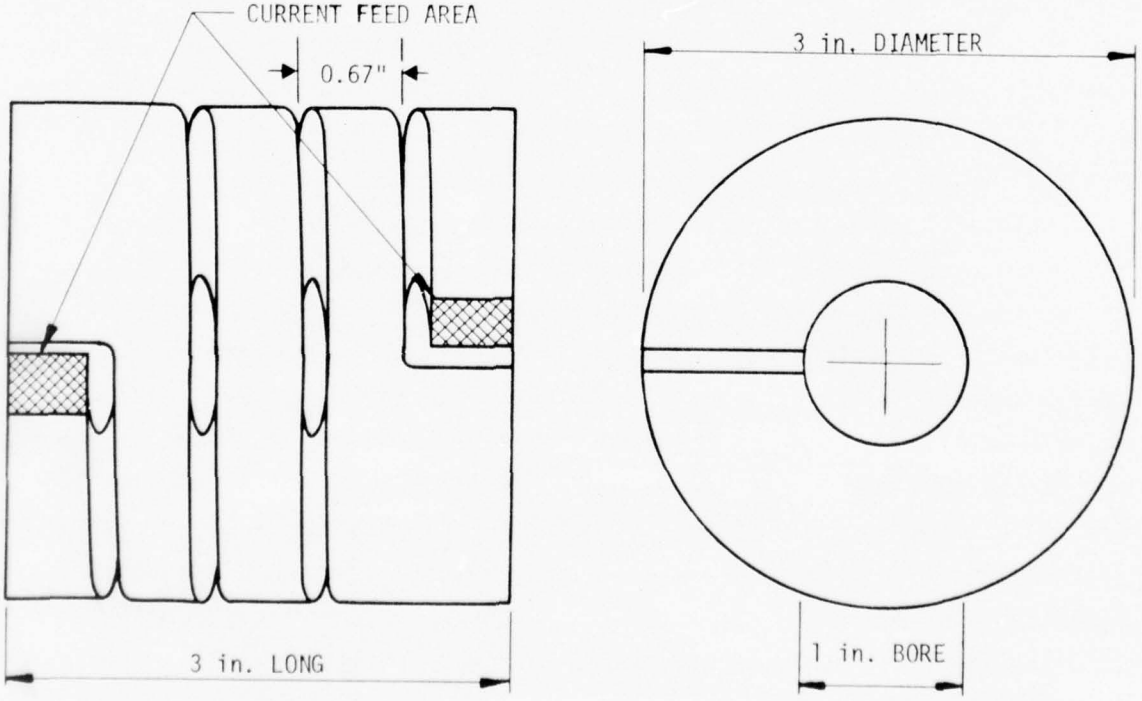


Figure 5.1b. Drawing of Helical Conductor of Steel for Fast Solenoid

shown instead of using a true helix in order to improve the field uniformity in this region. This design is suggested by flux conservation and was tested using foil models before construction of the full-scale device. The current feed plates were made of the same material as the coil and were attached by TIG welding.

The insulation was vacuum cast in place in the form shown in Figure 5.1.a. This arrangement completely enclosed the conductor except at the faces where it was bolted to the collector of the pinch bank. A "fin" of insulating material extended into the space between the feed plates and allowed a transition to the layered mylar insulation used there. A rigid insulating material, Dupont Urethane LW 570, cured with 24 percent MOCA, was used. Although the mechanical properties of this substance are not very well defined, estimates based on a compressive modulus of 7×10^4 psi, which is obtainable with this type of material, showed that it could absorb the impulse produced on the conductors during a 10 μsec pulse at 300 kG without damage. This construction solved the problem of insulation and mechanical support against compressive forces with one material and, at least for the field levels that were attained, eliminated the need for precompression.

2. Modification of Capacitor Bank

It was considered desirable to control the ringing of the capacitor bank when used with the fast solenoid for several reasons. Ringing of the current in the solenoid would contribute to the total mechanical impulse on the conductors and increase the possibility of mechanical damage to the insulation. Additionally, ringing of the discharge continues the deposition of j^2/σ power in the conductor and increases the chance of thermal damage to the adjacent insulation. Finally, ringing of the discharge was found in Reference 1 to cause additional ablation damage to the ends of the pinch tube with consequent damage to the focussing optics and instrumentation. Clamping the discharge at the current maximum would do little to solve the first two problems caused by ringing; therefore, it was decided to add damping after the half-cycle. This was done by switching a parallel

damping resistor across the LC circuit at the half-cycle time. The resistance value was chosen equal to the circuit impedance, $\sqrt{L/C}$, of about 100 mΩ.

The schematic diagram, Figure 5.2., shows the method used to add the switched parallel damping to the capacitor bank. An additional Veradyne spark gap, connected as shown to a large coaxial copper sulfate damping resistor, is connected to the collector plate assembly with 6 low inductance cables with an average length of 5 ft. The midplane of the spark gap is biased at - 20 kV so that when the main switches fire, - 60 kV is applied to the upper electrode and an approximately uniform field gradient exists across the gap. At the end of the first half-cycle, the voltage on the upper electrode of the spark gap is about + 60 kV so that at this time the upper gap is stressed to about 80 kV. It was hoped that this would be enough to self-trigger the gap, but it was found necessary to use a weak trigger pulse at the end of the first half-cycle. Even so, the operation of the damping switch was somewhat unreliable. Reliable operation was obtained only for the first ten or so shots after the switch had been cleaned and re-assembled, but operation of the switch became progressively more unreliable as it "aged". This problem could be corrected by using a high energy trigger device as is standard with these switches. Otherwise, the damping device performed quite well, as can be seen from the current waveforms shown at the top of Figure 5.3. The decay time constant 2L/R was reduced by at least a factor of 3 by using switched damping, while, of course, the first quarter-cycle peak was not changed.

3. Fast Solenoid Performance

The fast solenoid was operated at initial charging voltages between 45 kV and 60 kV. Below 45 kV, reliable triggering of the Veradyne switches in the pinch bank could not be obtained, and above 60 kV, frequent switch explosions due to insulation failure resulted. The reproducibility of the current waveform was not as good as in the case of the theta pinch because, due to the larger load impedance of the solenoid, synchronization of the

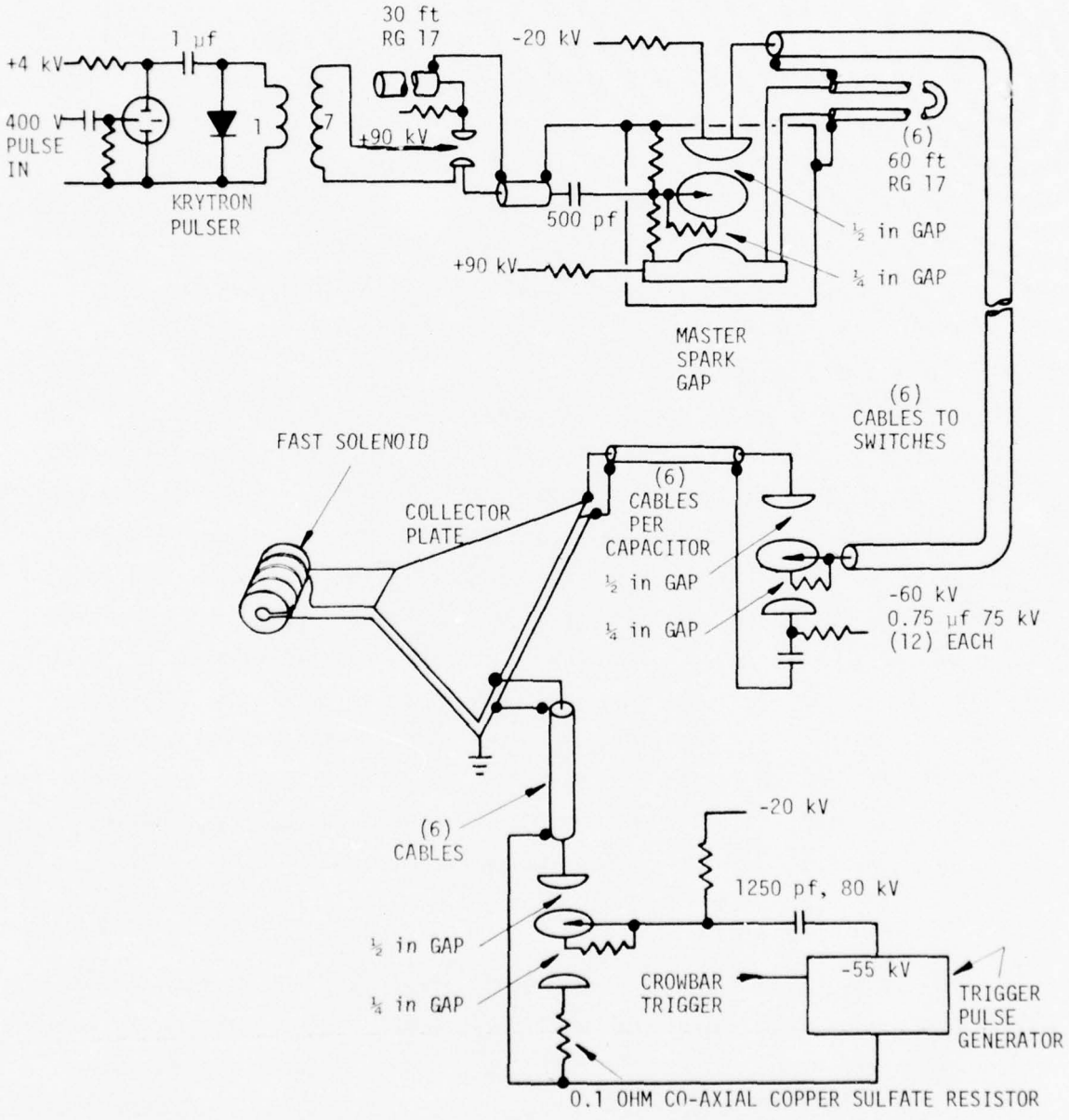


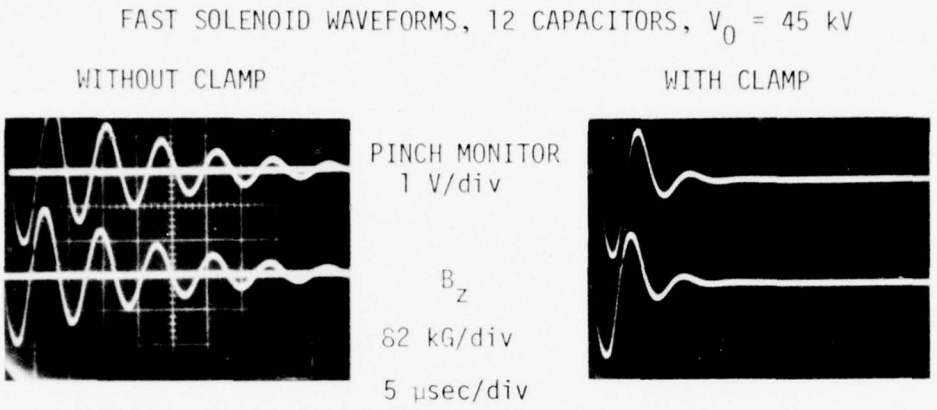
Figure 5.2. Schematic of Capacitor Bank and Clamp Circuit for Fast Solenoid

switching in the pinch bank becomes more critical. Frequently, current waveforms were seen in which one or more of the switches fired after the first quarter-cycle peak had been reached. This problem could be corrected only by extending the cables connecting the capacitors to the collector to allow a longer time $2\ell/c$ between the firing of the first switches and the cancellation of the voltage across the rest of them. It was not a sufficiently serious problem to justify this expense, and thus was controlled by careful monitoring of the current waveform. The quarter-cycle period of this device was 2.0 μsec, indicating a total system inductance of 180 nhy. This will be discussed in more detail at the end of this section.

The magnetic profile in the solenoid was measured on-axis, using the magnetic probes and methods discussed in Section IV. The results are shown in Figure 5.3. As in the case of the theta pinch, the peak field on the first quarter-cycle was considerably below the predicted value, although analysis is more complex in the case of a multi-turn coil with an unknown current distribution. As was expected for such a short solenoid with a steep pitch, the field has a peaked profile, down by about 40 percent at the ends of the coil. For comparison, the field distribution on-axis is calculated from the helix relation[12],

$$H_z = \frac{1}{4} H_\theta \cot \frac{P}{\pi a} (\cos \phi_2 - \cos \phi_1) \qquad (5.1)$$

where a is the helix radius, P is the distance between adjacent turns, and ϕ_2 and ϕ_1 are the angles subtended between the field point z, and the left and right edges of the helix ends, respectively. H_θ is the current sheet field given by $H_\theta = NI/h$, where N is the number of turns, I is the current in the winding, and h is the length of the coil. This function is plotted as the dashed line on Figure 5.3 for a current of 282 kA, which would be expected at 45 kV based on the measured circuit parameters. In this calculation h is taken as 4P, which is somewhat shorter than the 3" coil length due to the treatment of the ends. The extended ends tend to flatten the field profile and reduce the peak value, but not to the extent measured. As in the case of the theta pinch, the reason for the low



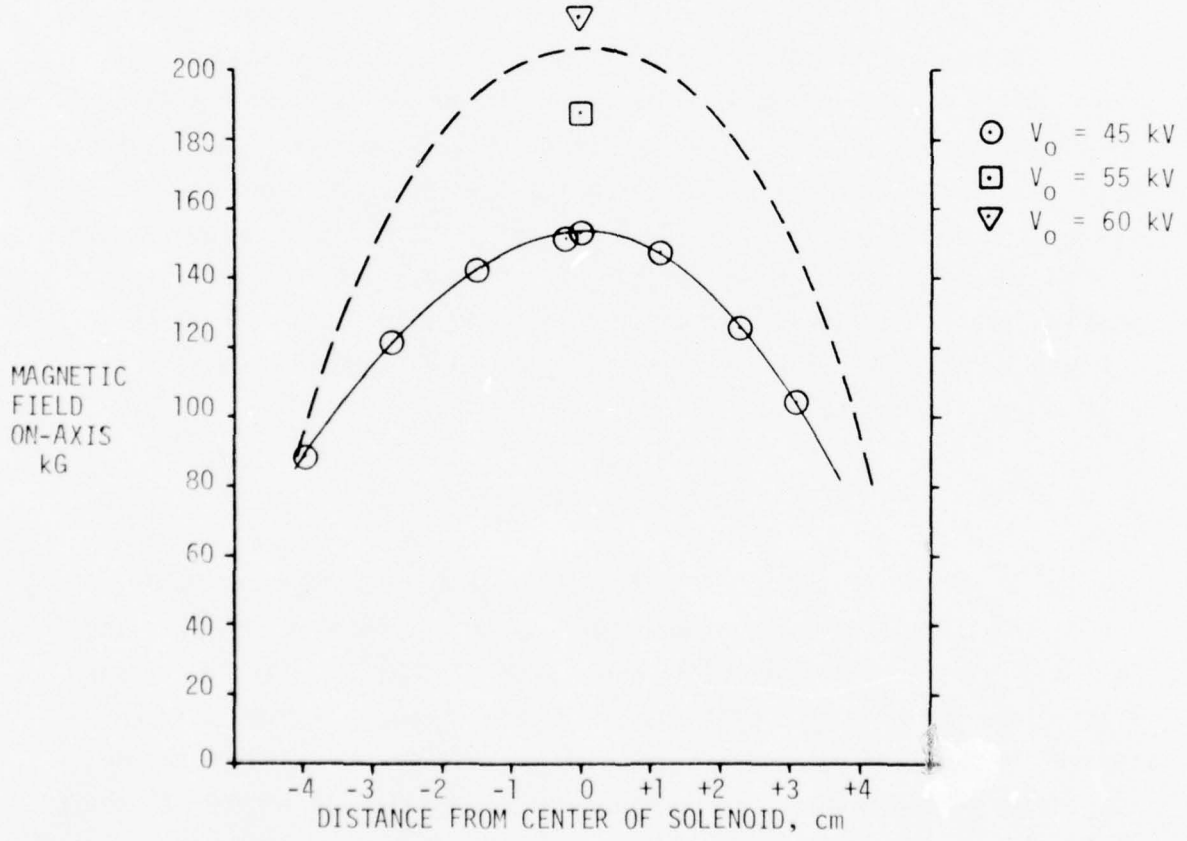


Figure 5.3. Field Profile of Fast Solenoid; C = 9 μf (12 Capacitors). For V_0 = 45 kV, dashed line is theoretical profile while solid line is the experimental profile.

76 00202

measured peak first quarter-cycle field is not well understood, but some or all of the reasons discussed in Section IV may apply to this case as well.

4. Summary of Pinch Bank Performance with Various Loads

In the course of the experiments discussed in this report, the same basic capacitor bank of (12), 0.75 μf, 75 kV capacitors was used with 3 different load coils. A comparison of the performance of the capacitor bank with different loads improves the assignment of inductive and resistive components to various parts of the bank and load. These performance characteristics are listed in Table 5.1. The coil inductance in the case of the two theta pinch coils is calculated using current sheet relations corrected for a current distribution obtained from potential theory as in Reference 1. The solenoid inductance calculation presents a more difficult problem, because in the multi-turn configuration the actual current distribution is unknown. An approximate calculation was made using a constant current density solenoidal model, but the effective length of the coil was taken to be 6.5 cm instead of the actual 7.5 cm length. This was done to account for the fact that part of the field correction region at the end of the coil has a lower net current density than the middle part of the coil. In this case, the coil inductance is $k_L \mu_o N^2 \pi a^2/h = 156\ k_L$ nhy for a coil 6.5 cm long x 2.5 cm diameter. The value of k_L is taken from Knoepfel[12] from the constant current density, thin current sheet relation to be $k_L = 0.8$, giving a coil inductance of 125 nhy. Two other sources of inductance are present in the solenoid assembly. The current feed inductance consists of a component associated with the parallel plate section 7 cm wide x 7 cm long, with a spacing of 0.7 cm, having an inductance given by the parallel plate relation $L_{pp} = \mu_o S\ell/h = 8.8$ nhy, in addition to the inductance associated with line currents parallel to the axis of the solenoid and the opposing line current in the plate assembly. This last component is approximated using the surface current, potential relation for opposing cylindrical conductors $L_\ell = \ell(\mu_o/\pi) \cosh^{-1}(S/d)$, where ℓ is the conductor length of 7.5 cm, S is the conductor separation of 1 cm, and d is the conductor diameter of 7.5 cm. This inductance is $L_\ell = 15.3$ nhy, giving a total coil feed inductance of 24.1 nhy.

Table 5.1

Performance Characteristics of Theta Pinch
Bank with Various Loads (12 capacitors, 0.75 μf each)

	LONG COIL	SHORT COIL	FOUR TURN SOLENOID
coil diameter (cm)	3.3	3.3	2.5
coil length (cm)	10	7	7.5
calculated coil inductance (nhy)	8.5	10.8	125
solenoid feed inductance (nhy)	---	---	24.1
collector inductance (nhy)	7.3	7.3	25.5
inductance of bank (nhy) (12 capacitors, 0.75 μf each)	8.3	8.3	8.3
total calculated inductance (nhy)	24.1	26.4	183
$\tau_{\frac{1}{4}}$ (long term measurement) (μsec)	0.73	0.77	2.0
total inductance (nhy) (based on period)	24.0	26.9	180
2L/R (μsec) (based on long term average)	9.6	8.0	18.3
R_T (mΩ)	5	6.7	20
I_{max} @ 60 kV (kA) (based on above)	1080	997	376
B_{max} @ 60 kV (kG) (assuming constant resistivity)	108	129	265
B_{max} @ 60 kV (kG) (measured)	80	98	214

Since in using the solenoid the separation of the collector plates is increased from 2 mm (as in the theta pinch coils) to 7 mm, the inductance of the collector plate assembly is increased by a factor of 7/2 to 25.5 nhy.

The capacitor bank inductance was determined previously in Reference 1, using various numbers of capacitors and noting that this part of the inductance varies as 1/n, where n is the number of connected capacitors. The total system inductance thus calculated is listed in Table 5.1, and may be compared with the value determined from the ringing frequency. The agreement is quite good.

The maximum current is evaluated, as in Reference 1, as $I_{max} = V/\omega L\, e^{-t_{\frac{1}{4}}R/2L}$, where R/2L is evaluated as the long term damping constant determined experimentally. With the peak current determined, B_{max} is evaluated, as mentioned earlier in Sections IV and V. As was discussed previously, the measured values fall about 20 to 25 percent below the calculated values.

5. Plasma Production in Fast Solenoid

The azimuthal electric field, which produces the initial plasma breakdown in the fast solenoid is somewhat lower than that available with the theta pinch. The voltage delivered to the coil is given by the ratio of the coil inductance to the total bank inductance, or $125/180 \times V_0 = 0.69\ V_0$. The voltage per turn at the inner bore of the coil is then $1/4 \times 0.69\ V_0 = 0.17\ V_0$, hence the azimuthal electric field at the solenoid bore is $0.17\ V_0/2.5\ \pi = 0.022\ V_0$ volts/cm. Since the azimuthal field is proportional to the radius, the field at the inner surface of the 1.4 cm diameter pinch tube is $0.012\ V_0$ or, for a 60 kV charging voltage, 0.74 kV/cm. This value is roughly half that obtained in the theta pinch; therefore, a series of image converter camera photographs were taken to determine pressure limits for prompt breakdown on the first quarter-cycle.

Prompt breakdown was found to occur in both Ne and Kr filling gases at initial pressures between 0.5 torr and 2.5 torr. Plasma implosion was

symmetrical in all cases and no evidence of plasma instability was seen, with the luminous plasma confined to the central region of the tube thru the first quarter-cycle peak at 2.0 μsec. The only noticeable difference from previous implosion experiments in the theta pinch was that the "hole" in the center of the plasma column closed up after about 700 nsec. This was verified in the plasma profiles determined by holographic interferometry shown in Figure 5.4.

Holographic interferograms were taken of the plasma produced in the fast solenoid for a variety of filling pressures and at various times during implosion and confinement phases. The holography was done using a ruby laser, hence the sensitivity was 1 fringe for a line density of 3×10^{17} /cm^2. Because the magnetic field in the solenoid is not constant with axial position, and because plasma end loss may be important for the later stages of the discharge, an assumption of uniform line electron density is incorrect. Since, however, there is no way of knowing the axial electron density profile, a constant density with a length of 7.5 cm was assumed in interpretation of the interferograms, and in general, the resulting numbers for electron density will be underestimates of the density in the region of maximum field.

Figure 5.4 shows interferograms and interpreted density profiles for both krypton and neon plasmas at 0.5 torr initial filling pressure. Neon behaves much as it did in the theta pinch, except that the weakly ionized hole fills in about 700 μsec. Possibly, due to the slower rise of the magnetic field in this case, there is little trapped flux by the time breakdown is completed. Krypton showed very complex behavior. Very early is the implosion phase, the central region of the plasma tube shows a confused fringe pattern. This is thought to be due to photo-preionization of the neutral gas in the whole tube. At later times, the confined Krypton plasma has the peculiar "shoulder" in the density profile. This indicates a double current layer and persists through the first quarter cycle. Both the krypton and neon plasma reach maximum central line density at about 1.0 μsec and slowly decay by end loss over the

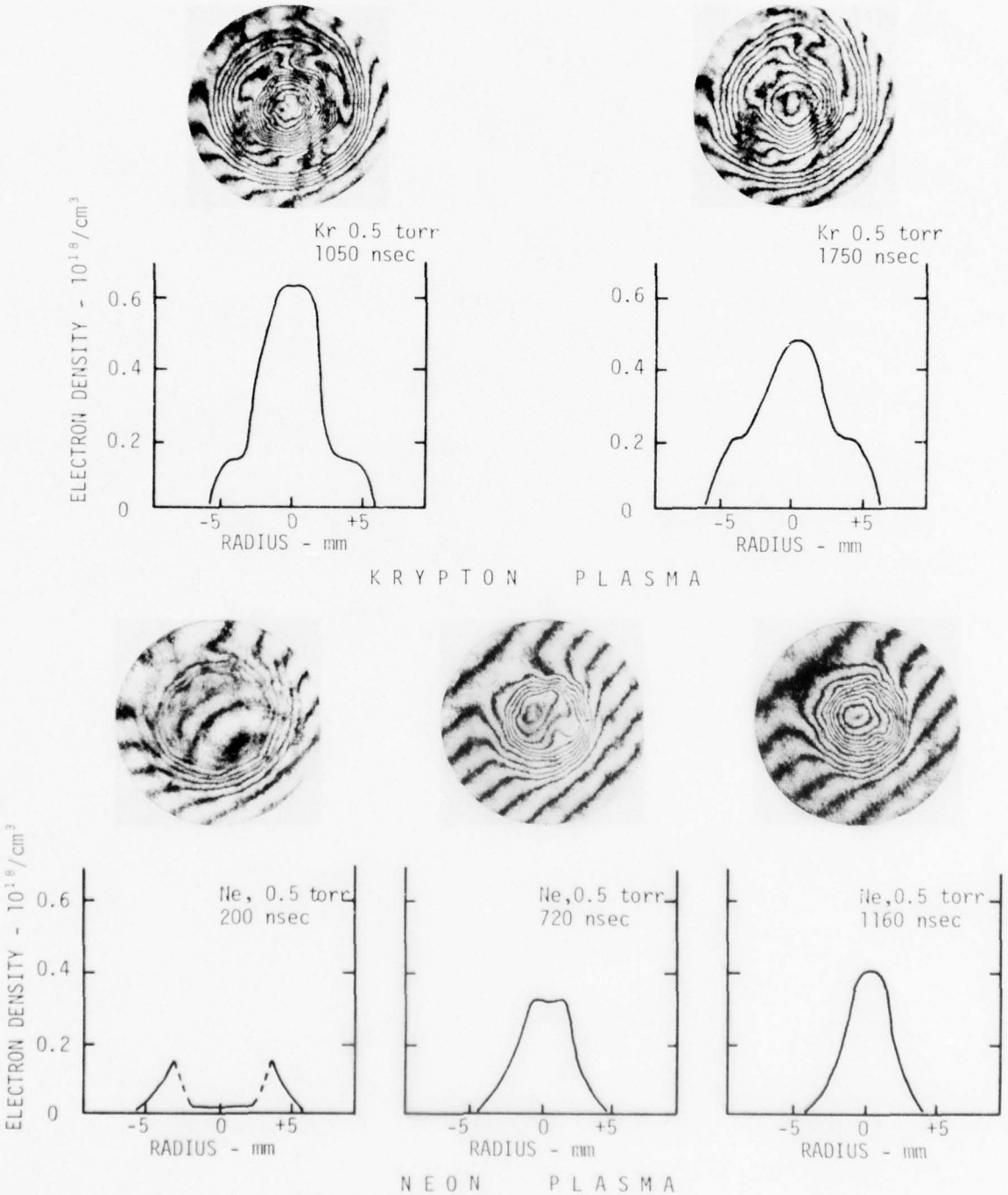


Figure 5.4. Unheated Electron Density Profiles at Various Times, Fast Solenoid, 60 kV, 1.4 cm Diameter Plasma Tube

76 00203

next microsecond. Neon decays by about 40 percent in this time, while decay with krypton is slower as one would expect. The neon plasma shown in Figure 5.1 appears to have an average degree of ionization of about 2.5 if one assumes the entire tube length to be at constant density and if it is assumed that all the gas initially in the tube is swept into the plasma core. This is about the same as was observed in the theta pinch earlier.

SECTION VI

LASER OPERATION

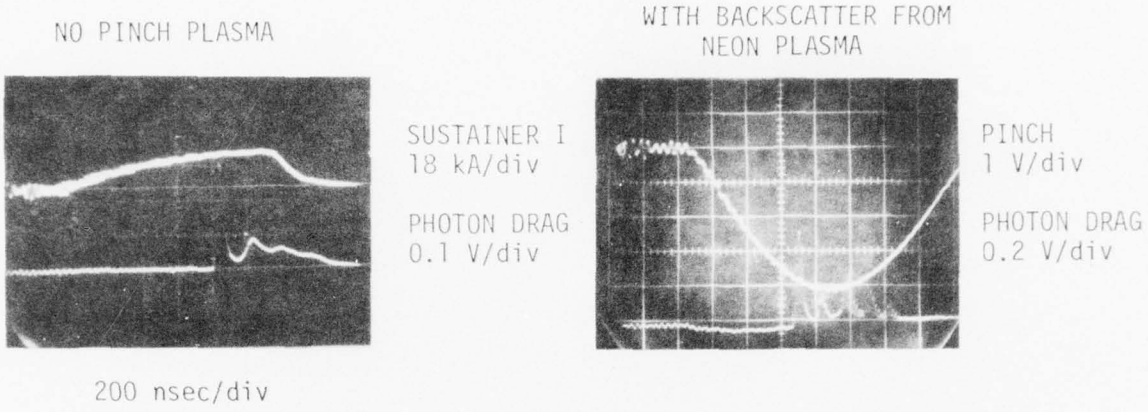
1. Quasi-Steady Performance

The behavior of the 10 liter cold cathode laser in the gain switched mode is discussed in Ref. 1. At 3¾ atm fill pressures, using 2/0/1 $He/N_2/CO_2$ laser mixes, 80J gain switched "spikes" were obtainable in 40 nsec FWHM Gaussian shaped pulses. Both the sustainer power supply (operating at Marxed voltages of 210 kV) and the e-beam power supply (operating at a Marxed voltage of 220 kV) were crowbarred immediately after the gain switched spike to minimize the energy in the "tail".

When the threshold behavior of the ionization-soft radiation process was recognized, it became apparent that strong K-shell emission required more energy than was available in the laser spike. It was also recognized that the lower power laser tail was sufficiently intense to heat the plasma which was already ionized by the spike. The laser performance was then investigated using a 3/½/1 $He/N_2/CO_2$ mix with electrical pumping continuing after the gain switched spike. The pumping time was limited to about 1.5 μsec by arcing or impedence collapse in the cold-cathode e-beam gun.

Figure 6.1 shows the results of these quasi-steady investigations. A typical laser output trace is shown on the upper left hand part. The long sustainer rise time is due to the relatively high (~1.75 μh) inductance of the Marx bank supply. The laser output exhibits a typical gain switched spike which saturates the laser medium and results in a weak second spike. (This spike is to be distinguished from the plasma induced mode locking shown to the upper right and discussed in Section VII). The intensity then reaches a quasi-steady value (for the trace shown, lasting only 100 nsec) until the sustainer and e-beam are crowbarred. The laser power is inferred from integrating the area under the photon drag trace, and measuring the total energy with a calorimeter.

TYPICAL LASER POWER OUTPUT RECORDS
WITH 3/½/1 MIX (PHOTON DRAG)



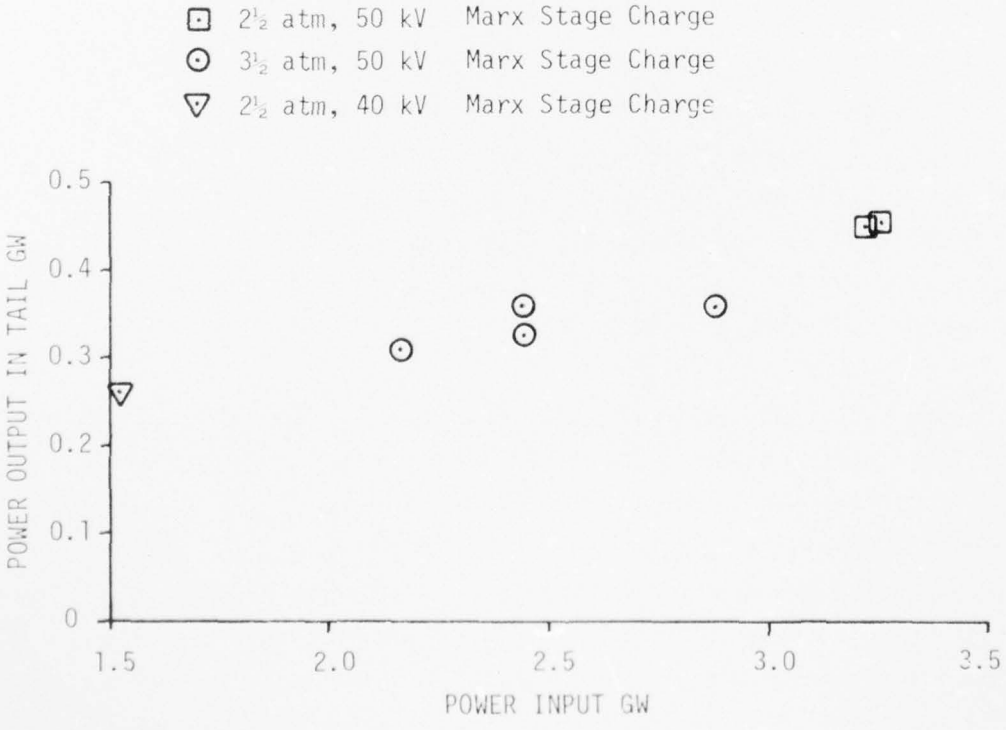


Figure 6.1. Laser Performance in Tail of Pulse with 3/½/1 Mix

76 00204

The laser input power is the product of the sustainer voltage and current. By the time the current has reached a steady value, the voltage across the 10 cm anode-cathode gap has dropped to about 2/3 the erected Marx voltage. Due to inductive drops this is actually near the maximum voltage ever applied to the sustainer. For typical charge voltages of 50 kV on the 3 stage Marx bank, 25 kA currents are produced at 100 kV gap voltages.

The results plotted on Figure 6.1 are typical with higher output powers achieved at lower pressures for the same applied voltage. This is due to the higher currents drawn and higher input powers at the lower pressures. The total currents are relatively low (considering the 0.4 a/cm^2 transmitted e-beam current) due to the low specific electric field values of 2.9-4.0 kV/cm-atm. These electric-fields are, however, high enough for efficient pumping. Typical quasi-steady efficiencies range between 12-17 percent, which is reasonable considering the fact that round optics are being used, and an inefficient sustainer electrode shape results in current fringing and electric field nonuniformities. Total quasi-steady powers of up to 400 MW have been achieved for times up to 1 μsec. Higher powers are possible at higher voltages (the maximum Marx charge is 75 kV), but optical damage to the salt output window then becomes a problem. At a 400 J output, the 10 cm O.D. by 3.9 cm I.D. annulus produces an average fluence at 6 J/cm^2, and probably peak fluences of 10 J/cm^2. Very careful alignment is necessary to keep hot spots from raising the peak fluence above this value. Chemical polishing of NaCl windows ia also necessary to avoid surface damage. However, with these two techniques, routine operation with both single crystal and polycrystalline NaCl at the 400 J level is possible.

2. Oscillator-Amplifier Experiments

Before switching to longer time scale laser operation, a considerable effort was expended to increase the gain-switched output spike energy above 80 J. A peaking capacitor was considered for the sustainer Marx bank to increase the initial pumping rate, but the results of previous work did not imply that this modification would produce the theoretically

predicted power increase.[1] Rather than rely on faster pumping, it was decided to develop the oscillator amplifier configuration discussed in Ref. 1. A schematic of the TEA oscillator and the 10 liter laser in an amplifier configuration is shown in Figure 6.2. By tilting the amplifier salt exit window to its maximum angle at 10 degrees from the optical axis, and placing a metal "spoiler" on the center of the AR coated germanium meniscus lens, it was hoped to increase the threshold for parasitic oscillations in the amplifier. However, the pumping time before parasitic oscillation began remained at the 1.4 μsec value we had previously achieved without the "spoiler". This can be compared with the 0.8 μsec time to lasing shown in Figure 6.1. The small signal gain reached was calculated to be between 3 and 3.5 percent/cm. An unevaluated source of parasitics is diffraction from the hole in the amplifier diagonal coupling mirror, but correcting this would involve considerable redesign of the amplifier.

Considerable effort was also expended on improving the TEA oscillator. The Rogowski shaped electrodes were replaced with flat electrodes with a 1/2 in.edge radius, and the preionizer sparks were electrically isolated from the main discharge to prevent arcing to them. A small amount of xylene was bled continuously into the laser to increase the degree of preionization. This did not increase the laser output, but improved the reliability. With these changes a reproducible, reasonably uniform 2.5 J-80 nsec annular output spike was achieved with a $4/\frac{1}{2}/1$ $He/N_2/CO_2$ plus 2 percent H_2 mix at 1 atm.

Measurements were then made along the oscillator-amplifier optical train as indicated in Figure 6.2(a). A photon drag detector viewing a split off portion of the oscillator exit beam was calibrated against calorimeter readings at position "A". Calorimetric measurements were then made at successive positions with the amplifier unpumped, and the fractional energy reaching each position is plotted in Figure 6.2(b). As noted, approximately 25 percent of the beam energy is lost in travelling the additional 94 inches from near the oscillator exit window to the amplifier entrance lens. This loss must be due to the divergence of undesirable high order modes in the oscillator.

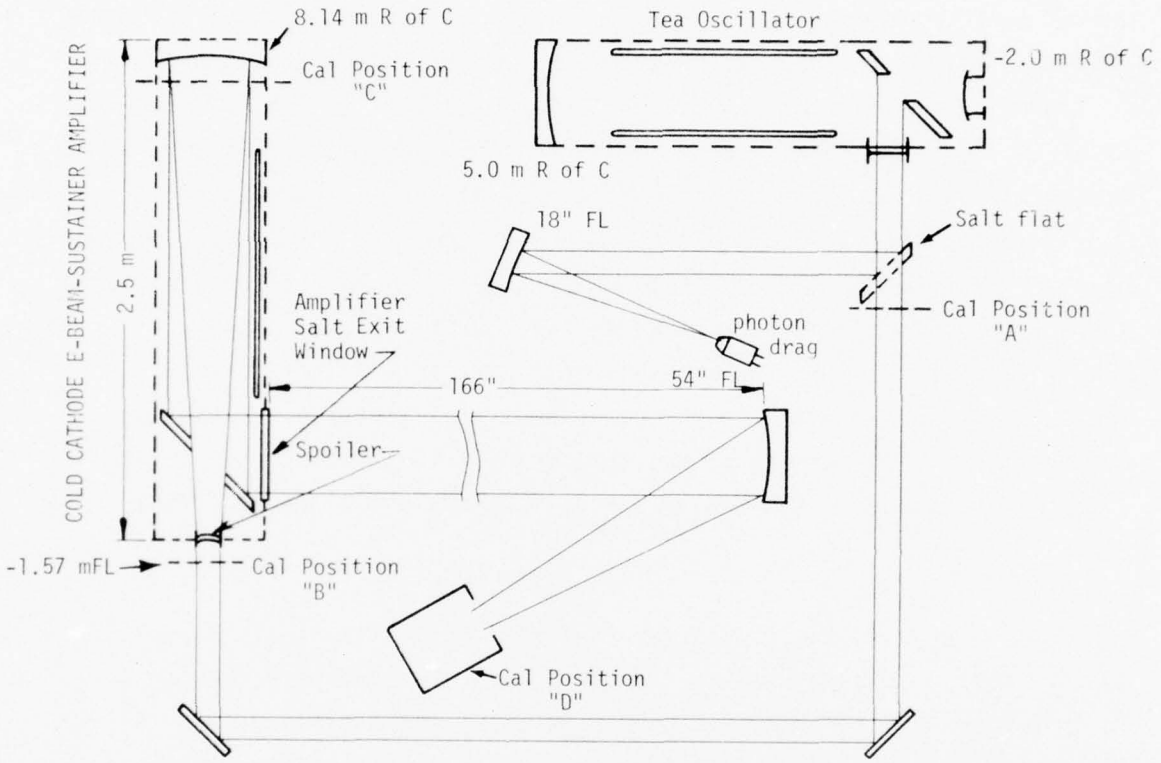


Figure 6.2(a). Schematic of Oscillator-Amplifier System Showing Calorimeter Positions

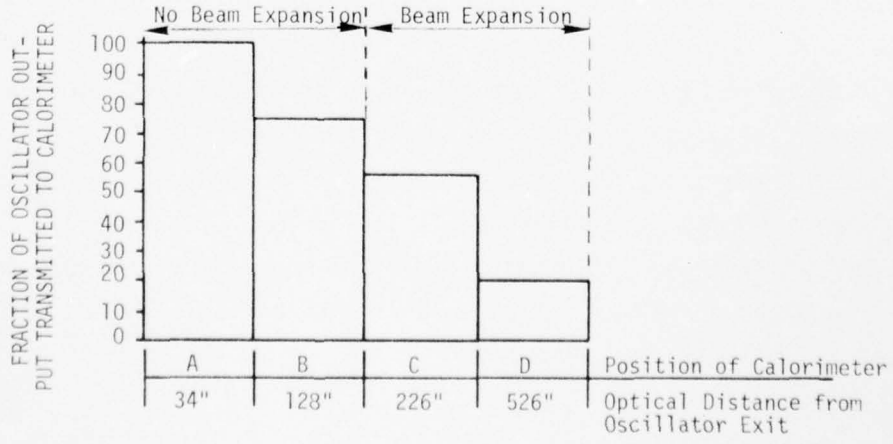


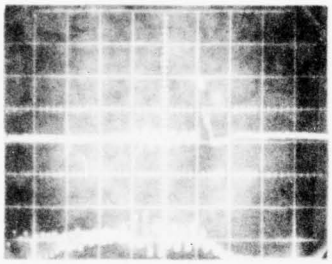
Figure 6.2(b). Histogram of Fraction of Oscillator Energy Recovered at Various Positions, Amplifier Inactive

A negative meniscus AR coated -1.57 m fl germanium lens is located at the same position in the amplifier configuration as a -1.57 m fl convex mirror would be in an unstable resonator arrangement, and the same 4.07 m fl mirror is used at the other end to recollimate the beam in a Cassegranian arrangement. The "spoiler" on the lens is 1.5 cm in diameter, equal to the ideal hole size in the annular beam from the TEA oscillator. The amplifier magnification M = 2.58 is only slightly larger than the oscillator magnification of M = 2.50, yet by the time the oscillator beam has reached the far amplifier mirror (position "C") it has decreased to only 55 percent of its original energy. On retraversing the cavity and exiting from the amplifier, additional diffraction and vignetting losses are incurred. The final output beam is slightly divergent and reduced to only 20 percent of the original TEA loss output energy. This latter loss is the most damaging since it occurs where the amplified beam will be strongest.

The above measurements were actually made after initial experiments with the total system to try to explain the poor performance. This performance is shown in Figure 6.3, where the overall 2 pass amplifier gain is plotted as a function of the amplifier electrical pumping time for two different input energies: 1) the standard TEA 2.5 J energy; and, 2) this energy attenuated in the central order by a factor of 10 using a 30 percent transmitting screen. The smaller scale variations in input energy were measured by the photon drag detector shown in Figure 6.2, and the output energy was measured by the calorimeter at position "D". The amplifier gain is defined as the ratio of measured amplifier output with electrical pumping to the value it would have (inferred from the previous discussion) without pumping. The measured diffraction and vignetting losses were thus accounted for in this round about fashion, which is strictly correct only when no saturation effects are present.

The maximum measured amplifier "gain" of 350 for the low input power corresponds to a small signal gain of 2.9 percent per cm. This is

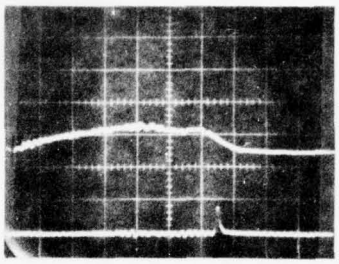
TYPICAL INPUT AND OUTPUT WAVEFORMS IN
OSCILLATOR AMPLIFIER EXPERIMENT



Oscillator
Photon Drag
0.2v/DIV

Sustainer I
0.05v/DIV

200 nsec/DIV



Sustainer I
0.05v/DIV

Amplifier
Photon Drag
0.2v/DIV
(attenuated)

200 nsec/DIV

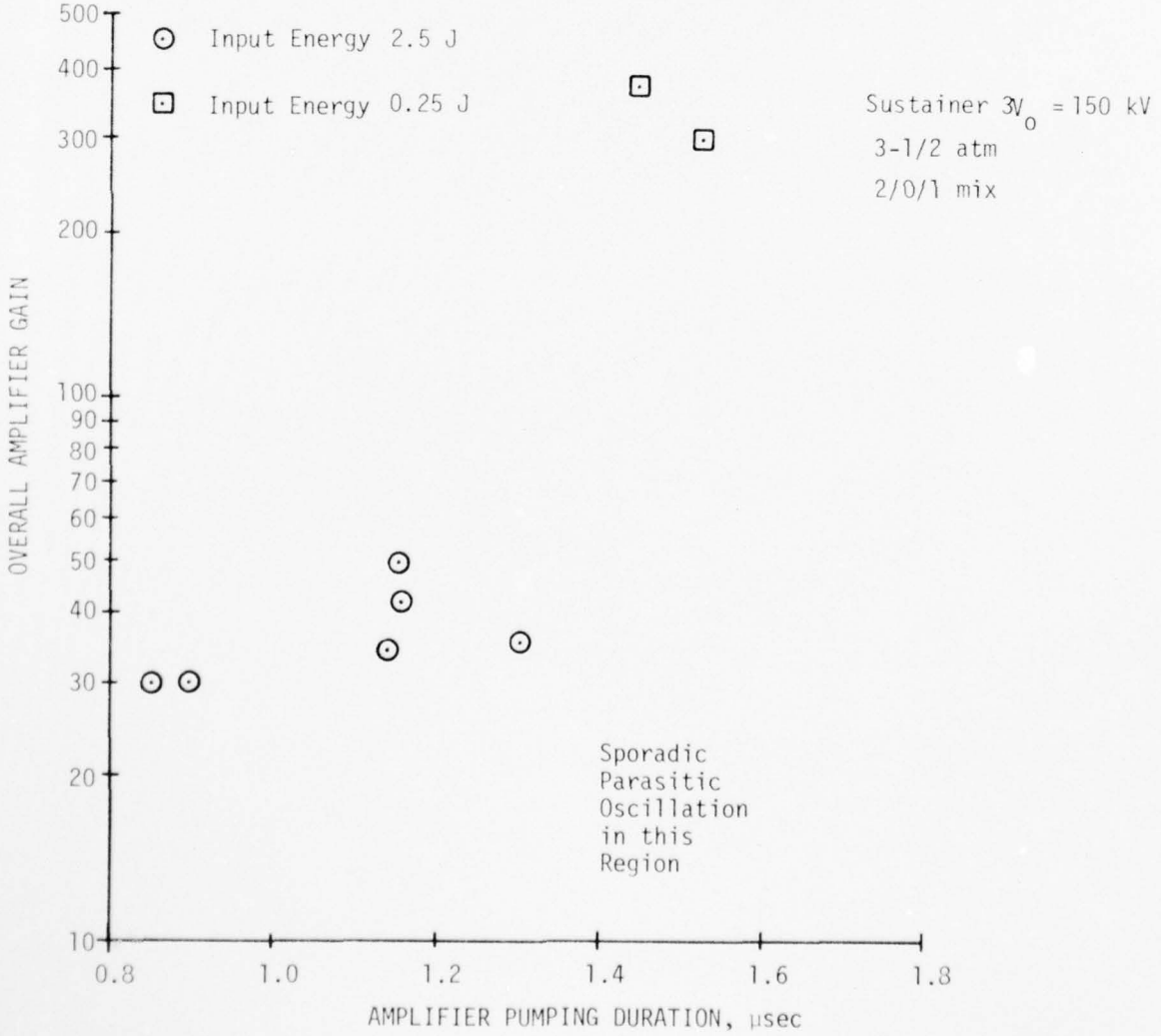


Figure 6.3. Large and Small Signal Gain Characteristics of Amplifier

in rough agreement with the calculated small signal gain, considering that some saturation effects may still be present. The higher input energy points definitely show the effects of saturation, and the highest measured gain of 50 would amount to a significant performance increase over the previous gain switched oscillator performance if not for the diffraction and vignetting losses. The actual maximum spike output obtained in the oscillator-amplifier configuration was only 30 J, and since considerable developmental effort would have to be expended to significantly improve this value, the straight oscillator configuration was returned to. It can be concluded that the development of an efficient tens of nsec oscillator-amplifier is certainly feasible, but it requires somewhat more effort than allotted in this program.

SECTION VII

LASER HEATING EXPERIMENTS IN THE THETA PINCH

1. Phase III Modifications

The Phase III modifications to the theta pinch are discussed in Section IV. These consisted primarily of shortening the pinch coil from 10 cm to 7 cm in length, in order to increase the maximum magnetic field available. Neon plasma heating experiments were done with both the 10 cm coil and the 7 cm coil.

In order to control the problem of plasma tube wall ablation, the alumina plasma tube was shortened to 4.5 inches when the 7 cm coil was in use, and the catchers were modified in order to keep the end-seal on the pinch tube as close to the pinch coil as possible. The recess in the ends of the coil, as shown in Figure 4.2, allowed the coil insulation to be folded flat, so that the end of the catcher assembly could be positioned flush with the end of the coil. In this way, the overhang of the tube beyond the coil could be reduced to 0.25 in., and ablation damage to the instrumentation and focussing optics could be minimized.

A major change in the laser heating experiments during Phase III was the development of a soft x-ray diagnostic system using silicon PIN x-ray detectors (XRDs), and aluminum and beryllium foil filters. This step was required when it became apparent that the gold thermopile calorimeters, (described in Appendix I) supplied by Stanford Research Institute (SRI), were much too sensitive to the fast pulsed magnetic field of the theta pinch to be useful. Additionally, the one inch square entrance foil area of these calorimeters proved to be much too vulnerable to blast damage from the pinch, even with the catchers installed.

As it was necessary to cluster several detectors at equal distances from the source, and close to the axis of the pinch, Quantrad 0.025 PIN-200 XRDs were chosen, primarily for their small size. The XRDs were mounted

as shown in Figure 7.1a, on a face-plate, which fastened to the SRI calorimeter package. A short length of 50 Ω microdot cable connects each detector to the BNC vacuum feed-through connectors provided on the SRI package. Each of the XRDs is mounted in a holder, also shown on Figure 7.1a. The holder consists of an aluminum plate containing an aperture to define an effective area for each XRD. The aperture is split into two parts to allow insertion of filter foils. The aluminum plate was fastened to a nylon cup, which served to hold the detector and insulate it from the face-plate and the rest of the pinch assembly. This was found to be necessary to eliminate ground loops and excessive electrical noise.

Provision was made to allow the XRD holders to be positioned at various radii, as shown in Figure 7.1a, in order to view selected portions of the plasma column. When making intensity ratio measurements, all three XRDs were positioned at one radius, usually the one closest to the experimental axis.

Various entrance aperture geometries were used in the course of the experimental program. The first used was a single 0.070 in diameter hole in the center of the plate. This gave an adequate signal, but did not support the thinnest foils against blast damage from the pinch. Half mil beryllium foils usually cracked after only a few shots with this arrangement. A single 0.035 in hole was also tried, but this did not admit enough x-ray power to produce adequate signals for some experiments. In addition, it was little better than the larger hole in supporting the beryllium foils, since the fracture of the foils seemed to be initiated by sharp bending where it was clamped at the edge of the hole.

The most satisfactory entrance aperture arrangement is the one shown in Figure 7.1a. It consisted of a single 0.150 inch hole centered over the XRD (0.200 inch sensitive area). The foil was supported by sandwiching it between two layers of precision stainless steel mesh. The alignment of the mesh, and consequently a constant entrance area, was assured by using small dowel pins in the parting plane of the foil holder. The mesh that was used

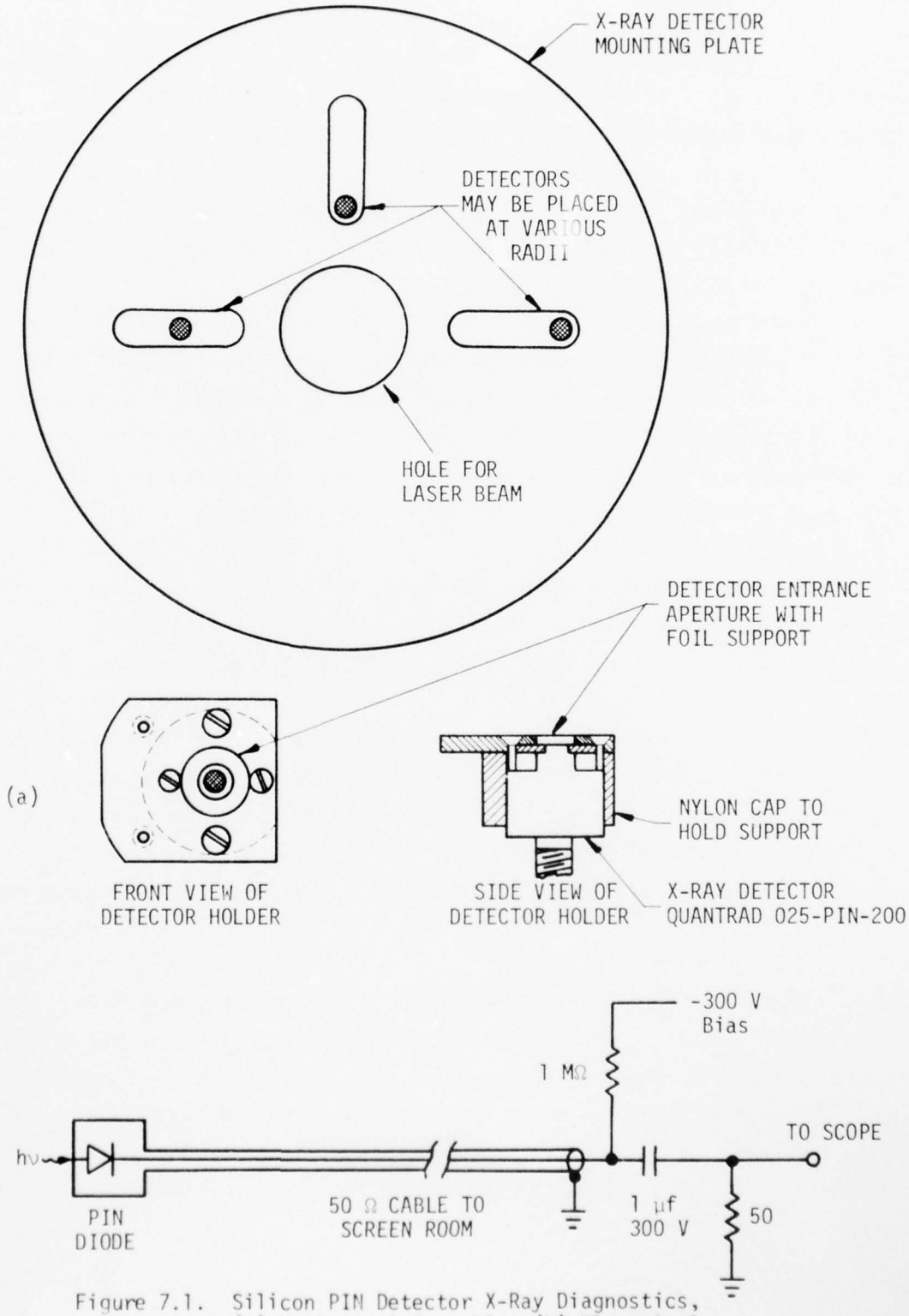


Figure 7.1. Silicon PIN Detector X-Ray Diagnostics, (a) Mechanical Assembly, (b) Electrical Schematic

was a simple grid of 0.020 in., nearly square holes in stainless steel foil sold commercially as a replacement screen for Shick electric razors. The geometrical transmission of this screen was measured optically and found to be 48 percent. At the low x-ray energies that were being measured, this screen, which was about 0.001 in thick, may be considered to be completely opaque. At higher energies, however, a thicker screen of electro-formed mesh would be advisable.

The biasing arrangement for the x-ray detectors is shown in Figure 7.1b. The AC coupling scheme used was found to give quite adequate rise time if attention is given to the choice of a coupling capacitor. An advantage over various "hot case" biasing schemes that might be used is the avoidance of additional noise pick-up in the bias supply.

The voltage output of an XRD is given by

$$V = R_L G A \int_{\text{all } E} R(E)T(E)I(E)dE \qquad (7.1)$$

where R_L is the load resistance, G is the detector sensitivity in A/watt, A is the effective area, R is the response function of the detector, T is the transmission of the foil, and I is the x-ray intensity in watts/cm^2-keV at the XRD location, all functions of the photon energy E. For line radiation, the integral may be replaced by a summation over the prominent lines.

These detectors have a maximum sensitivity of about 0.28 amp/watt at a photon energy of around one keV. The response curve in the region of 0.6 to 1.8 keV is shown in Figure 7.2a, with GR(E) plotted as a function of E. This data is supplied by the manufacturer, and has been found by other investigators[13] to be accurate within ± ten percent from detector to detector. Therefore, they may be used without calibration with reasonable accuracy.

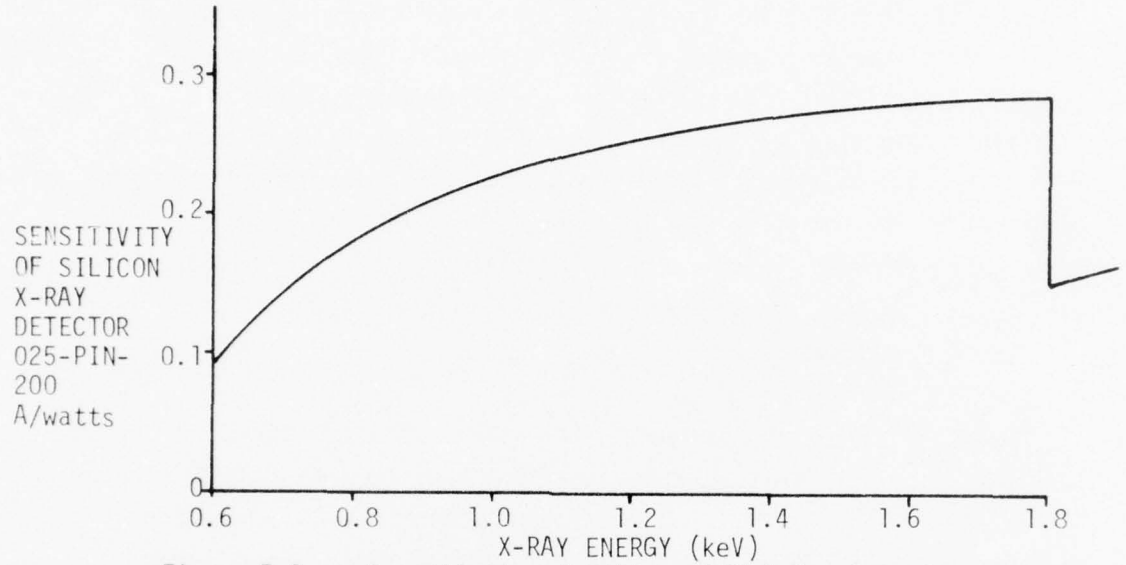


Figure 7.2 a. Sensitivity of Silicon PIN X-Ray Detector

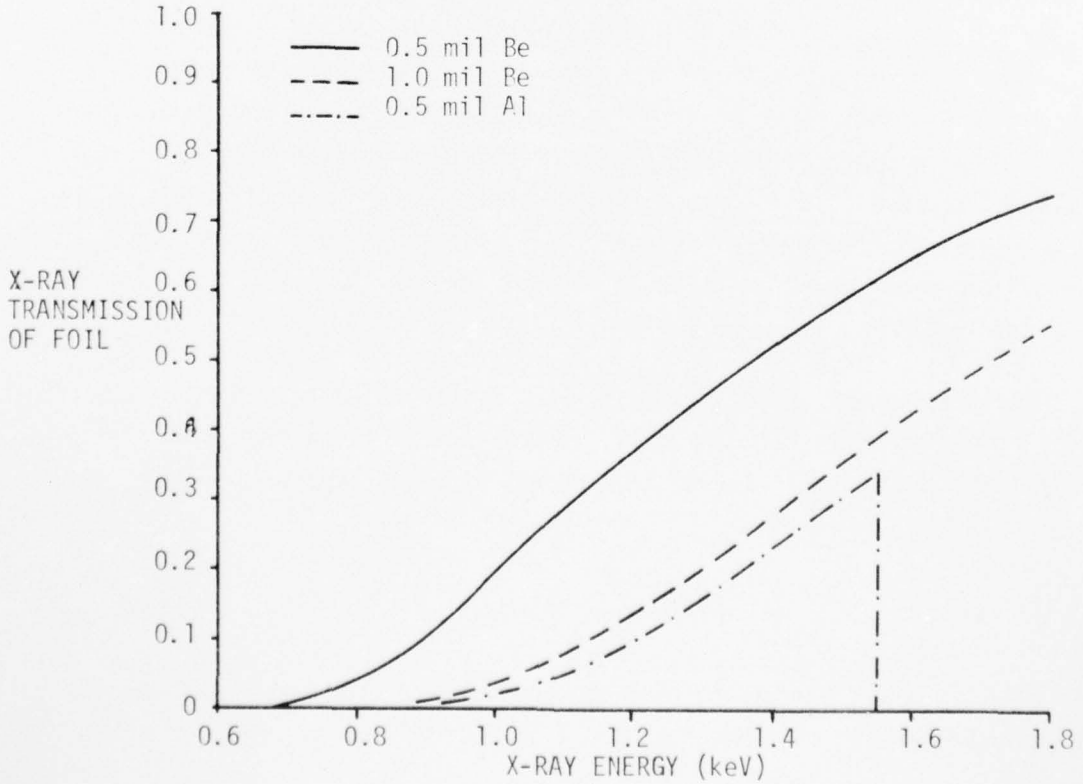


Figure 7.2 b. Transmission of X-Ray Filter Foils

76 00208

The foil transmission T(E) is plotted as a function of energy for the three foils that were used. The mass absorption data used was obtained from Stratton.[14] For a simple line spectrum, the ratio of intensities transmitted through the two beryllium foil filters gives a reasonable indication of photon energy. The absorption coefficient per unit thickness of the aluminum becomes so high below about one keV that a small error in determining the foil thickness may cause a large variation in transmitted intensity. Therefore, the beryllium foil intensity ratio is the preferred measurement.

As a test of the x-ray diagnostics system, line radiation from laser heated metal vapor plasmas, produced by simply placing a solid metal target in the evacuated theta pinch chamber at the focus of the CO_2 laser beam, was looked for. The XRD package in this case was located seven inches from the target surface, as shown in Figure 7.3. With a laser heating input of 80 joules in a pulse of 40 nsec FWHM, x-rays were observed on all three XRDs. Typical records are shown in Figure 7.3. The strongest and most reproducible output was observed using an aluminum target. In this case, the ratio of signals produced by the 1.0 mil Be foil XRD to that of the 0.5 mil Be foil XRD was 0.7. This ratio corresponds to a monochromatic energy of 1.6 keV, which is the He-like resonance line. This energy is above the 1.56 keV aluminum absorption edge, which would account for the low x-ray flux registered by the XRD behind the aluminum foil.

The x-ray power output from a source may be evaluated from the output of one of the XRDs, once the foil transmission is known from a two-foil measurement. The output power of the source, assuming isotropic radiation, is

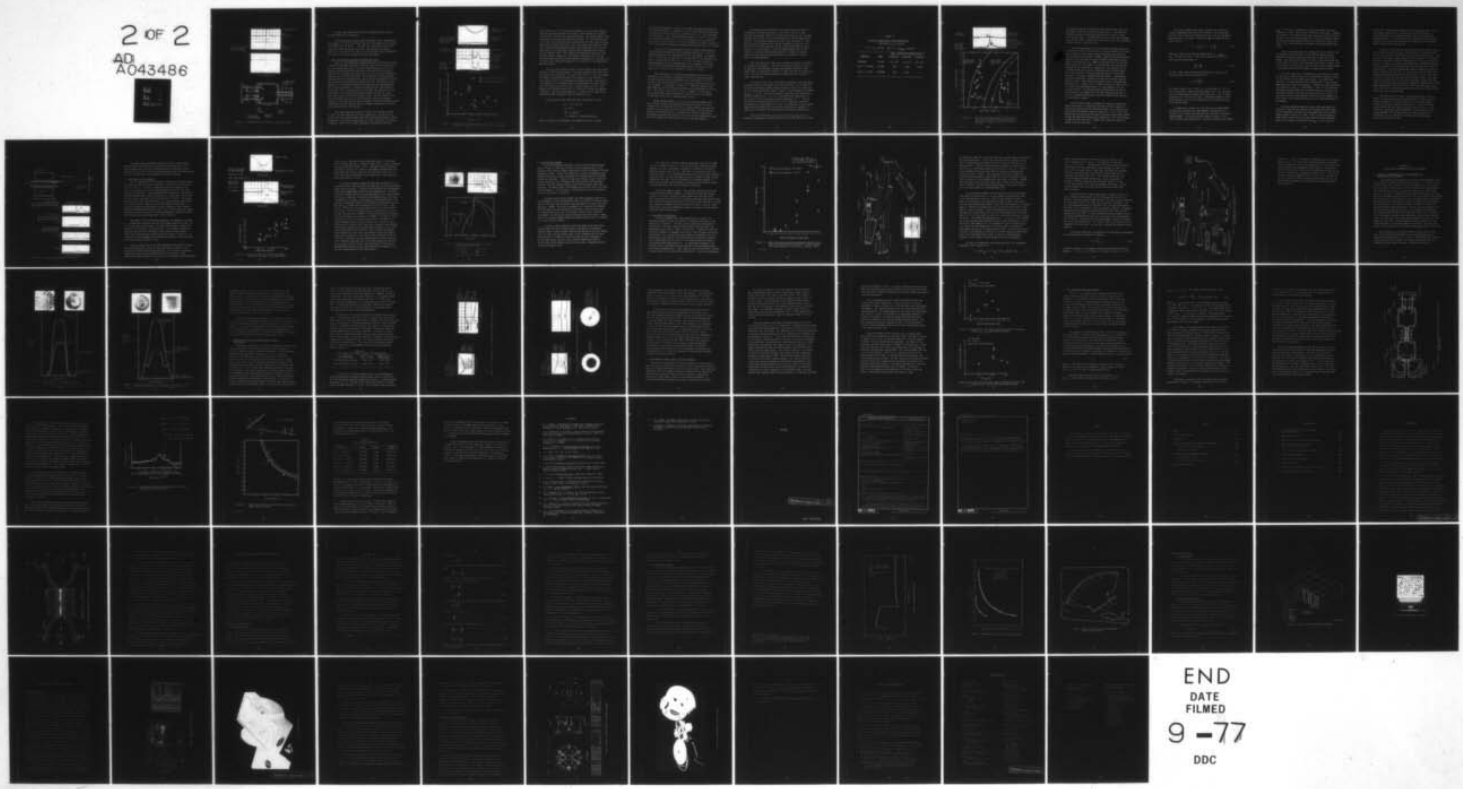
$$W = 4\pi a^2 \Phi \tag{7.2}$$

where Φ is the x-ray flux at the detector, and a is the distance between the source and the XRD. Since the flux $\Phi = \int I(E)dE$, the source power is

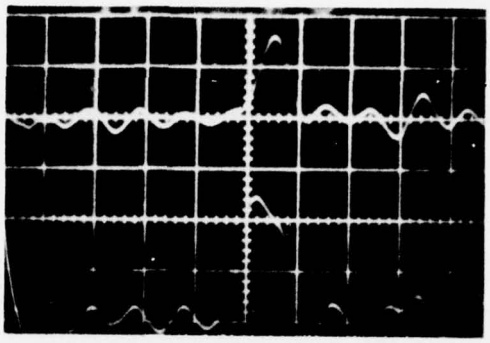
$$W = CV = \frac{4\pi a^2}{R_L G A \bar{R} \bar{T}} V(\text{volts}) \quad \text{watts} \tag{7.3}$$

AD-A043 486 MATHEMATICAL SCIENCES NORTHWEST INC BELLEVUE WASH F/G 20/9
LASER HEATING OF MAGNETICALLY CONFINED PLASMAS FOR X-RAY PRODUC--ETC(U)
APR 76 A L HOFFMAN, E A CRAWFORD DNA001-74-C-0006
UNCLASSIFIED MSNW-76-130-1 DNA-3963F NL

2 OF 2
AD A043486



END
DATE FILMED
9 -77
DDC

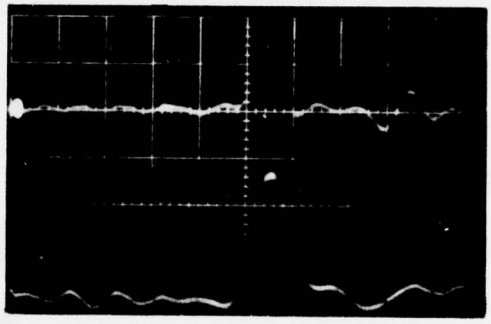


0.070 in diameter
APERTURE

XRD 1 mil Be
5 V/div

TYPICAL X-RAY OUTPUT
IN SOLID ALUMINUM
TARGET EXPERIMENT

XRD 0.5 mil Be
5 V/div



XRD 0.5 mil Al
0.5 V/div

PHOTON DRAG
0.2 V/div

40 nsec/div

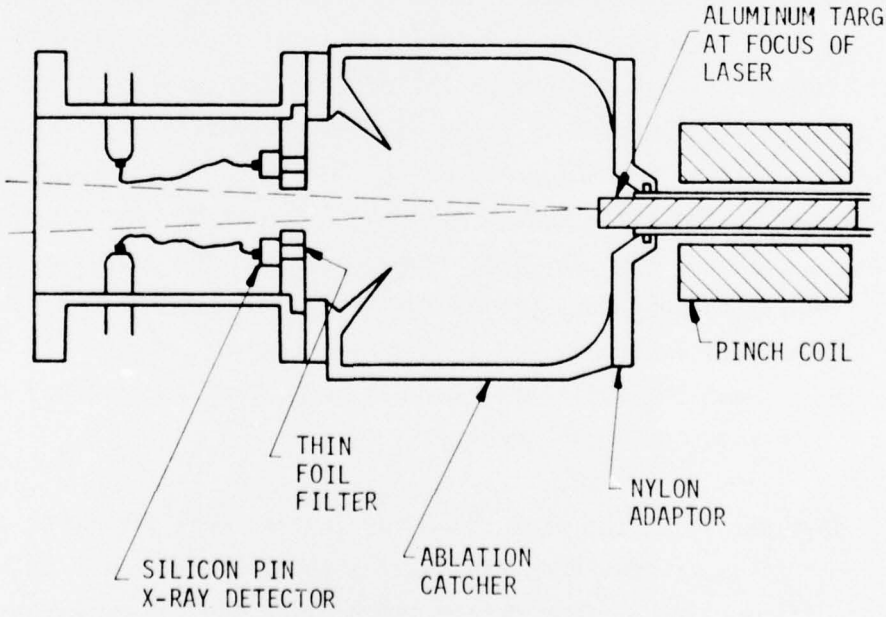


Figure 7.3. Experiment for Laser Heating of Solid Metal Targets

76 00209

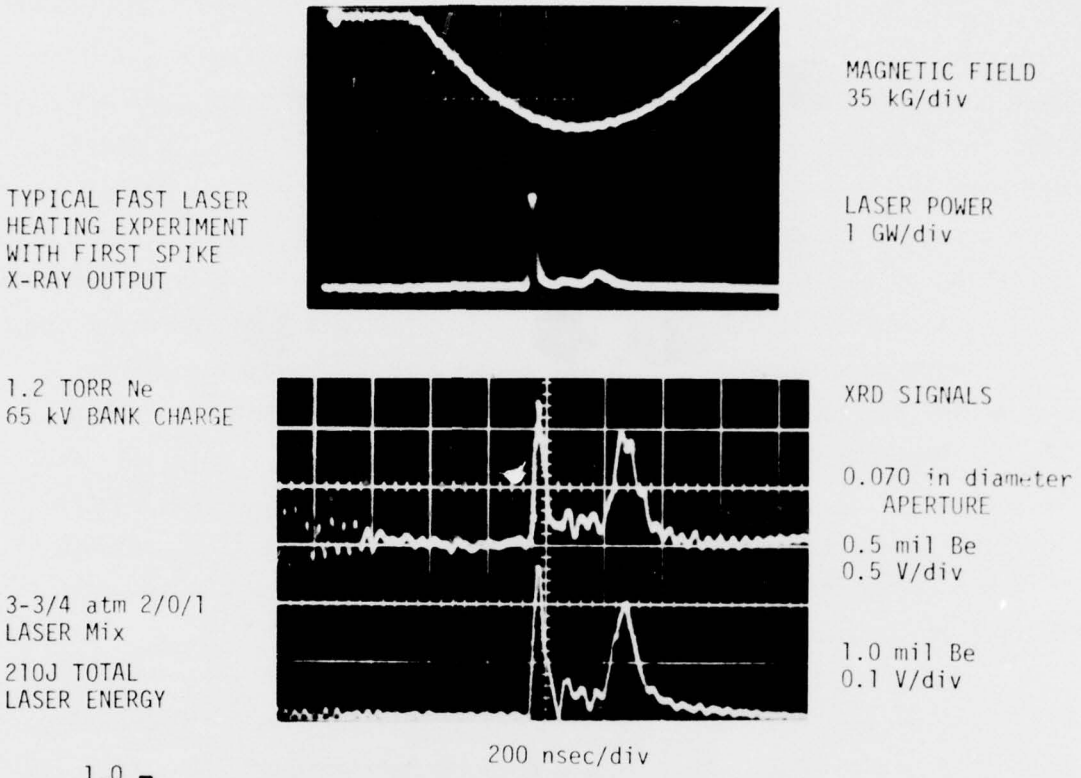
The peak power output from the solid aluminum target was found to be about 100kW into 2π stearadians.

The XRD package was replaced with the SRI bent crystal spectrometer, and sequences of 5 to 10 shots were fired on 1-film exposure, giving a total x-ray energy of 25 to 50 mJ. This was just sufficient to give a film spectrum on Kodak "No Screen" x-ray film. The spectrum was found to consist of 1 line, the Al XII line, at 7.75 Å (1.6 keV), thus corraborating the result of the Be foil transmission ratio measurement.

2. Neon Line Radiation Using Gain Switched Laser Spikes

Using the x-ray diagnostics package described in the previous section, a series of experiments was begun to look for neon IX line radiation from the laser heated theta pinch. Initially, the XRD package was set up to view the laser entrance end of the theta pinch, while the scintillator-photomultiplier package, described in Ref. 1, was set up to simultaneously view the exit end of the theta pinch. No difference in signal was noted (when the 30-40 nsec photomultiplier transit time was subtracted) and, since the large foils covering the scintillators were very susceptible to blast damage, the scintillator-photomultiplier diagnostics were abondoned after the first few experiments. A range of plasma conditions were covered by varying the initial filling pressure in the pinch, the timing of the laser with respect to the pinch bank (including attempts to heat the second half-cycle plasma), and the peak mangetic field. The laser energy in the first gain switch spike was set by the laser gas pressure and pumping voltage. A 2/0/1 laser mix was used originally to maximize the gain switched spike energy, and the sustainer bank was crowbarred immediately after the spike to minimize the "tail" energy.

Best x-ray outputs were found for initial fill pressures of about 1.2 torr. At lower pressures the initial theta pinch density was too low for efficient absorption during the heating and plasma expansion process. At too high a fill pressure (above about 2.0 torr), too high a line density is heated. Figure 7.4 is a plot of the peak x-ray output on the first



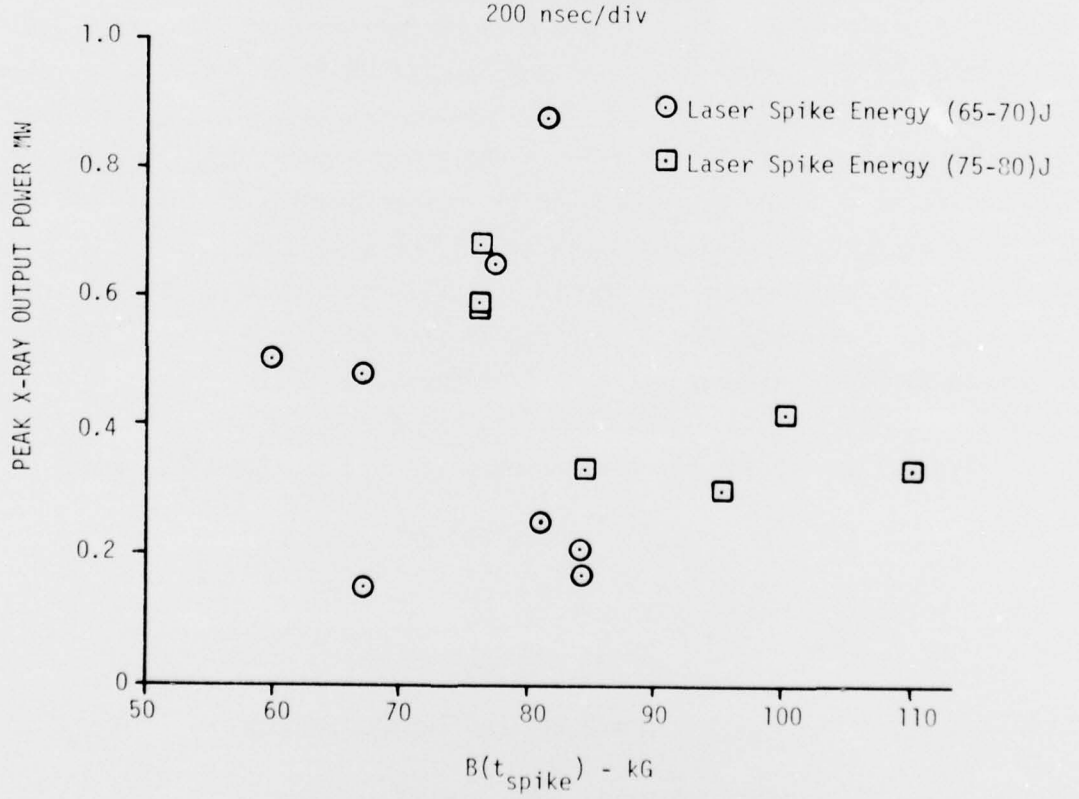


Figure 7.4. Peak K-Shell X-Ray Output Power on First Spike as a Function of Magnetic Field at Time of Laser Spike. P_o = 1.2 torr Neon

laser spike, for a 1.2 torr neon fill pressure, as a function of magnetic field for two ranges of spike laser energy. These results were obtained with both the 7 cm and 10 cm long theta pinches. The plotted magnetic field corresponds to the value when the spike occurred. The oscilloscope traces at the top of the figure are typical records with the laser spike occurring about 100 nsec before peak field. Best x-ray outputs were found for laser spike inputs occurring between 200 nsec earlier than peak field, and the peak field, but no consistent variations were found with exact timing or value of magnetic field. This supports the theoretical conclusions that the peak electron temperatures are limited by radiation and not by the absorption-pressure balance scaling derived in Equations (2.7) through (2.9). Of course, some minimum containment field is required for the temperatures that are reached.

The x-ray traces shown on Figure 7.4 were obtained with XRDs located about 30 cm from the heated plasma. They were fronted by disks with 0.070 in diameter holes covered by .5 mil and 1.0 mil Be foils. The ratio between the signals recorded with the two foil thicknesses is 0.22, and this is fairly typical for all the experiments performed with neon. The value of 0.22 indicates an x-ray photon energy (if monochromatic) of about 1.02 keV. This high energy is surprising since it implies significant $\Delta n = 2$ and higher He-like radiation, when the $\Delta n = 1$, 0.92 keV line would be expected to dominate. The exact energy spectrum is critical in this range for determining the XRD calibration factor C in Equation (5.3).

Typical values for the quantities given in Equation (7.3) are

$$4\pi a^2 = 1.25 \times 10^4 \text{ cm}^2$$

$$R_L = 50\ \Omega$$

$$\bar{GR} = 0.2 \text{ A/watt}$$

$$A = 0.055 \text{ cm}^2 \text{ --(with mesh holder)}$$

Thus C is equal to $0.023/\bar{T}$ MW/volt. One additional factor is needed

to correct for absorption in the 1.2 torr neon background gas between the plasma and the detector. Reference 15 gives a mass absorption coefficient for neon gas of 8240 cm^2/gm to Cu L_α radiation at 13.3 Å. This corresponds to 0.01/torr-cm. Since the neon absorption edge is at 14.2 Å, the He-like neon radiation, beginning at 13.5 Å, will experience similar absorption. With typical fill pressures of 1.2 torr, and detector to plasma spacings of 30 cm, the transmitted radiation through the background neon gas is 70 percent.

Using this 70 percent absorption factor C becomes $0.032/\bar{T}$ MW/volt. The principal uncertainty now lies in choosing the value of $\bar{T}$, since this depends strongly on the x-ray spectrum in the 1 keV region. For example, T for 0.5 mil Be foil is equal to 0.12 for the 922 eV 1s-2p resonance line, and T = 0.26 for the 1075 eV 1s-3p n = 2 line. If these are the only two contributing lines the measured ratio of 0.22 between 1 mil Be and 0.5 mil Be foil transmission implies equal fluxes from both lines and values of $\bar{T}$ = 0.19 for 0.5 mil Be and $\bar{T}$ = 0.042 for 1 mil Be.

The above values of $\bar{T}$ are extremely dependent on the exact foil thicknesses. For example, an intensity ratio of 0.22 would be measured for 922 eV radiation with a difference in foil thicknesses of 0.36 mil instead of the specified 0.50 mil. For this reason, and the fact that the 1s-2p f-number is so dominant, a value of $\bar{T}$ = 0.0144 was chosen for the data reduction, using the measured voltage from the XRD behind the 1 mil Be foil. This gives a value of C(1 mil Be) = 2.2 MW/volt for the screen supported foil-XRD package located 30 cm from the plasma or 4.8 MW/volt for the XRDs with a 0.070 in diameter hole in front.

An XRD detector behind a 0.5 mil Al foil generally produced only one-fifth the voltage as the detector behind the 1.0 mil Be foil, even though Figure 7.2b shows the 0.5 mil Al to transmit between one-third and one-half as much as the 1.0 mil Be in the 1 keV range. As mentioned previously, the aluminum opacity is so high here as to make a quantitative measurement impossible, but the 0.5 mil Al to 1.0 mil Be transmission ratios do tend to support the lower value of $\bar{T}$ used in the data reduction.

One other possible explanation for the measured ratios would be a contribution of higher energy than 1.1 keV x-rays. Table 7.1 shows possible contributions, with foil transmission factored in, for continuum radiation and 0.93 and 1.6 keV line radiation at a 0.16 keV electron temperature. The continuum transmission factors come from Elton.[16] They give roughly the measured ratios, but the transmitted intensities are a factor of 100 less than measured, and the continuum contribution can be ignored for the neon plasmas. Using our alumina plasma tube, 1.6 keV radiation is possible from aluminum impurities. However, an impurity fraction greater than 50 percent would have to be present to have an impact on the measurements.

Neon line radiation is thus seen to be the only possible contributor to the measured XRD signals. The exact calibration constants are based on theoretical considerations assuming pure resonance radiation, even though there is experimental evidence for higher order He-like Lyman series lines. This will be discussed further in conjunction with the spectra shown in Section VIII.

The results of the first spike heating experiments, using the above calibration factors, are plotted as circles on Figure 7.5 as a function of the laser spike energy, without regard to magnetic field. For comparison, the first spike calculations shown in Figure 3.7 are reproduced as the solid $Z_{initial} = 1$ curve. The initial conditions specified in the calculations were an ion density at 3×10^{17} cm^{-3}, electron and ion temperatures of 10 eV, and an initial ionization level corresponding to $Z = 1$. For the specified ion line density of 0.25×10^{17} cm^{-1}, these low β conditions correspond to a column diameter of 3.2 mm. This dimension is just slightly larger than the focused laser spot, and the ion density corresponds to about the 1.2 torr neon fill pressure with a theta pinch compression at 7.

There is considerable scatter in the first spike data, which is primarily influenced by alignment between the laser beam and plasma column.

Table 7.1

Possible Contributions to XRD Signal Behind
Thin Foils at T_e = 0.16 keV

$Z = 8 \quad n_e = 10^{18}/cm^3 \quad R_g f = 1.0 \quad V_{plasma} = 0.25\ cm^3$

Radiation	Power	Power Transmitted Through Foil-MW		
		0.5 mil Be	1.0 mil Be	0.5 mil Al
Continuum	1.6 MW	1.6×10^{-3}	0.4×10^{-3}	0.12×10^{-3}
Line χ = 0.93 keV	3.8 MW	0.45	0.054	0.043
Line χ = 1.6 keV	0.056 MW	0.04	0.027	--

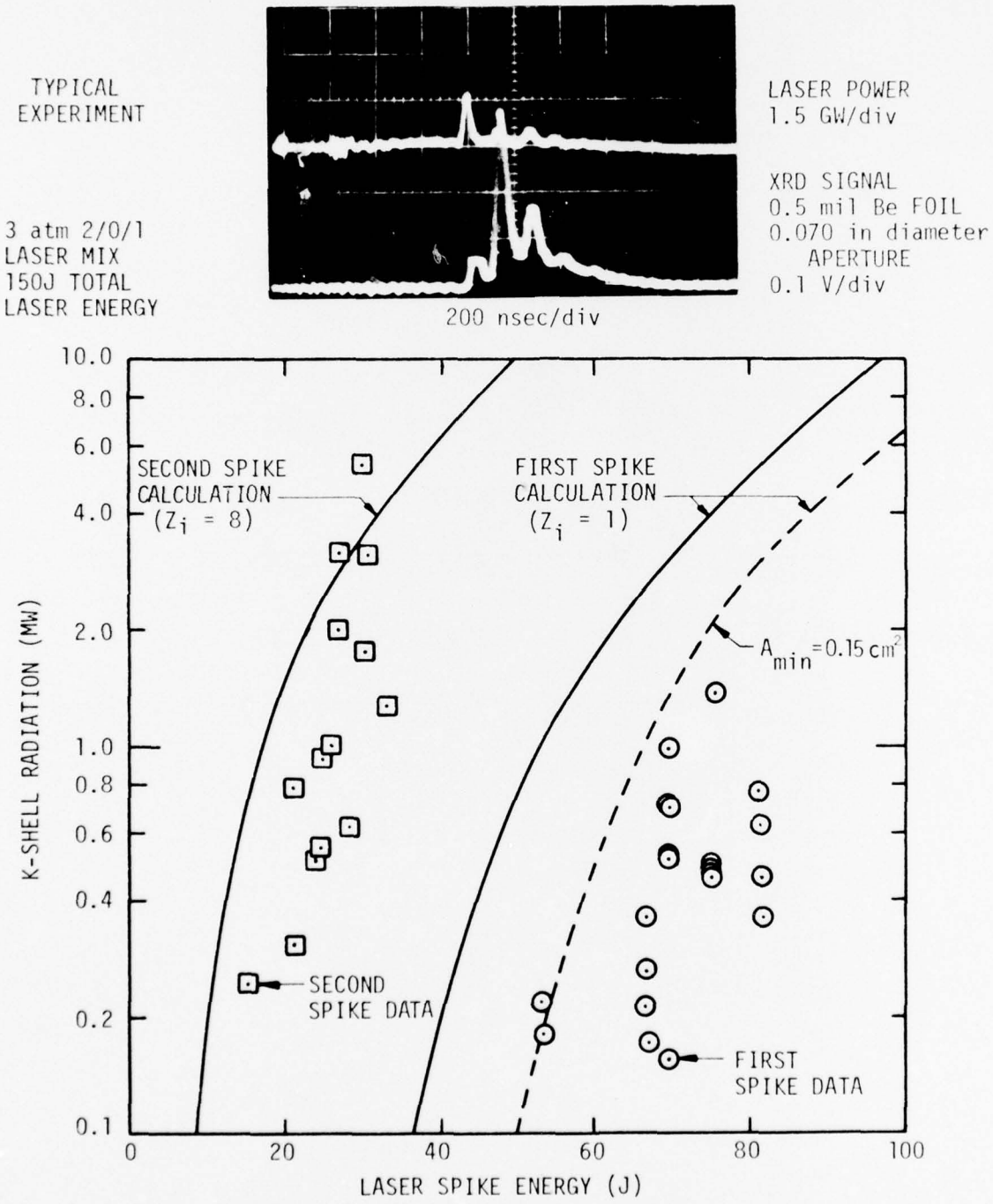


Figure 7.5. Theoretical and Experimental K-Shell Radiation on First and Second Laser Spikes Irradiating Neon Theta Pinch B_{max} = 100 kG, Fill Pressure = 1.2 torr

This precludes making any definative comparisons between theory and experiment, except to say that more laser energy is experimentally required than would be predicted theoretically to reach a K-shell X-ray emitting state. Experimentally, for first spike laser energies less than 50 J there is never any X-ray emission, while the calculated threshold energy is only about 35 J.

Possible explanations for the discrepancies between theory and experiment are slower ionization rates or faster radiation rates than used in HIRAD, or laser beam spreading beyond the area containing the N_p line density specified in HOFNEX. Multistep ionization should make the single step processes used in HIRAD a conservative approximation, and likewise use of a BBMFCT factor equal to 20 in the black body limited rate should make the soft radiation rates conservative. Although the CO_2 laser beam is focused to a 1 to 2 mm spot size on the front of the plasma column, refraction could certainly spread this radiation over a larger area than the initial 3.3 mm column diameter if the density gradients were unfavorable. Inteferograms displayed in Reference 1 show an initially very favorable electron density profile in neon theta pinch plasmas, with a strong density minimum on axis. However, this is known to be due to a lower ionization level, and the neutral density is surely peaked on axis for pressure balance. (The electron density minimum lasts too long to be accounted for by trapped field and lower plasma beta on axis.) The fast solenoid inteferograms in the next chapter do not have this electron density minimum.

For the initial phases of heating of a neutral, or relatively weakly ionized gas, by a Gaussian laser beam, a density peak will form on axis due to more rapid ionization there. For a typical 50 eV plasma with a 0.04 mm/nsec acoustic speed (for $Z = 3$, $A_i = 20$), this density peak can persist on the order of 25 nsec before acoustic motion changes the peaked distribution to an annular one. This first 25 nsec is when the laser intensity is highest, and significant refractive energy losses can take place.

The initial incoming laser beam is focused with f/15 optics giving a convergence half angle of 0.03 radians. This angle alone does not result in excessive divergence for the first few centimeters beyond the laser focal point. The plasma index of retraction, however, varies as

$$\Delta n = (1 - n_e/n_{e_c})^{1/2} \approx 1 - \frac{1}{2}\frac{n_e}{n_{e_c}} \tag{7.4}$$

where n_{e_c} is the critical electron density where $\omega_p = \omega_{laser}$ ($n_{e_c} = 10^{19}/cm^3$ for 10.6 μ). The Eikonal equation for refraction can be written approximately as

$$\frac{d^2r}{ds^2} = \frac{dn}{dr} \tag{7.5}$$

and for a linear index of refraction variation $\Delta n = (\Delta n_o/\Delta r_o)r$ an initially parallel ray will move off axis

$$\Delta r = \frac{1}{2}\left(\frac{\Delta n_o}{\Delta r_o}\right) s^2 \tag{7.6}$$

For typical values of $\Delta n_o = 0.05$, $\Delta r_o = 0.25$ cm, then $\Delta r = 0.1\ s^2$, or Δr can change by 1 mm after the ray travels only 1 cm. Since the initial plasma absorption length varies from 1.0 to 1.5 cm (as shown by Figure 3.5) in the first 25 nsec, a considerable amount of first spike radiation can be lost to refraction out of the dense portion of the plasma column.

As mentioned in Section III, this effect can be approximated by specifying a minimum laser beam diameter, and neglecting any portion of the incident radiation which falls outside of the plasma column diameter. For the calculations shown in Figure 7.5, the initial plasma column diameter was 3.3 mm and the dashed curve labeled

A_{min} = 0.15 cm^2 was calculated for a specified minimum laser beam diameter of 4.4 mm. Thus the initial effective laser power is reduced by a factor of 0.56 from the solid curve calculation and the threshold energy is seen to increase by about 15 J. Even this additional energy loss may be an underestimate of the initial refractive effects, but there is seen to be much better agreement with the experimental data points.

Typical laser power and X-ray radiation traces are shown in the oscilloscope traces on Figure 7.5 for conditions where parametric backscatter from the plasma causes the laser to mode lock to the plasma. The spiking in the Figure 7.5 traces is more pronounced than in the Figure 7.4 traces, even though the laser energy is lower. This is not generally the case, but is an indication of the threshold nature of the backscatter and slight changes in laser-plasma alignment.

The X-ray intensities, corresponding to the second laser spike on runs such as shown in Figure 7.5, are plotted as squares on Figure 7.5 as a function of the second spike energy. The calculations, labeled Z_i = 8, were made for initial conditions of a 50 eV electron temperature and 8 times ionized plasma. Otherwise all other conditions were identical to the Z_i = 1 calculations. Thus, the soft radiation-ionization threshold behavior is eliminated and the calculated curve corresponds roughly to the ideal scaling laws derived in Section II. End-losses and radial heat transfer modify the results somewhat, but these effects are continuous and do not act as a threshold energy to be overcome.

The good agreement between the second spike experiments and predictions indicates that both the laser-plasma absorption process is well understood, and that the plasma heated by the first spike is indeed ionized to the He-like state. There is some discrepancy at lower energies most likely due to the refractive losses mentioned above but not enough to justify the same A_{min} = 0.15 cm^2 type of

calculation. The difference between the first and second spike x-ray power, when compared to the first and second spike laser power, is vivid confirmation of the threshold effect caused by the ionization-radiation process. The second spike results also show that the plasma heated by the first spike is contained well enough to still be present when the second laser spike arrives.

In order to investigate more thoroughly the plasma end-loss process, the experiment sketched in Figure 7.6 was performed. Three XRDs, each with a 1.0 mil Be foil filter, were set up at three different radii. Care was taken to maintain azimuthal symmetry of the apparatus. The detector mount was on the end of the pinch tube opposite to the CO_2 laser beam entrance. As shown by the figure, each detector was vignetted by the edge of the pinch tube, so that each detector "saw" only part of the pinch plasma on-axis. The three separate XRD signals reproduced in Figure 7.6 were all taken on the same shot. It can be easily seen that XRD1, which viewed all the plasma column within the pinch coil, saw an x-ray signal on the first laser spike, and also on the two later pulses. XRD2, which viewed all but the first 1.2 cm of the pinch column, saw only the late pulse, and then with reduced amplitude, suggesting a reduced source volume. XRD3, which viewed all but the first 4.2 cm of the pinch column, saw no x-ray signal at all, indicating that the hot region never reached farther than 4.2 cm into the pinch column.

These results tend to confirm the area wave assumption used in HOFNEX. A comparison with the calculation shown in Figure 3.8 shows the 80 nsec radiation to come from the first 1.5 cm of the plasma column, the 280 nsec radiation to come from $1\frac{1}{2}$ to $2\frac{1}{2}$ cm into the column, and the 480 nsec radiation to come from $2\frac{1}{2}$ to $3\frac{1}{2}$ cm. The excellent correspondence with the AREDFCT = 0.5 calculation is also in good agreement with standard theta pinch end-loss theory and experiments, but is a more definite indication of the area wave processes than previously seen.

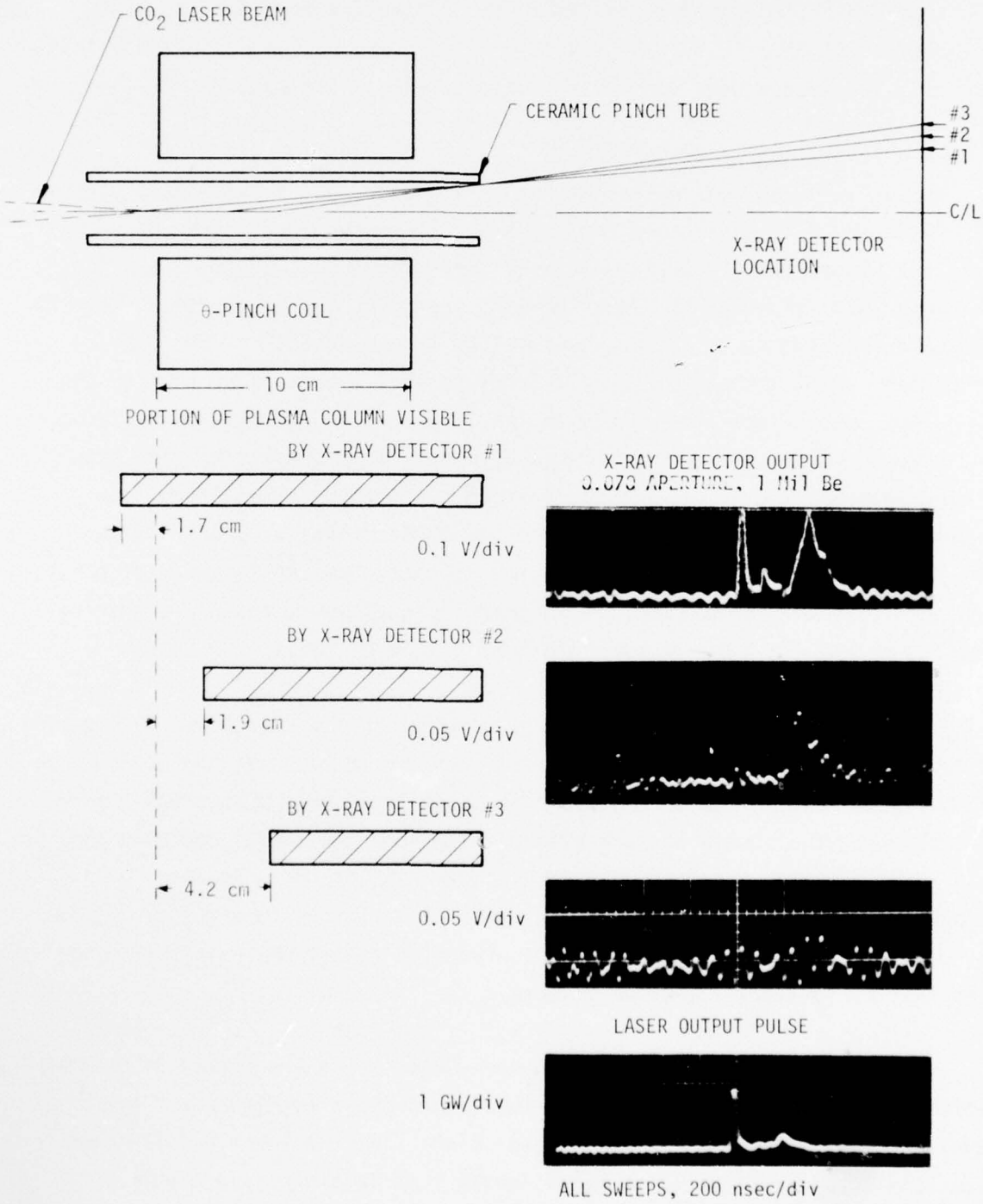


Figure 7.6. Experiment Showing Propagation of Hot Region

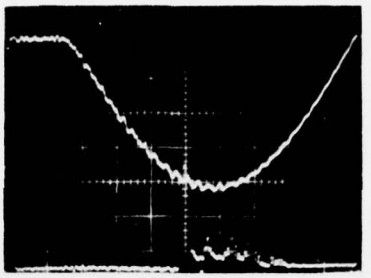
The longer plasma containment times than given by simple acoustic end-flow allows laser heating to be performed over a longer time scale. The experiments described in the following subsection were done to take advantage of this effect, plus the threshold nature of the radiation emission process, to produce more copious amounts of K-shell radiation.

3. Long Time Scale Laser Heating

The laser output results in Figure 6.3 show that quasi-steady powers of 500 MW could be maintained for durations in excess of 0.5 μsec by using a 3/½/1 laser mix. A series of experiments was thus conducted using this mix and sustaining the laser pumping power for up to 0.6 μsec after the gain switched spike. These experiments were conducted at the previously determined optimum theta pinch fill pressure of 1.2 torr neon, and for the most part near a peak pinch field in the 7 cm coil of 100 kG. The spiking behavior shown on the right of Figure 6.3 was always present to some extent if accurate alignment between the laser and plasma was maintained. In fact, the presence of spiking was an accurate indicator of good alignment. The depth of modulation varied from shot to shot, but the total laser energy remained constant for a given set of pumping conditions, and hence spiking did not change the average power level in the laser tail.

The results of the slow heating experiments are summarized in Figure 7.7. The XRDs were located at the end of the plasma nearest the laser, and thus saw the entire heated region. The total laser energy is roughly proportional to the energy in each after spike. For the lowest energies the radiation took the form of individual spikes similar to those shown in Figure 7.5, and some of these results were also plotted in Figure 7.5. As noted earlier, the agreement with the predicted radiation is very good when the initial ionization process is over.

The exact form at the x-ray output depended on the degree of spiking, which varied from shot to shot, but the traces shown on Figure 7.7 are typical of the higher laser energy conditions. At the lower oscilloscope sensitivities any first spike radiation is lost in the noise. Some modulation in phase with the laser spiking is still present, but the radiation



PINCH 1 V/div

PHOTON DRAG 0.2 V/div

TYPICAL SLOW LASER HEATING EXPERIMENT

LASER 3/0.5/1 MIX

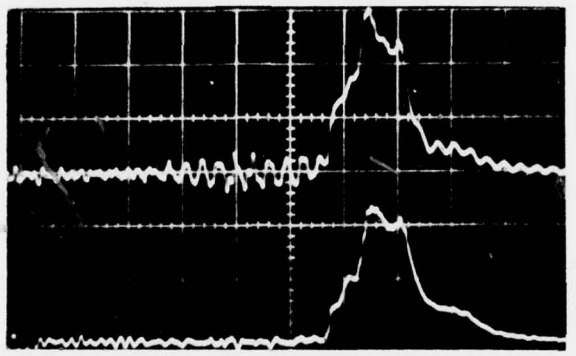
200 nsec/DIV

FIRST SPIKE ENERGY 65 J

TOTAL LASER ENERGY 330 J

B_o = 100 kG

1.2 TORR Ne



APERTURE 0.150 in WITH SCREEN

XRD 0.5 mil Be
2 V/div

XRD 1.0 mil Be
0.5 V/div
$I_{1.0}/I_{0.5}$ = 0.20

200 nsec/DIV

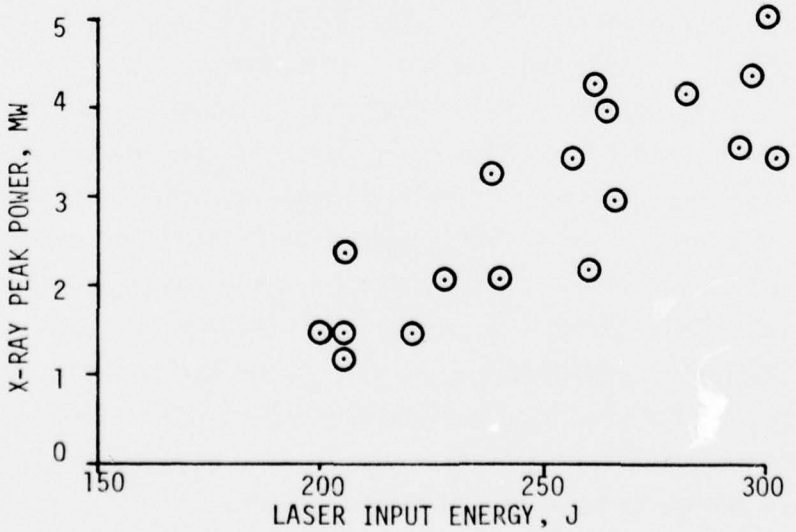


Figure 7.7. Results of Slow Laser Heating Experiment; 3/0.5/1 Mix in Laser; 1.2 torr Ne in Pinch.

level is more a function of the average power level. An additional set of detector waveforms is shown on Figure 7.8 for a laser irradiation with less pronounced spiking. This is compared with the theoretical calculation of Figure 3.9. There is good general agreement with the pulse shape and intensity after the first two laser spikes, but no first spike energy is detected and the second spike x-ray power must begin from a near zero level.

The large discrepancy between the experiment and numerical calculations at early times are almost certainly due to the beam refraction losses discussed earlier. A realistic calculation of the interdependent plasma radial hydrodynamics and laser beam propagation is far beyond the scope of HOFNEX, and can only be approximated in the crudest fashion by the A_{min} stipulation. Calculations performed with A_{min} low enough to reduce the first spike x-ray emission to undetectable values, also resulted in subsequent radiation levels below the measured value, even when the A_{min} stipulation was dropped after the first spike. Thus, the tail of the laser spike must either remain more tightly focused than the $N_p = 0.025\ cm^{-1}$ column diameter, or the plasma losses must be lower than specified in HOFNEX. As mentioned previously, resonance losses are allowed to be high due to the BBMFCT = 20 numerical input, and radial losses are also high since no provision is made for a thermal boundary layer outside the central core. (Early time beam refraction will certainly help create such a boundary layer, although it may not be effective due to rapid radiative losses.) Less rapid cooling than theoretically predicted seems to support the reduced losses explanation. Most likely both tighter focusing and reduced plasma losses contribute to the strong K-shell radiation during the laser tail. Considering all the unknown behavior, the calculations give a remarkably good modeling of the plasma temperature, and serve to verify the classical and well understood nature of the inverse Bremsstrahlung absorption process and heating wave propagation, plus the gross energy balance of the atomic physics.

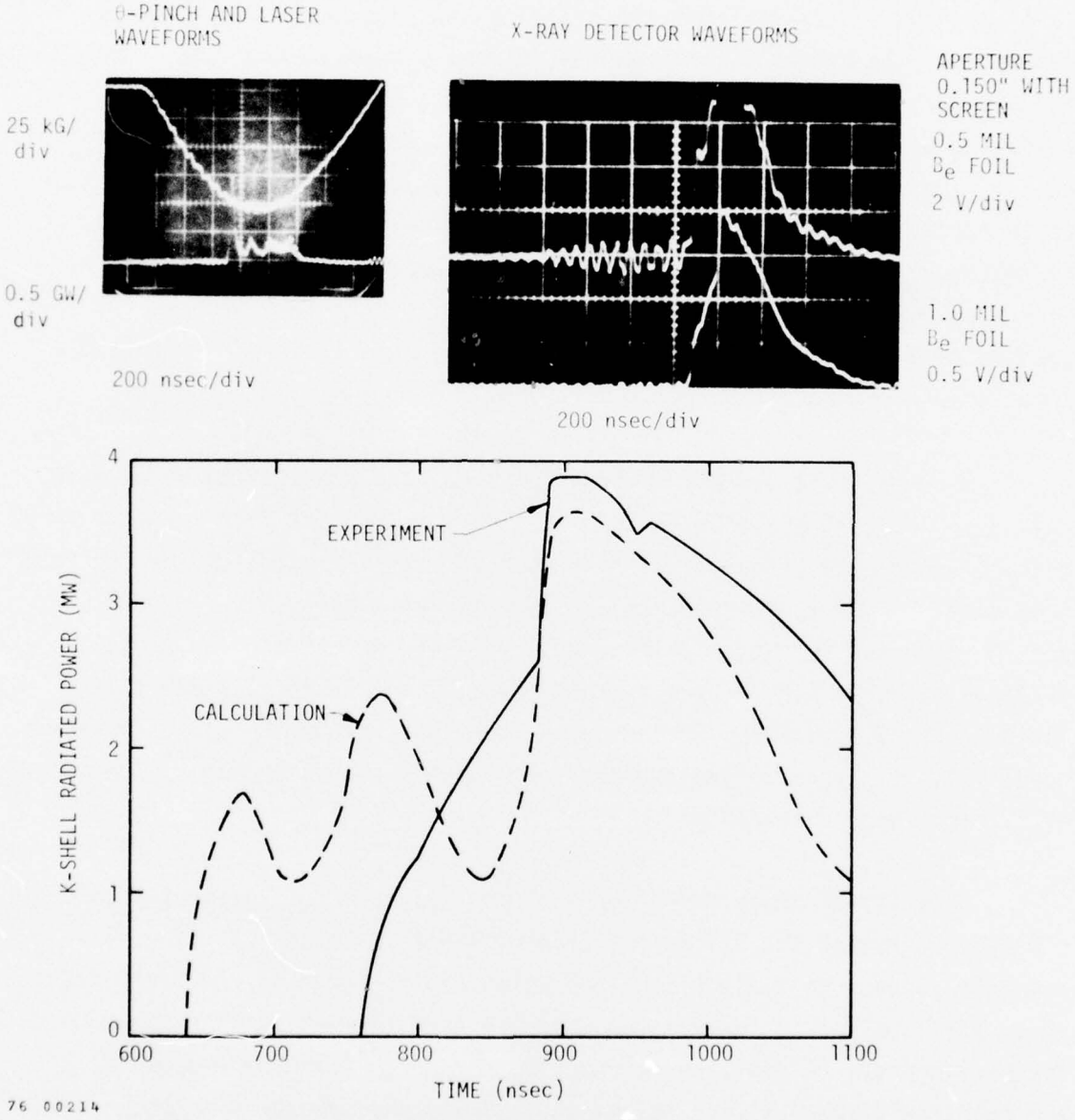


Figure 7.8. Comparison of Theory and Experiment for Laser Heated Neon Theta Pinch Plasma

B_{max} = 100 kG E_{LASER} = 170 J

$t_{1/4}$ = 800 nsec AREDFCT = 0.5

$N_p = 0.025 \times 10^{18}\ cm^{-1}$ BBMFCT = 20

4. Low Z Dilution Effects

The scaling arguments presented in Section II and displayed graphically on Figure 2.2 show that the ratio of soft radiation rate to laser absorption rate cannot be reduced significantly unless the degree of dilution becomes very large. To test this hypothesis, a series of experiments were conducted using a gas mixture consisting of 25 percent neon and 75 percent helium (ion fractions). Figure 2.2 shows this mixture to have a radiation to absorption ratio only 15 percent lower than pure neon, while having a radiation rate (per constant number of particles) 55 percent lower than pure neon. The latter figure is due primarily to the fact that in the final ionized states ($Z = 2$ for He and $Z = 8$ for Ne) only 1 out of 18 instead of 1 out of 9 particles is a neon ion.

Assuming that the plasma dynamics and laser propagation were to remain unchanged, it would be desirable to have an initial fill pressure double that for pure neon, thus providing a neon ion density half that of the pure neon case. However, the theta pinch dynamics will certainly be different, and the compression ratio achieved will be lower as the filling pressure is increased (the type of gas in this phase is not critical since only low degrees of ionization are produced from the theta pinch alone). Therefore, fill pressures somewhat higher than double the pure neon fill pressure of 1.2 torr should be optimal.

A series of image converter pictures was taken of the theta pinch plasma formed with the 3/1 He/Ne gas mix to determine the operational pressure range. Reliable plasma formation was obtained on the first quarter cycle for total pressures greater than 1.0 torr (compared with 0.43 torr for pure neon). In addition, a check was made for laser breakdown in the cold gas without firing the pinch, using a photodiode to monitor visible light at the entrance area to the pinch tube. Breakdown occurred for pressures above 3 torr.

The results of a series of heating experiments using the 3/1 He/Ne fill gas is shown in Figure 7.9. With the laser input energy held nearly constant, the peak x-ray output is plotted as a function of the partial pressure of neon in the fill gas. (The total fill pressure is just four times this value.) The x-ray waveforms were quite similar to those obtained using pure neon. The only difference seen was an absence of "mode locking" behavior of the laser. Thus, the threshold for inducing parametric instabilities must have been increased, or the laser focal intensity reduced by refractive effects (or lack of strong self-focusing).

The results shown in Figure 7.9 are entirely consistent with those expected from the scaling arguments. At neon partial pressures between 0.6 and 1.2 torr the x-ray flux is about one-half the pure neon value. This indicates that similar values of electron temperature have been achieved. These results show that dilution with a low Z gas is not effective in raising the x-radiation, although for very large dilution ratios it may be a good technique for making high temperature plasmas to be used as a spectroscopic source of highly ionized species.

5. Backscatter Investigation

It might be thought that laser backscatter was a serious loss mechanism although this was not manifest by increased laser power in the plasma-laser "resonator". In order to get a quantitative measurement of the fraction of CO_2 laser radiation backscattered from the plasma, the experimental setup shown in Figure 7.10 was used. In addition to the standard laser diagnostic arrangement consisting of the calorimeter and photon drag detector "A", a second backscatter diagnostic arrangement was set up. Approximately eight percent of the backscattered radiation was reflected from a polyethylene pellicle into a 1 m FL concave mirror and focussed onto another photon drag detector "B". An approximate alignment of the pellicle, mirror, and photon drag was made using the autocollimated beam of the He-Ne alignment laser. Then, a heating shot was fired with a polaroid film burn target at the location of photon drag "B". Sufficient backscatter

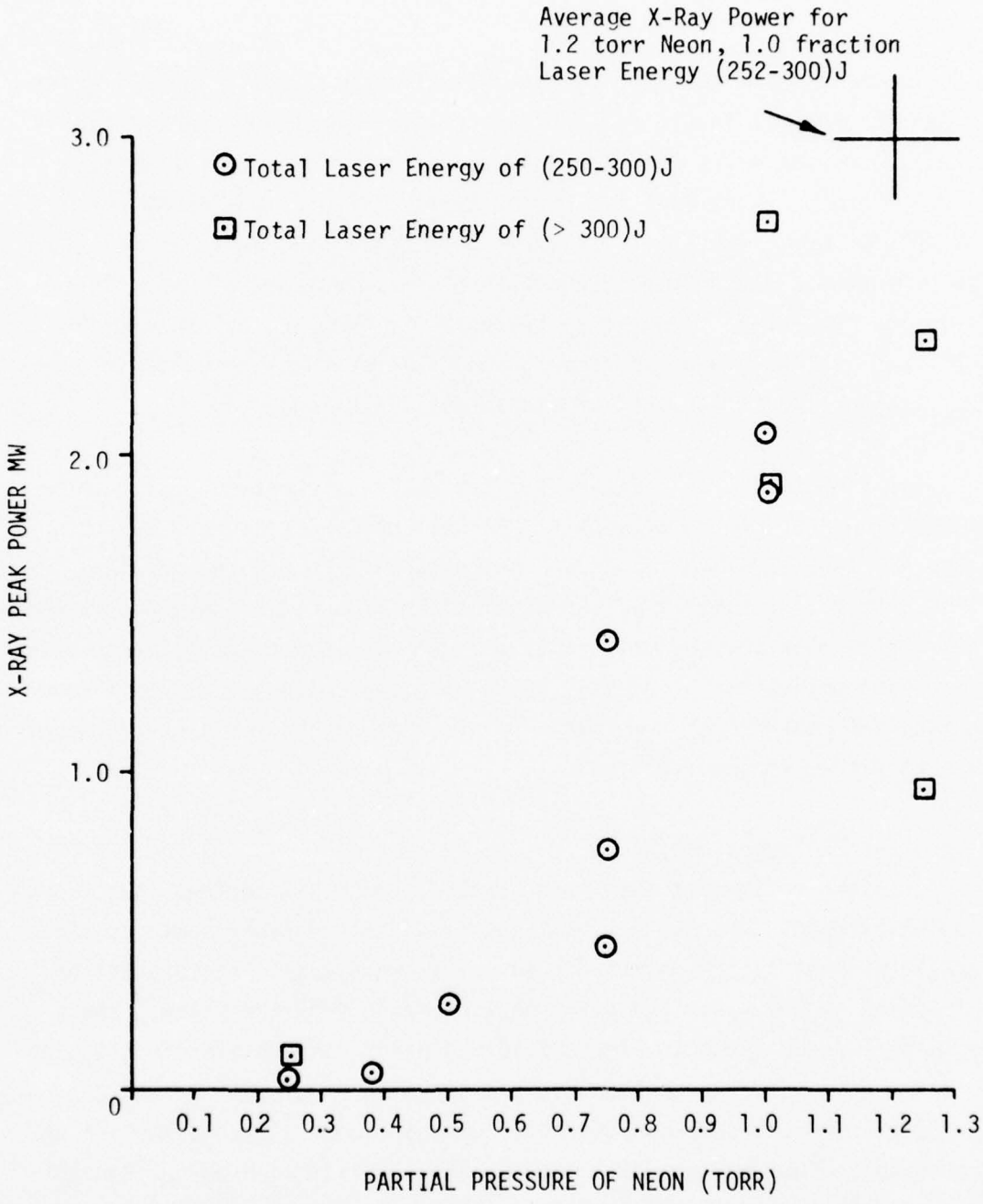


Figure 7.9. Result of Slow Laser Heating Experiment on Helium Diluted Neon 0.25 Fraction Neon at Various Fill Pressures; Laser First Spike Energy 65 J, 3/0.5/1 Mix, Pinch B_o = 100 kG

76 00215

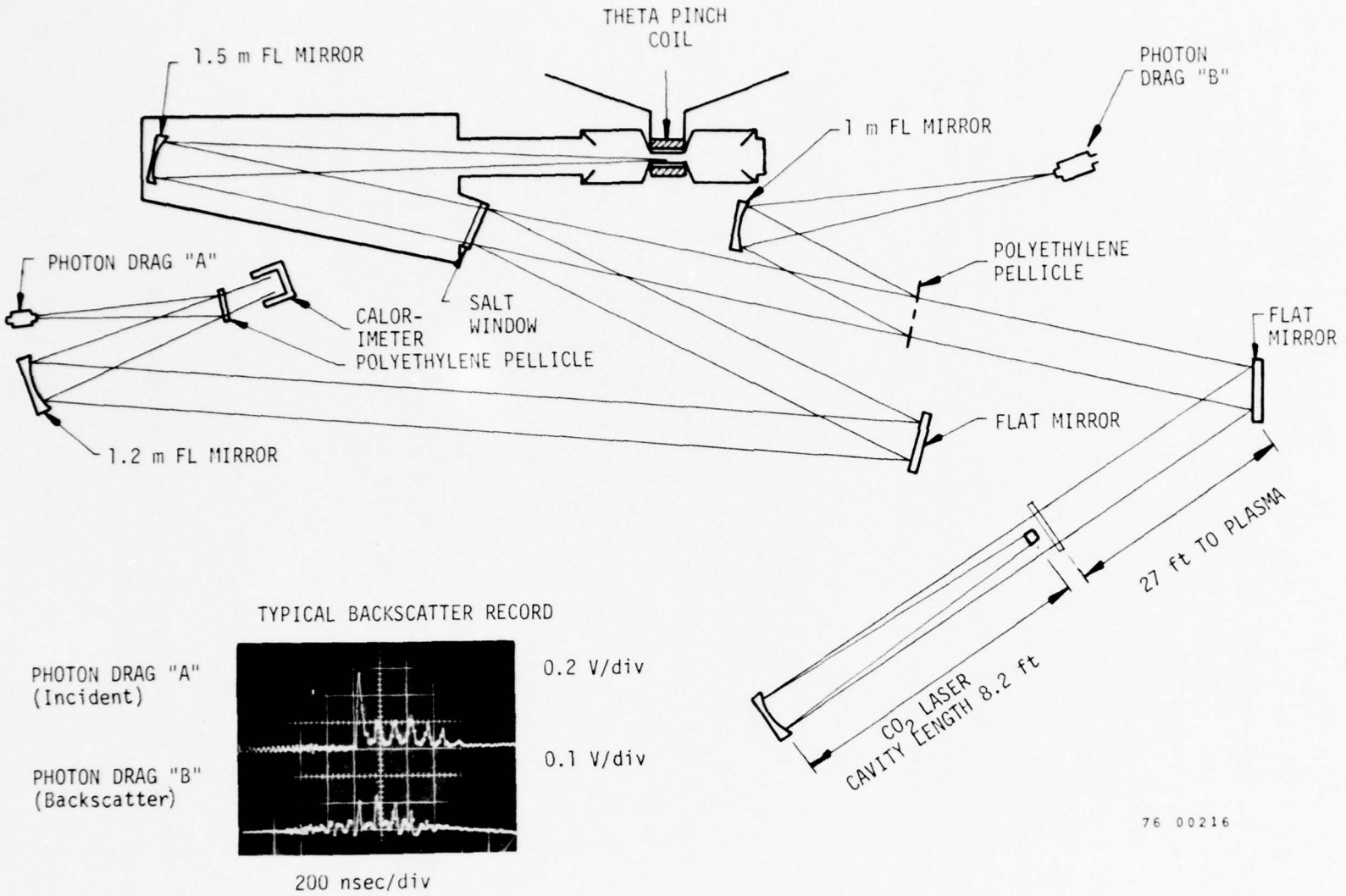


Figure 7.10. Experimental Setup for Time Resolved Backscatter Diagnostics

was obtained to burn the film at the focal spot, and the photon drag detector could be located there. A small focal spot was formed, allowing at least half of the backscattered radiation to fall in the 4 mm^2 entrance area of photon drag "B". Since the input laser beam undergoes one additional reflection off a salt window (assumed to be 5 percent), the 4 to 1 intensity ratio recorded by the photon drag detectors indicates a backscattered fraction at about 1 percent. This value agrees with the estimates obtained from burn patterns at photon drag "B", and with the amount of backscatter necessary to cause modulation of the primary laser beam. Although some subsequent spikes have about three times as great fractional backscatter intensity, the total backscattered energy is less than 1 percent due to the small width of the backscattered spikes.

The time interval between arrival of the laser pulse at the photon drag detector and the arrival of the next reamplified backscatter pulse at the same detector is 135 nsec. Half this time interval in nsec is equal to the distance in feet between the plasma and laser, plus the distance the backscattered beam travels in the laser cavity before it is focused down to a diffraction governed spot size on the small convex mirror, from whence it begins to expand. Since the Cassegranian optics of the unstable resonator has a magnification of 2.58, the 10 cm diameter beam is focused down to 3.87, 1.50, and 0.58 cm diameters on successive double passes through the optics. The diffraction governed radii $\sqrt{\lambda \ell} \approx 0.5$ cm, so that 3 double passes will be made before diffraction effects cause the beam to re-expand. These 49 ft, when added to the 27 ft between the laser and plasma result in a round trip time between pulses of 139 nsec, which is within the experimental accuracy of the measured transit time. The 6 effective passes through the laser medium are sufficient to achieve saturation intensities, even for very weak backscatter inputs, as long as the backscattered radiation is not frequency shifted beyond the laser gain bandwidth.

The CO_2 laser bandwidth at room temperature has a full homogeneous bandwidth at half intensity of[17]

$$\Delta\nu = 5.76(\psi_{CO_2} + 0.73\ \psi_{N_2} + 0.64\ \psi_{He})P(atm)\quad GH_Z \qquad (7.7)$$

where ψ are the molecular fractions of the laser gas mix. For a $3/\frac{1}{2}/1$ $He/N_2/CO_2$ mix at 3 atm, $\Delta\nu$ = 12.6 GH_Z and, for the 10.6 μ line, $\Delta\lambda = 4.7 \times 10^{-3}\mu$. The wavelength of the backscattered radiation was measured using the experimental layout sketched on Figure 7.11. The 1.2 m focal length Czerny - Turner type spectrometer was borrowed from Vlases and Massey and is described in a paper by Massey on parametric backscatter (Ref. 18). A 100 line/mm grating was used in an approximate Littrow configuration, giving a dispersion of 58 Å/mm. Sufficient intensity was transmitted through a 0.25 mm slit to burn Polaroid film at the spectrometer focal plane. Liquid crystal displays were also used, but the film burn patterns gave best resolution.

A small reflector in the incident beam, as shown in Figure 7.11, gave a reference spectrum which could be displaced vertically to distinguish it from the backscattered spectrum, yet provide a good calibration. The He-Ne 6328 Å line in 17th order was also used as a reference. The CO_2 laser operated primarily on the P(20) line, with some contributions from P(22), P(18), and P(16) in order of decreasing intensity. Detectable backscatter was only observed from the P(20) and P(22) lines, but most commonly only from P(20). A typical backscatter spectrum shown in Figure 7.11 shows the backscattered line shift to be quite small; approximately 20 Å to the red. The resolution of the spectrometer is about ±10 Å due to the size of the entrance slit. This shift is seen to fall within the 47 Å bandwidth of the laser gain line, and thus it permits the observed spiking behavior.

If Brillouin scattering is assumed to be the backscattering mechanism, the scattered radiation should be shifted by

$$\Delta\lambda = 2 \frac{V_s}{c} \lambda_o \qquad (7.8)$$

to the red, where V_s is the acoustic speed given by Equation (3.1) with AREDFCT = 1. For $T_e = T_i$ = 0.16 keV, Z = 8, and A = 20, $V_s = 10.7 \times 10^6$

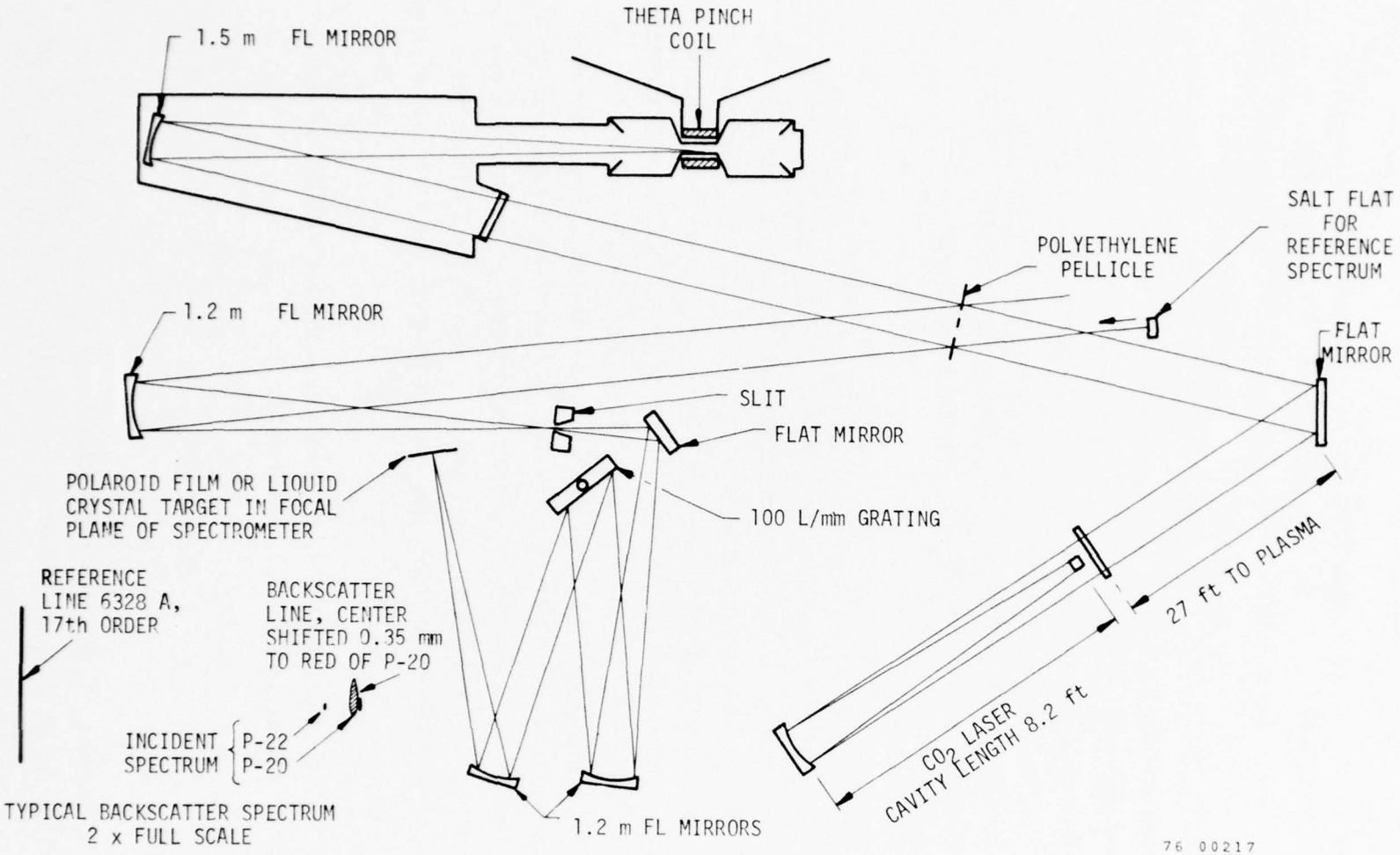


Figure 7.11. Experimental Set-Up for Spectral Resolution of Backscattered CO_2 Laser Radiation.

cm/sec and $\Delta\lambda$ = 76 Å. This amount of wavelength shift was observed by Massey, et al.[18] in similar slow solenoid experiments in hydrogen. Possible explanations for the low observed shift in neon theta pinch plasmas include a low temperature and low degree of ionization in the scattering region at the front of the heating wave where the ion density is highest, or a compensating Doppler shift to the blue due to plasma streaming towards the laser. In any case, the effect of the small shift is to keep the backscattered radiation within the CO_2 P(20) gain bandwidth, and to thus produce the aforementioned spiking behavior.

SECTION VIII
LASER HEATING EXPERIMENTS IN THE FAST SOLENOID

1. Holographic Interferometry of Laser Heated Neon and Krypton in the Fast Solenoid

Interferometric measurements of the initial plasma produced in the fast solenoid has already been discussed in Section V. As one can see from Figure 5.4, the density minimum on axis has disappeared at times greater than about 700 nsec after the start of the solenoid. This caused concern about the ability to couple laser radiation into the end of the plasma column, so additional interferograms were taken after the onset of laser heating to see whether radially symmetric heating was achieved. The technique used was the same as that reported in Section V except that the holographic ruby laser was timed to produce a 20 nsec Q-switched spike after heating with the CO_2 laser. The results are shown in Figures 8.1 and 8.2 for neon and krypton plasmas, respectively. The CO_2 laser was operated in the same "slow heating" mode discussed in 7.3, and produced a 40 nsec-65 J gain switched spike followed by a 500 MW tail of up to 0.5 μsec duration. The interferograms shown were taken immediately after the gain switched spike. At later times, the fringe pattern becomes too chaotic for interpretation, mostly due to the appearance of ablation products from the plasma tube walls as the plasma temperature increases. The onset of this effect can be clearly seen in the heated interferogram shown in Figure 8.1.

The interpretation of the interferograms deserves some explanation. At the ruby laser wavelength, each fringe corresponds to an integrated electron density of $3 \times 10^{17}/cm^2$. Although the axial electron density distribution is unknown, the plotted values assume that it is constant along the length of the tube. Therefore the density is



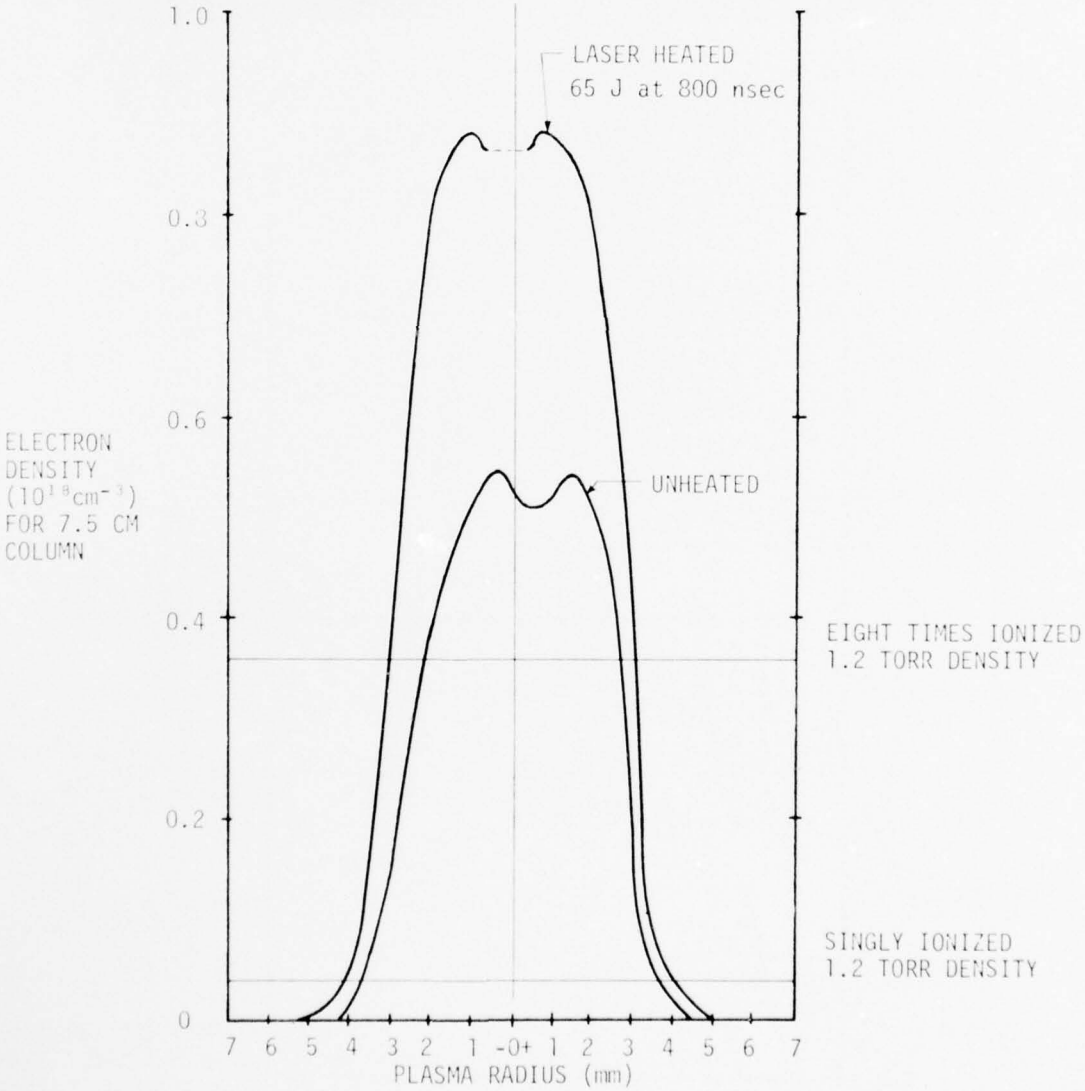


Figure 8.1. Neon Density Profiles in Fast Solenoid
B_{max} = 160 kG, 1.2 Torr Initial Fill Pressure
$t_{\frac{1}{4}}$ = 2.0 μsec $t_{picture}$ = 0.9 μsec

76 00218

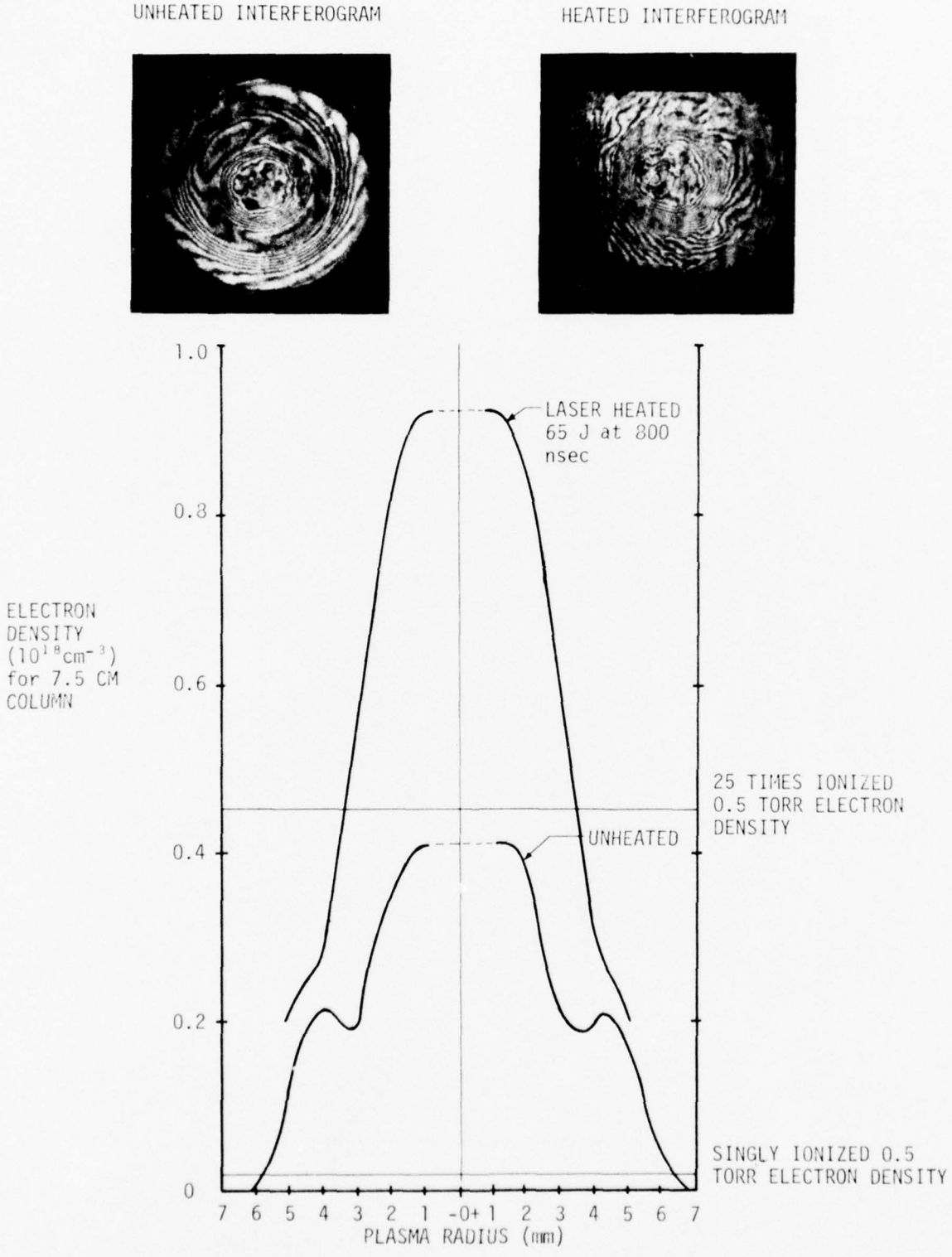


Figure 8.2. Krypton Density Profiles in Fast Solenoid. B_{max}=160 kG, 0.5 torr Initial Fill Pressure. $t_{\frac{1}{4}}$ = 2.0 μsec, $t_{picture}$ = 0.9 μsec

76 00219

evaluated as $N_e(r) = n(r) \times 3 \times 10^{17}/7.5$ (cm^{-3}) where n(r) is the number of fringes crossed to reach the point (r) going from a zero density region. In the case of the heated krypton interferogram shown on Figure 8.2, no zero reference can be established, and it is assumed that the density in the "shoulder" region is unchanged during the heating process. It is not possible to actually determine if a density minimum has been formed during the heating process because the fringes are blurred due to plasma motion and perhaps due to refraction in steep density gradients in the central region.

The lines indicating various degrees of ionization on Figures 8.1 and 8.2 are for an uncompressed plasma. As discussed in Section IV, the initial z in the unheated neon is about 3, and increases to about 8 on heating. In krypton, z must be quite high in the center, but quantitative interpretation is impossible due to the fact that gradients in z must exist over the broad profile. In any case the degree of ionization is more than doubled by laser heating of the krypton column.

2. X-Ray Emission from Laser Heated Krypton Plasmas in Fast Solenoid

Although the calculations of Section 3.5 showed that for the laser energies and magnetic field intensities that could be obtained, no L-shell x-radiation should be produced from krypton, a few laser heating experiments were performed on krypton with the X-ray diagnostics operating. The XRD package was set-up as indicated in Section 7.2 with 1.0 mil Be, 0.5 mil Be, and 0.5 mil Al filters in place. Several curious and, as yet, not fully understood phenomena were found in the course of these experiments. They are illustrated by the waveforms shown on Figure 8.3a. "X-ray" signals were frequently observed at the start of the solenoid. These were probably due to electron runaway during the gas breakdown, and have previously been noticed in operating a theta pinch with H_2 filling. Occasionally, bursts of this type occurred near current maximum even in the absence of laser heating. Fast bursts of "X-rays" sometimes occurred concurrent with the first laser heating spike, and these are seen in the example shown. Curiously, these pulses did not

affect all three detectors on any given shot. If they were due to X-rays at all, they must have been from very restricted zones in the plasma, and the detectors not seeing them were in "shadows" cast by the plasma tube in the sense discussed in Section 7.2. It should be noted that in this experiment, the detectors were all at r = 0.98", and would have been shadowed only if the source were very close to the tube wall. An alternate explanation is that these signals were caused by fast electrons which arise from small regions in the plasma and are channeled along flux lines to only some detectors.

The other type of X-ray signal found in the krypton heating experiments is also seen in Figure 8.3a. This is a signal that rises slowly during the tail of the laser heating pulse, peaking at the end of the laser pulse. The same sort of threshold behavior as seen for first spike neon heating is seen here, based on the total laser energy. At lower laser energies, no slowly rising signal is obtained. The largest signal seen was about 50mV on the 0.5 mil Be covered XRD. It decays very slowly over a time of several microseconds, with the decay rate varying with filter foil thickness in a way that suggests a "softening" of the radiation responsible as a function of time. This signal increased consistently with increasing laser energy. The intensity ratios between different pairs of filter foils were remarkably consistent and are summarized below in Table 8.1.

Table 8.1.
Foil Transmission Intensity Ratios for Krypton Plasma

FOIL COMBINATION	RATIO AT PEAK	RATIO 1.5 sec AFTER PEAK
I(1 mil Be)/I(0.5 mil Be)	0.56 ± 0.07	0.36 ± 0.05
I(0.5 mil Al)/I(1.0 mil Be)	0.36 ± 0.05	0.26 ± 0.12

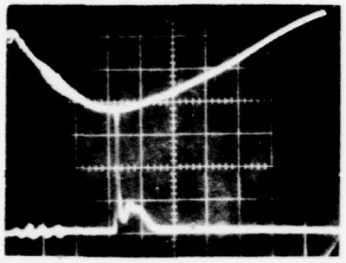
If one tries to fit these intensity ratios to the transmission ratios for spectrally integrated bremsstrahlung, found in Elton,[16] then one finds reasonable agreement between the two ratios. A "bremsstrahlung temperature" of T_e = 0.45 keV at the time of peak intensity is found, cooling to about 0.30 keV in 1.5 μsec. This of course, cannot represent

B_o = 160 kG

P_o = 0.5 torr Kr

Laser 50 kV, $3^1/_2$ atm, $3/^1/_2/1$

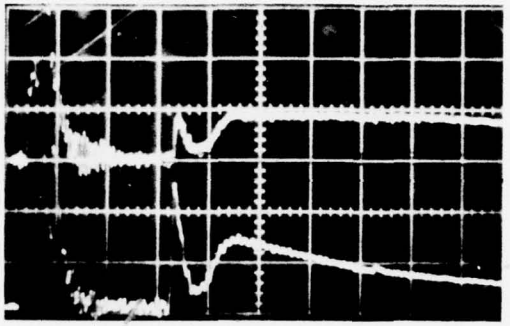
E_T = 280 J



PINCH
MONITOR
1v/DIV

PHOTON
DRAG
0.2 v/DIV

0.5 μsec/DIV



APERTURE
0.150 IN. WITH
SCREEN

XRD1
0.5 mil Be
0.05 v/DIV

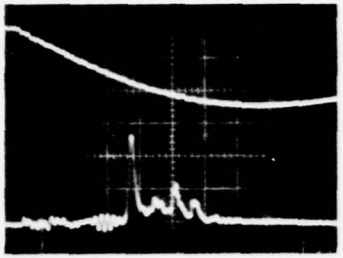
XRD2
1.0 mil Be
0.02 v/DIV

0.5 μsec/DIV

76 00220

Figure 8.3a. Typical Waveforms in Krypton Heating Experiment in Fast Solenoid

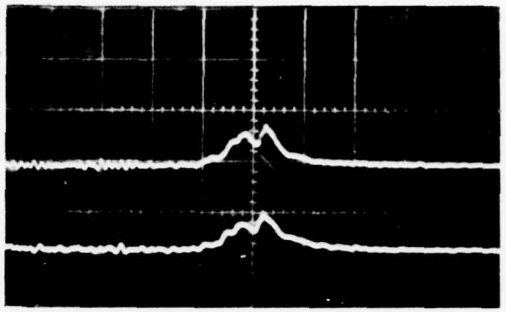
B_o = 160 kG
P_o = 1.2 torr Ne
Laser 50 kV, $3^{1}/_{2}$ atm, $3/^{1}{}_{2}/1$
E_T = 256 J



PINCH
MONITOR
1v/DIV

PHOTON
DRAG
0.2 v/DIV

200 nsec/DIV



APERTURE
0.150 IN. WITH
SCREEN

XRD1
0.5 mil Be
5.0 v/DIV

XRD2
1.0 mil Be
1.0 v/DIV

200 nsec/DIV

Figure 8.3b. Typical Waveforms in Neon Heating Experiment in Fast Solenoid



VACUUM SHOT,
LASER ONLY



1.2 Torr Ne in
Solenoid. Laser
Fired at, Current
Maximum B_o = 160 kG
E_T = 100 J

Line Electron
Density $\approx 3.6 \times 10^{18}\ cm^{-2}$

Figure 8.3c. Burn Patterns 12 Inches Behind Laser Vacuum Focus

76 00221

a true temperature of the dense plasma since the line and continuum intensities would then be much stronger than measured. The calculation shown in Figure 3.12 also shows a much lower temperature of 0.17 keV, and this is assuming an initially 8 times ionized plasma. The interferogram shown in Figure 8.2 implies somewhat lower initial and final degrees of ionization, although this must be partially due to column shrinkage.

The high ratios of transmission between the two beryllium foils does tend to indicate at least some component of fairly hot x-rays. The lower aluminum transmission suggests much of the radiation is beyond the 1.56 keV aluminum absorption edge. The most mystifying phenomena is the long decay time, with radiation persisting well after the zero point in the confining magnetic field. Some trapped field confinement is still possible, but all evidence points to recombination radiation from a fairly low density plasma. The temperatures implied by the high foil transmission ratio do not agree with the calculations shown in Figure 3.12, but are not inconsistent with the scaling law temperatures given by Equation 2.7, even in the lower fields near the exit of the solenoid. Laser focusing to areas smaller than the 3.6 mm assumed in the calculations of Section 3.5 could produce higher temperatures. Unfortunately, the low level of the radiation makes any detailed spectral measurements impossible, and instrumentation malfunction must be regarded as just as likely an explanation for the observed phenomena as any of the above postulating.

3. Laser Heating of Neon Plasma in the Fast Solenoid

Laser heating experiments in the fast solenoid with a neon plasma were done along essentially the same lines as those discussed in Section 7.3, that is, using the low intensity tail of the laser pulse. Some significant differences did exist, however, between the operation of the theta pinch and the laser, and these allowed a greater variation in experimental parameters, or more "knobs to turn" in the solenoid experiments. It is this area that was explored in more detail, using the fast solenoid.

As seen in Section 5.5, for a wide range of filling pressures, the solenoid plasma reached a nearly steady state in about 700 nsec, without the neutral "hole" seen in the theta pinch. This allowed a variation of initial pressure, and also of magnetic field at the time of laser firing. The laser-magnet firing could be altered without seriously changing properties such as the integrated electron density. Once the "hole" disappeared, the integrated electron density decreased very slowly. This probably represents a balance between end flow, compression, diffusion, and recombination, but it is not expected that the actual electron density or state of ionization changes much after 700 nsec.

Laser burn patterns were taken on exposed polaroid film at the far end of the plasma to see if the absence of a preformed density minimum would affect the beam propagation. The film was located in a tube 12 in. behind the laser focal point. Any significant 10.6 μ radiation transmitted through the plasma would burn the film as indicated by the "vacuum" shot burn pattern on Figure 8.3c. If the laser radiation were refracted out of the plasma, a dispersed pattern, or no burn at all, would be expected. On the other hand, concentration of transmitted radiation on axis would demonstrate "hole burning" and trapping of the laser radiation. The vacuum reference shot shows the typical annulus resulting from the unstable oscillator mode pattern. Also shown in Figure 8.3 is a pattern of radiation transmitted through a neon plasma for laser irradiation beginning at peak magnetic field. The region of maximum intensity is at the axis of the pinch, showing trapping. The "caustic structure" of the rest of the burn pattern is quite typical and probably results from slight azimuthal nonuniformity of the exit region of the plasma. Diffraction like effects are seen in these patterns, indicating some preservation of spatial coherence in the transmitted beam. The burn pattern shown represents about the maximum amount of transmitted radiation,

which was estimated at a joule. For laser irradiation at earlier times, when more plasma was present, the transmitted radiation was diminished. Thus, the lack of a density minimum does not seem to present any problems to the heating process.

The x-ray diagnostics used in these experiments were the same as those discussed in Section VII. A typical record of a heating experiment is shown in Figure 8.3b. As in the theta pinch slow heating experiments, x-ray signals begin after the first spike and grow during continued heating. The spiking behavior of the laser due to backscatter was similar at similar fill pressures, but disappeared completely at higher fill pressures. It should be noted that spiking was never observed for krypton fills, and very seldom for He-Ne mixtures. The most pronounced spiking was observed for neon fill pressures below 1.0 torr, with even higher intensity after spikes produced than shown in the trace on Figure 7.10.

Figure 8.4a summarizes the variation of x-ray output energy with initial filling pressure in the plasma tube. A maximum is reached at around 2 to 2.5 torr, and the peak value of 2.5 J was the highest attained in any of the neon heating experiments. At higher filling pressures, available laser power is probably a limiting factor. Figure 8.4b shows the variation of peak x-ray output power with the value of magnetic field when laser heating began. The relation between B(t) and t is of course $B(t)/B_0 = \sin(\pi/2 \cdot t/\tau_{1/4})$, hence low values of B(t) represent quite early times. A constant solenoid bank voltage, and thus constant B_0 was used here. No clear variation of heating efficiency with B(t) can be seen, except that on the average, one does best by starting to heat at B $\approx$ 100 kG. This means then that most of the slow heating is done before the peak field is reached. The point at B(t) = 50 kG represents heating beginning at $\approx$ 300 nsec, before the plasma is well formed, and thus the x-ray output is lower.

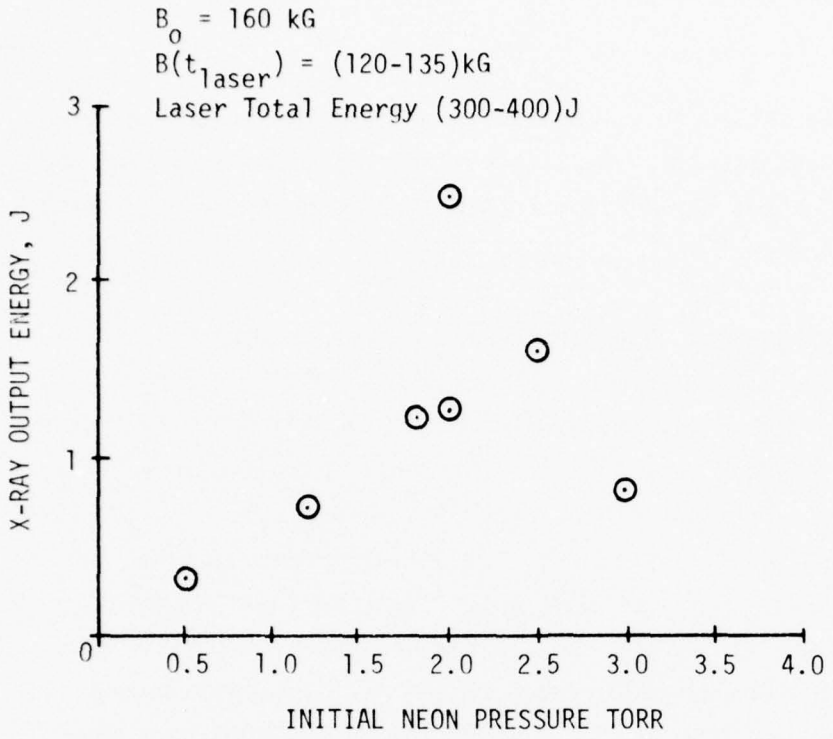


Figure 8.4a. Variation of X-ray Output Energy with Initial Fill Pressure of Neon, B_o, E_{laser} Approximately Constant

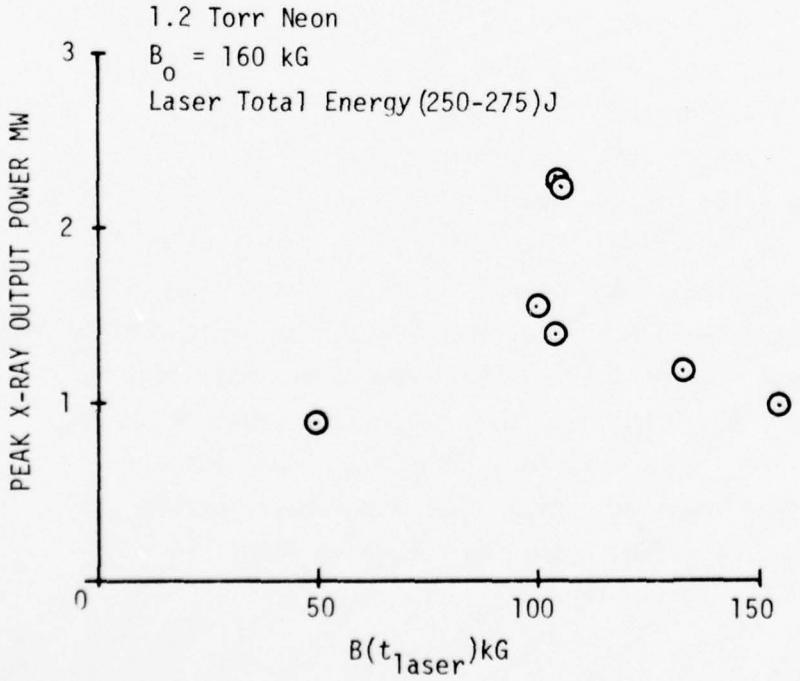


Figure 8.4b. Variation of X-ray Output Power with Magnetic Field at Time of Laser Firing. B_o, P_o, and Laser Energy Constant.

76 00222

4. Time Integrated Neon X-Ray Spectrums

The 2.5 J x-ray output energies suggested that useful x-ray spectrum might be obtained using 0.5 mil Be foil with only a few exposures. A description of the SRI spectrometer used is contained in Appendix I, which is Stanford Research Institute's report on the bent crystal spectrometer and thermopile calorimeter they built for us under contract to DNA. Their discussion of crystal efficiency can be summarized here to derive expected x-ray fluences in the film plane. The entrance plane of the spectrometer was located 20 cm from the entrance of the plasma tube, and the crystal another 5 cm behind this plane. For a crystal location 25 cm from the plasma, 1 J of emitted x-rays will produce a flux of 1.27×10^3 ergs/cm^2 at the calorimeter, or approximately 100 ergs/cm^2 of 0.93 keV x-rays transmitted through a 0.5 mil Be foil.

An x-ray will be diffracted only when its angle of incidence to the crystal normal satisfies the Bragg equation $\sin\theta = n\lambda/2d$ where n is the diffraction order and d the crystalline interplaner spacing (equal to 13.32 Å for KAP). The fractional diffraction for x-rays striking a portion of the curved crystal where the Bragg equation can be satisfied is thus proportional to the radius of curvature of the crystal multiplied by an effective angular spread where the Bragg equation is satisfied, and is inversely proportional to a dimension, a, equal to the height of the incoming beam. The fractional diffraction χ can be defined as

$$\chi = \frac{\varepsilon}{a} \tag{8.1}$$

where ε is defined as the diffraction efficiency, and is plotted in Appendix 1 as a function of wavelength. Typical values at 0.93 keV are $\varepsilon = 5 \times 10^{-5}$ cm, and a is approximately 0.25 cm.

The input fluence per unit width of the crystal is $\varepsilon_{in} = aI_{in}\Delta t$, and the diffracted fluence per unit width is just

$\varepsilon_{diff} = \chi\varepsilon_{in} = \varepsilon I_{in}\Delta t$. The fluence at the film plane is then

$$\theta(erg/cm^2) = \frac{\varepsilon_{diff}}{\Delta s} = \varepsilon \frac{\Delta E}{\Delta s} \phi_{in}(ergs/cm^2\text{- keV}) \qquad (8.2)$$

where $\phi_{in} = I_{in}\Delta t/\Delta E$ and $\Delta E/\Delta s$ is the dispersion at the film plane. For 1 keV x-rays $\Delta E/\Delta s \approx 0.25$ keV/cm at the near film plane described in Appendix 1, and thus $\theta \approx 1.25 \times 10^{-5}\ \phi_{in}$. The Doppler width given by equation (3.22) for neon ions at 0.16 keV is 0.22×10^{-3} keV, yielding a value of $\phi_{in} \approx 5 \times 10^5$ ergs/cm^2- keV and a film plane fluence of 6 ergs/cm^2. Kodak no-screen film requires approximately 10^8 photons/cm^2 or 0.16 ergs/cm^2 at 1 keV for exposure, and fine grain positive approximately 100 times this amount.

Unfortunately, the above derivations only apply for perfectly collimated x-ray beams, although similar results are obtained for beams originating from point sources. The collimators supplied with the SRI spectrometer had two 5 mm holes spaced 2 cm apart. This only serves to reduce scattering effects and gives no angular restrictions. The x-ray source must be analyzed from the point of view of being a 5 mm diameter source. The angular deviation from a point source is thus 0.017 radians at 30 cm, and the minimum resolution of a film plane located 5 cm from the bent crystal will thus be 0.08 cm. This must be compared with the pure Doppler width of 0.22×10^{-3} keV and 0.001 cm. The fluence at the film plane calculated from the Doppler width is thus reduced by a factor of 80 to 0.08 ergs/cm^2. This value is further reduced in half by a 48 percent transmitting screen support behind the 0.5 mil Be foil (necessary to prevent blast damage). The resultant 0.04 ergs/cm^2 is only 1/4 the value required to expose no-screen film (assuming 1 joule of x-rays is emitted at the 0.92 keV resonance line), and approximately 4 exposures should be necessary to obtain a good spectra.

The spread in intensity at the film plane implies a minimum resolution of 0.02 keV. A collimator consisting of 19, 0.030 in.

ID by 3 in. long tubes was constructed to restrict the angular spread to 0.01 radians, but it is obvious that this will reduce the film plane fluence to a value too low to measure.

The SRI double bent crystal spectrometer described in Appendix 1 was set up as shown in Figure 8.5, with the entrance plane of the spectrometer located 8 inches from the near end of the plasma tube. Both the upper and lower spectrometers were used simultaneously, and both were set at an angle of 6.5 degrees from the experiment axis so that the spectrometer axis intersected the experiment axis at approximately the end of the plasma tube. The upper spectrometer was fitted with the tube collimator described above. On this spectrometer, the internal collimator was removed and the crystal oriented to accept maximum illumination from the external collimator. The lower spectrometer was used with the internal collimator with the source dimensions only providing angular resolution. It was provided with a screen supported entrance foil of 0.5 mil Be. A normal slotted solar collimator would have been an improvement, reducing the angular spread in only one direction (the direction of dispersion), but would still cut the fluence down to too low a value in our experiments.

The x-ray spectral measurements were made at the end of the contract period, and only two useful runs were obtained before the laser had to be shut down for maintenance. The first run consisted of 5 exposures with a total x-ray fluence of 3 J (as measured by the XRD detectors at the far end of the plasma tube), and the second run had 2 exposures with a total x-ray fluence of 4.5 J. The no-screen film was developed for four minutes in duPont Cronex, x-ray film developer and fixed normally. The same spectra was present on both films and a densitometer tracing of the slightly more exposed, higher x-ray fluence film is displayed on Figure 8.6. The exposures were so weak that the lines are barely above the background level.

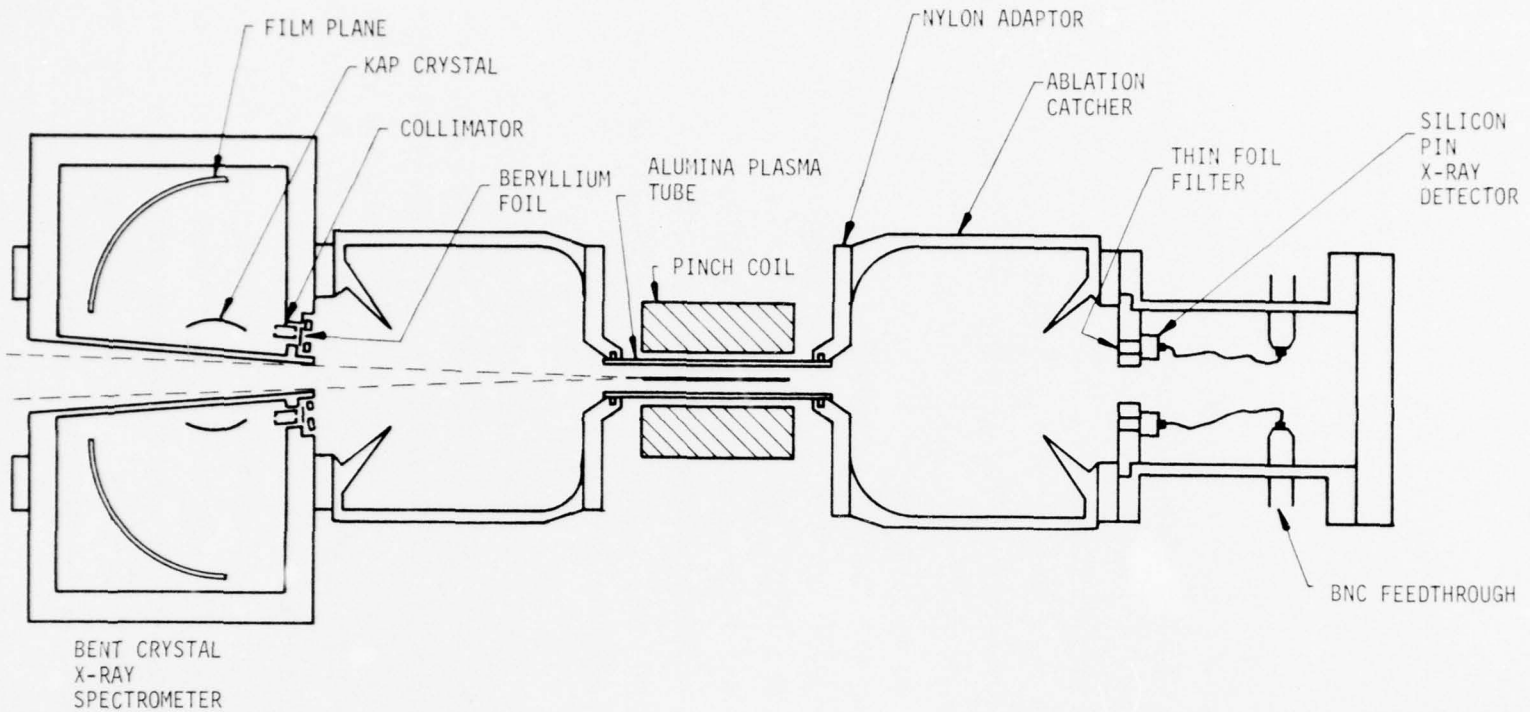


Figure 8.5. Setup of SRI Double Bent Crystal Spectrometer on Fast Solenoid Pinch

The energy scale shown on Figure 8.6 was devised from the film distances in the following manner. The dispersion curves supplied by SRI in Figure 3 of Appendix 1 apply to a collimated source alligned with the spectrograph axis shown in Figure 3 of Appendix 1, but these curves seem to apply to second order dispersion. We used the measured spectrograph geometry and Bragg diffraction relation to derive the curve shown on Figure 8.7. The origin on the film is taken as the sharp edge where the undiffracted radiation striking the film is stopped by the crystal. The additional lines on the Figure indicate uncertainties in the angle between the spectrometer axis and the heated plasma. This was set as carefully as possible to zero by setting the spectrometer adjustment to 6.5 degrees and placing the 0.9 in. high entrance hole 8 inches from the plasma tube. However, errors of about 2 degrees are possible in aligning the spectrometer assembly with the plasma tube axis and these 2 degrees misalignment calculations are the ones displayed by dashed lines on Figure 8.7. An additional 1 degree error is introduced by the 5 mm size of the heated column.

The plotted point at 1.6 keV represents a line obtained upon irradiating the aluminum target described in Section 3.1. The other point is obtained from the lowest energy densitometer peak in Figure 8.6, assuming that it is due to the 0.92 keV He-like resonance line. Since the two pictures were taken with different alignments. The points do not fall on the same curve. Crystal orientation and geometric errors can account for the neon line falling outsize the 2 degree error curves. The energy plot on Figure 8.6 was devised using the He-like resonance line as a reference point and translating the calibration curve of Figure 8.7 sidewards.

Some of the expected He-like neon lines are indicated on Figure 8.6. The resonance and intercombination line cannot, of course, be distinguished due to the 0.02 keV resolution, nor can Li-like satellites at 0.91 and 0.90 keV. A surprising feature, bu[illegible]ne hinted at by the

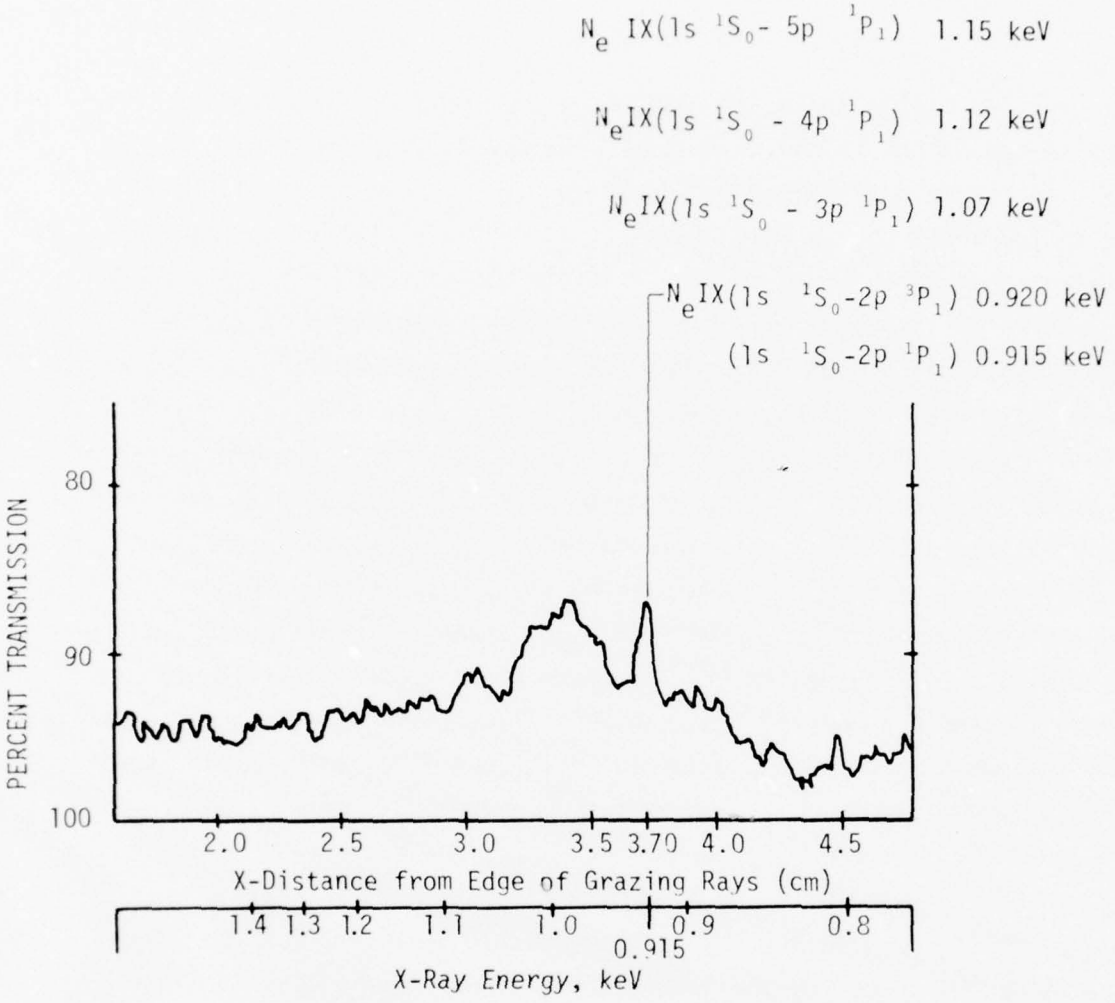


Figure 8.6. Densitometer Tracing of Neon Spectrum with Tentative Identification of Spectral Lines

76 00224

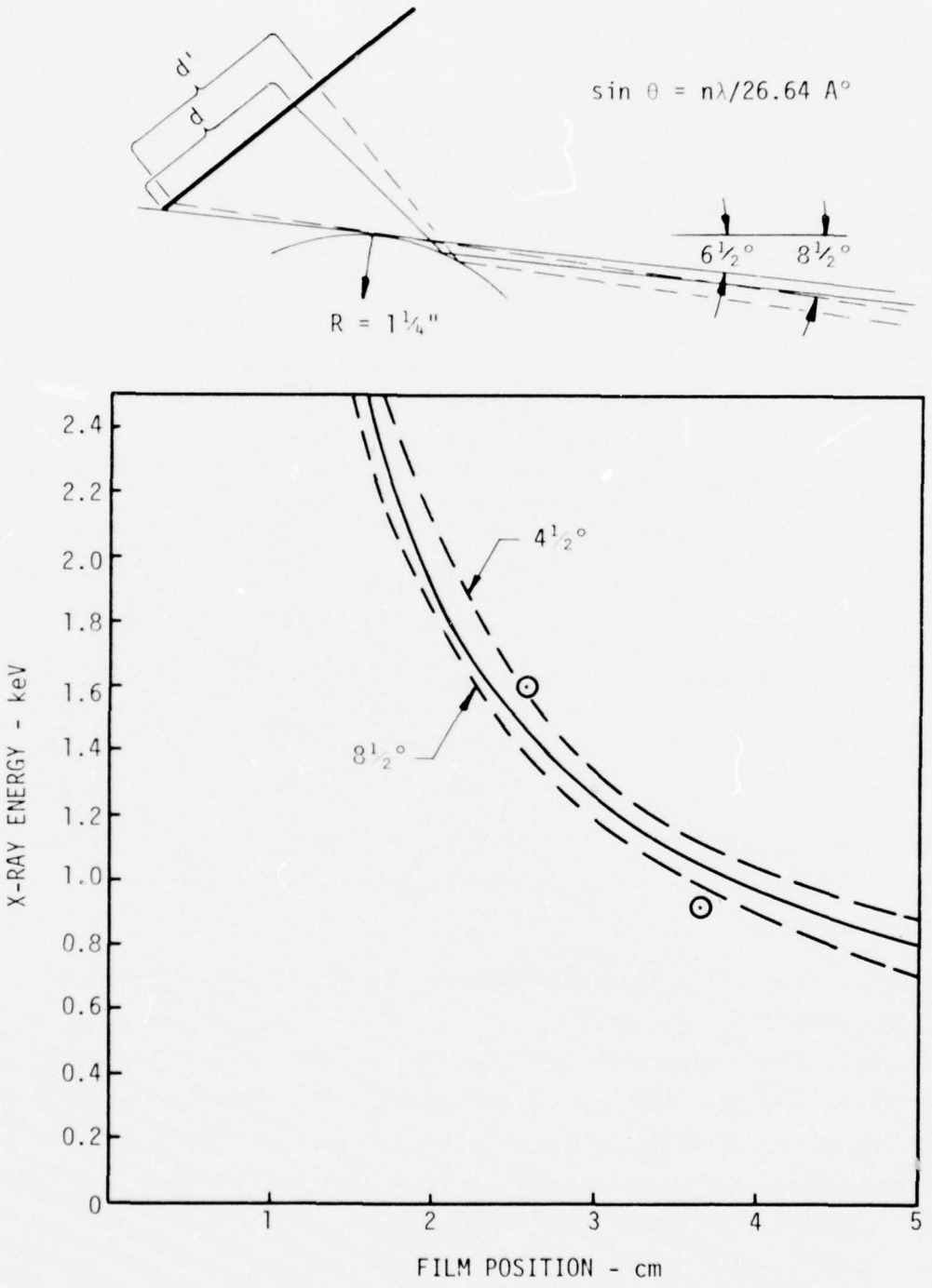


Figure 8.7 Theoretical Calibration of KAP Bent Crystal Spectrograph in Near Film Plane

76 00225

foil transmission ratios discussed previously, is the strong feature around 1.0 keV. An examination of the relevant f-numbers would lead to a prediction of dominant resonance radiation. The f-numbers for relevant transitions as listed by Wiese et al.[2] are listed below in Table 8.2.

Table 8.2
Ne IX Allowed Transitions

Transition	Energy	f-Number	Excitation Rate
$1s^2\ ^1S$ - $1s\ 2p\ ^1P^0$	0.92 keV	0.723	0.625 μsec^{-1}
$1s^2\ ^1S$ - $1s\ 3p\ ^1P^0$	1.07 keV	0.149	0.043 μsec^{-1}
$1s\ 2p\ ^1P^0$ - $1s\ 3d\ ^1D$	0.15 keV	0.703	0.46 $nsec^{-1}$
$1s\ 2p\ ^3P^0$ - $1s\ 3d\ ^3D$	0.16 keV	0.672	0.39 $nsec^{-1}$
$1s\ 2s\ ^1S$ - $1s\ 3p\ ^1P^0$	0.16 keV	0.386	0.22 $nsec^{-1}$
$1s\ 2s\ ^3S$ - $1s\ 3p\ ^3P^0$	0.17 keV	0.365	0.19 $nsec^{-1}$

All the $\Delta n = 1$ transitions listed have the excitation rate derived from equation (3.11) at Te = 0.16 keV, $\overline{n_e} = 1$, and $\langle g \rangle$ set equal to 0.2. The 1s - 2p resonance transition is seen to have a 15 times greater excitation rate than the 1s - 3p transition. The rate for radiative decay of the $1s\ 2p\ ^1P^0$ state is $8.9 \times 10^3\ nsec^{-1}$ so that even accounting for self absorption coefficients of 3.5 mm^{-1} (see Section III), multistep excitation to the 3d level is unimportant.

Any multi-step excitation to the n = 3 level must proceed via the forbidden transitions a, c, and d shown in Figure 3.4. Table 8.2 shows the excitation rates for the upper levels of these transitions into the 3p and 3d states to be very rapid, probably of the same order as the collisional relaxation to the $2p\ ^1P^0$ state. Thus, a reasonable

fraction of forbidden transition excitations end up in the n = 3 level. The path via the ^1S forbidden transition ends up directly in the $1s\,3p\ ^1P^0$ state where it will immediately radiate to the ground state, while the paths via triplet states require collisional relaxation in the n = 3 level and will incur additional branching ratios before radiating to the ground.

The above arguments show that radiation from the 3p level can be a significant fraction of the 2p radiation, perhaps as as high as 50 percent. This is less than the 1 to 1 ratio inferred in Section 3.2 from the foil transmission ratios, but the latter ratios are extremely sensitive to imprecision in the foil thicknesses. The spectra on Figure 7.6 shows about equal energies from the 2p and all other levels when account is taken of the variation in foil transmission and diffraction efficiency.

REFERENCES

1. A. L. Hoffman, "Laser Heating of Magnetically Confined Plasmas for X-Ray Production," MSNW Report No. DNA 3251F, and MSNW 74-118-1, Mathematical Sciences Northwest, Inc., Seattle (1973, 1974).

2. T. W. Johnston and J. M. Dawson, "Correct Values for High-Frequency Power Absorption by Inverse Bremsstrahlung in Plasmas", Physics of Fluids 16; 722 (1973).

3. W. L. Wiese, M. W. Smith, and B. M. Glennon,"Atomic Transition Probabilities", NSRDS-NBS 4 , U. S. Government Printing Office, Washington, D.C. (1966).

4. R. W. P. McWhirter, in Plasma Diagnostic Techniques, (ed. R. H. Huddlestone and S. L. Leonard) Academic Press, New York (1965).

5. H. J. Kunze, Phys. Rev. A3, 937 (1971).

6. R. C. Elton, in Methods of Experimental Physics, Vol. 9, Part A (Plasma Physics); ed. by H. R. Griem and R. H. Loveberg, Academic Press, New York (1971).

7. C. W. Allen, Astrophysical Quantities, Athlone Press, London (1965).

8. J. Davis, "Effective Gaunt Factors for Electron Impact Excitation of Multiply-Charged Nitrogen and Oxygen Ions", J. Quant. Spectro. Radiat. Transf. 14 (1974).

9. H. R. Griem, Plasma Spectroscopy, McGraw-Hill, New York (1964).

10. J. Davis, P. C. Kepple, M. Blaha, NRL Memo Report No. 2939 (1974).

11. L. C. Steinhauer and H. G. Ahlstrom,"Laser Heating in a Solenoid Magnetic Field", Physics of Fluids 18, 5 (1975).

12. H. Knoepfel, Pulsed High Magnetic Fields, American Elsevier Publishing Co., Inc., New York (1970).

13. J. F. Cuderman and K. M. Glibert, "An X-Ray Spectrometer for Laser Induced Plasmas," Rev. Sci. Instru. 46, 1 (1975).

14. T. S. Stratton, in Plasma Diagnostic Techniques, ed. by R. H. Huddlestone and S. L. Leonard, Academic Press, New York (1965).

15. B. L. Henke and J. C. Miller, "Ultrasoft X-Ray Interaction Coefficients", TR-3 Air Force Contract AF(637)-394, Pomona College, Claremont, California (1959).

16. R. C. Elton,"Determination of Electron Temperatures between 50 eV and 100 keV from X-Ray Continuum Radiation in Plasmas", NRL Report No. 6738 (1968).

17. R. L. Abrams, "Broadening Coefficients for the P(20) CO_2 Laser Transition", Appl. Phys. Letters 25, 10 (1974).

18. R. Massey, K. Berggren, K. Pietrzyk, "Observation of Stimulated Brillouin Backscattering from an Underdense Plasma, to be published.

APPENDIX

PRECEDING PAGE BLANK-NOT FILMED

NOT COUNTED

UNCLASSIFIED

SECURITY CLASSIFICATION OF THIS PAGE (When Data Entered)

REPORT DOCUMENTATION PAGE		READ INSTRUCTIONS BEFORE COMPLETING FORM
1. REPORT NUMBER	2. GOVT ACCESSION NO.	3. RECIPIENT'S CATALOG NUMBER
4. TITLE (and Subtitle) MEASUREMENTS OF X-RAYS EMITTED BY PLASMAS		5. TYPE OF REPORT & PERIOD COVERED Final Report for Period 25 February 1974 to 31 October 1974
		6. PERFORMING ORG. REPORT NUMBER SRI Project PYU-3251
7. AUTHOR(s) R. A. Armistead T. D. Witherly		8. CONTRACT OR GRANT NUMBER(s) DNA001-74-C-0201
9. PERFORMING ORGANIZATION NAME AND ADDRESS Stanford Research Institute 333 Ravenswood Avenue Menlo Park, CA 94025		10. PROGRAM ELEMENT, PROJECT, TASK AREA & WORK UNIT NUMBERS NWED Subtask Code W99QAXPF001-31
11. CONTROLLING OFFICE NAME AND ADDRESS Director Defense Nuclear Agency Washington, D.C. 20305		12. REPORT DATE August 1974 13. NO. OF PAGES 32
14. MONITORING AGENCY NAME & ADDRESS (if diff. from Controlling Office)		15. SECURITY CLASS. (of this report) UNCLASSIFIED 15a. DECLASSIFICATION/DOWNGRADING SCHEDULE

16. DISTRIBUTION STATEMENT (of this report)

Approved for public release; distribution unlimited.

17. DISTRIBUTION STATEMENT (of the abstract entered in Block 20, if different from report)

18. SUPPLEMENTARY NOTES

This work was sponsored by the Defense Nuclear Agency under Subtask W99QAXPF001-31.

19. KEY WORDS (Continue on reverse side if necessary and identify by block number)

Plasmas
X-Ray
Curved Crystal Spectrograph
KAP

20. ABSTRACT (Continue on reverse side if necessary and identify by block number)

A curved crystal spectrograph, with the provision for the simultaneous use of two crystals, was designed and provided to MSN. The delivered instrument contained a KAP crystal curved to a 1.25 inch radius of curvature.

A thermopile calorimeter assembly was also prepared for MSN use. This instrument had provisions for four thermopile calorimeters along with Ross or K-edge filters for the calorimeters. The calorimeter mounts can also

DD FORM 1 JAN 73 1473

EDITION OF 1 NOV 65 IS OBSOLETE

UNCLASSIFIED

SECURITY CLASSIFICATION OF THIS PAGE (When Data Entered)

19 KEY WORDS (Continued)

Thermopile Calorimeter
X-Ray Diagnostics

20 ABSTRACT (Continued)

accommodate active detectors such as the RCA scintillator-photomultiplier detector currently in use at MSN. Two 100 junction thermopile calorimeters with 0.002 inch thick gold absorbers were supplied in the calorimeter assembly.

SRI staff visited MSN and participated in instrument installation and initial experimentation. However, since the instrumentation will be used for continuing experimentation by MSN and supplemented by other measurements the results of the x-ray measurements will be reported by MSN under separate cover.

PREFACE

This program was initiated on February 25, 1974. Dr. R. E. Price was the original DNA COR, but upon his departure from DNA, was superseded by Dr. G. K. Soper. Dr. Alan L. Hoffman was the principal contact at Mathematical Sciences Northwest, Inc., and will be the experimenter employing the instrumentation developed during this program.

The authors gratefully acknowledge the contributions of Dr. T. A. Boster, Lawrence Livermore Laboratory, for his assistance in the design of the instrumentation and in the preparation of the curved KAP crystal.

CONTENTS

PREFACE 143

LIST OF ILLUSTRATIONS 145

INTRODUCTION 147

CRYSTAL SPECTROGRAPHS AND THERMOPILE CALORIMETERS 150

Curved Crystal Spectrographs 150

Thermopile Calorimeters 159

SPECTROGRAPH AND CALORIMETER ASSEMBLIES 162

Spectrograph Assembly 162

Thermopile Calorimeter Assembly 167

SUMMARY AND CONCLUSIONS 171

ILLUSTRATIONS

1. MSN Laser-Augmented Theta Pinch Plasma Source Configuration 148

2. KAP Spectral Efficiency 156

3. Dispersion Curves for MSN KAP Spectrograph 157

4. Sketch of One Side of Spectrograph with Energy Positions Noted 158

5. Sketch of Typical Thermopile Calorimeter 160

6. MSN Thermopile Calorimeter 161

7. Schematic of MSN Spectrograph 163

8. MSN Spectrograph 165

9. Schematic of MSN Thermopile Calorimeter Assembly 168

10. MSN Thermopile Calorimeter Assembly 169

5

INTRODUCTION

Mathematical Sciences Northwest, Inc. (MSN), under the support of the Defense Nuclear Agency Advanced Concepts Program, is investigating the potential of a CO_2 laser-heated, magnetically confined dense plasma column as an intense and well-controlled source of low-energy x rays. Currently, this technique is producing plasmas with temperatures of several hundred electron volts, and steps are being taken to increase the magnetic field and the laser energy to allow heating of $10^{18}/cm^3$ plasmas to kilovolt temperatures. If the basic physical questions related to this concept can be answered, then larger, higher flux devices would require only increased plasma diameters and scaled up CO_2 lasers.

One of the principal methods for characterizing any hot plasma is through detailed measurements of the emitted x rays. Since the MSN program is directed to the development of a pulsed x-ray source, x-ray diagnostic measurements are of added interest.

The objective of the SRI program was to develop diagnostic instrumentation for making x-ray measurements at the MSN facility and to provide support for initial experimentation. The MSN x-ray source, shown in Figure 1, presents certain limitations on the placement of the diagnostic experiments. On the laser beam entrance side, a propagation path must be provided for the laser along the axis of the plasma tube. On the far side of the plasma tube, consideration must be given to laser-induced damage to the light-tight windows by the transmitted and scattered laser beam. It would be possible to view the plasma through small holes through the magnetic coil. However, in addition to presenting instrumentation difficulties, the data obtained through such view ports would not be representative of the x-ray environment at potential target locations.

PRECEDING PAGE BLANK-NOT FILMED

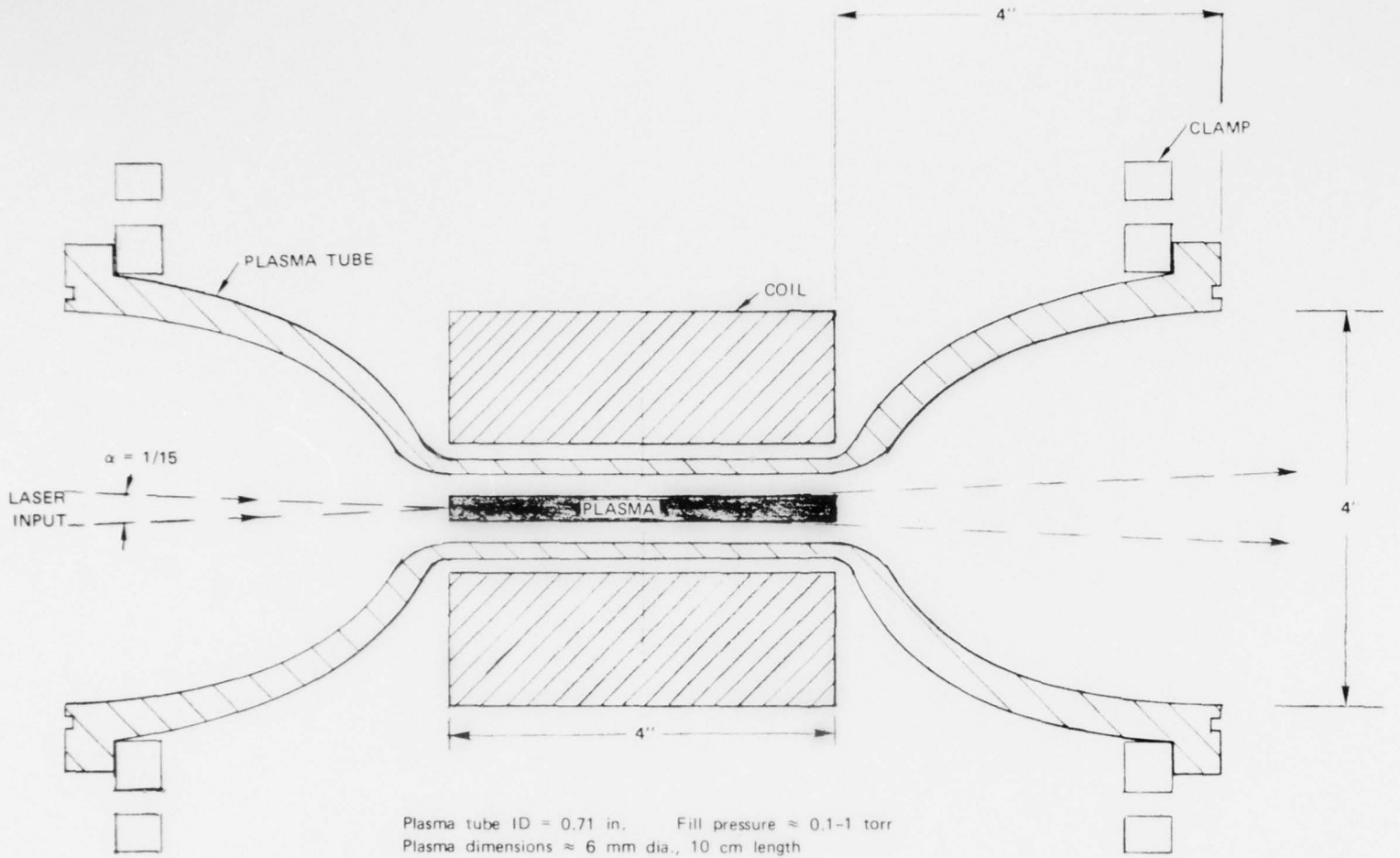


FIGURE 1 MSN LASER-AUGMENTED THETA PINCH PLASMA SOURCE CONFIGURATION

It was decided to use coaxial instrumentation assemblies that had a laser beam pass-through along the axis. This configuration results in the x-ray instrumentation being positioned slightly off axis.

The overall instrumentation concept consists of two instrumentation assemblies--one assembly with two curved-crystal mounts and film planes placed diametrically on either side of the laser pass-through, and one assembly with four detector locations to be used for either thermopile calorimeters or scintillator-photomultiplier tubes. Both assemblies were designed for use at either the laser entrance or exit side of the plasma tube. Thus, the curved crystal measurements and the thermopile measurements, which in many respects are complementary, can be used simultaneously. The crystal spectrograph design also permits the use of a pinhole plate at one of the positions normally occupied by a crystal and collimator. Thus, a pinhole image of the x-ray source can be obtained at the same time as a crystal spectrograph, providing details of the spatial distribution as well as diagnostic data, if well-calibrated films are used.

The instrumentation development includes two phases. In the first phase, which is the subject of this report, both instrumentation assemblies were fabricated. However, only one curved potassium acid phthalate (KAP) crystal and two 100-junction gold-foil thermopile calorimeters were prepared. In the second phase, an additional KAP, graphite, or lithium fluoride curved crystal and two additional thermopile calorimeters with K-edge or Ross filters will be developed if progress towards the development of the laser-augmented theta pinch source and the need for x-ray measurements warrant the additional instrumentation.

The following section discusses the basic aspects of curved crystal spectrometers and thermopile calorimeters. This is followed by a discussion of the design and fabrication of the instrumentation assemblies and a section summarizing the program and making recommendations for the possible future development of supplementary instrumentation.

8

CRYSTAL SPECTROGRAPHS AND THERMOPILE CALORIMETERS

The primary x-ray diagnostic data required to evaluate a plasma source, such as the one being developed at MSN, and to serve as the basis for design modifications are the x-ray spectrum, the fluence, and the spatial and temporal characteristics of the radiation. We designed instrumentation that permits the use of three complementary x-ray measurement techniques to provide the required diagnostic information.

The instrumentation currently includes a curved KAP crystal spectrograph to provide high-resolution spectral measurements and two thermopile calorimeters to make accurate measurements of the x-ray fluence and, with Ross or K-edge filters, to provide spectral data. The apparatus is also designed to accommodate an additional curved crystal for coverage of an extended x-ray energy range, two additional thermopile calorimeters to allow more detailed measurements, and a pinhole camera to spatially resolve the x-ray source and to give approximate fluence and spectrum information. Measurements of the pulse duration and shape can be made by mounting active detectors along the film plane in the crystal spectrograph or by replacing one or all of the thermopile calorimeters with active detectors, such as the scintillator-photomultiplier detectors currently in use as MSN, or by making a separate measurement with an active detector.

Curved Crystal Spectrographs

General Description

A curved crystal spectrograph (CCS) allows the continuous resolution of an x-ray spectrum with sufficient detail to resolve line spectra. In a CCS the collimated x-ray beam is incident on the curved crystal. Each wavelength in the beam is diffracted by the portion of the curved crystal that is at the proper angle, θ, to satisfy the Bragg equation,

$$n\tau = 2d \sin \theta \qquad (1)$$

where τ is the wavelength and d is the crystalline interplanar spacing. Bending the crystal to a convex form ensures that the Bragg condition is always satisfied at some point along the surface for any incident energy within the range for which the crystal is set and, hence, enables the simultaneous recording of all energies within this range. The use of crystals with different d spacings makes it possible to record different wavelength (energy) regions for the same range of θ values.

The use of calibrated photographic film makes it possible to record the continuous spectrum and, hence, to identify structure in the spectrum. Films have a dynamic range of two to three orders of magnitude, and the use of several film types, each having different sensitivity, allows coverage of a range of five to six orders of magnitude.

In addition to photographic films, CCSs have used other passive detectors such as thermoluminescent detectors (TLDs), slow active detectors such as thermopile calorimeters and metal-oxide-semiconductor (MOS) detectors, and fast detectors such as solid-state diodes and photomultiplier tubes.

To provide a basis for a discussion of the calibration procedures, we consider a convex curved-crystal spectrograph in basic terms. Let us define the efficiency, ϵ, of the diffracting crystal in terms of the total power, P, in ergs/sec diffracted by the crystal to the detectors, the height of the beam, L (or the crystal height if it is flooded by the beam), and the incident flux, I_o, in ergs/cm^2-sec. Thus,

$$\epsilon = \frac{P/L}{I_o} \quad (\text{cm}) \qquad (2)$$

or transposing

$$I_o = \frac{P/L}{\epsilon} \tag{3}$$

We define P in terms of the fluence, θ, diffracted along the detector plane

$$\frac{\theta}{\Delta t} = \frac{P}{L\Delta s} \tag{4}$$

where Δs is distance increment along the detector plane.

Substituting for P from Eq. (3) we find,

$$\frac{\theta}{\Delta t} = \frac{I_o \epsilon}{\Delta s} \tag{5}$$

or

$$I_o = \frac{\theta \Delta s}{\epsilon \Delta t} \tag{6}$$

Now define Φ as the spectrum incident onto the crystal (ergs/cm^2-keV)

$$\Phi = \frac{I_o \Delta t}{\Delta E} \tag{7}$$

where ΔE = x-ray energy, or

$$I_o = \frac{\Phi \Delta E}{\Delta t} \tag{8}$$

Finally, combining Eqs. (6) and (8) we obtain,

$$\frac{\theta \Delta s}{\epsilon \Delta t} = \frac{\Phi \Delta E}{\Delta t} \tag{9}$$

or

$$\Phi = \frac{\theta}{\epsilon} \left[\frac{\Delta s}{\Delta E} \right] \tag{10}$$

The term in brackets is the inverse of the crystal dispersion for the spectrograph geometry.

Thus, the spectrum measurement involves a determination of the x-ray fluence along the detector plane, θ, a knowledge of the spectrometer dispersion ratio, $\Delta E / \Delta s$, and the measurement of the diffraction efficiency of the crystal, ϵ.

The fluence measurements, θ, comes from the use of calibrated detectors. Films, since they can provide high resolution measurements, are well-suited for use in crystal spectrographs. Extensive calibration data for Fine Grain Positive (in both air and vacuum) and No Screen films over the energy range of 4 to 52 keV is available from previous programs. Limited extrapolations of the spectral sensitivity curves beyond these values can be made with confidence, particularly at the higher energies. Work now under way at LLL, hopefully,will extend these calibrations down to a few hundred electron volts.

The dispersion, $\Delta E / \Delta s$, is readily measurable with good accuracy for each spectrometer by making a broad-band spectrum exposure and using film at the detector plane. The films readily show the silver and bromine absorption edges, and these plus the K and L emission lines of the x-ray machine target, which are visible in several orders, provide all the data needed to determine the dispersion.

The crystal efficiency, ϵ, can be measured either by using the broad-band spectrum from a well-calibrated x-ray machine or by directing essentially monochromatic radiation onto the crystal and making sequential measurements of the flux at the crystal position and at the film plane.

Thus, we see that the intensity reaching the detector position depends on the fluence and spectrum of the x-ray source, the crystal efficiency of the specrograph, and the geometry of the spectrograph, which determines the dispersion. The crystal efficiency and dispersion, along with the detector response function, must be known to determine the incident

spectrum from the measured data. The resolution of the spectrograph is determined by source size, crystal, spectrograph geometry, and the characteristics of the detector used.

MSN Crystal Spectrograph

A potassium acid phthalate (KAP) convex curved crystal was chosen for initial use at MSN to provide detailed measurements of the x-ray spectrum and to determine the fluence. The crystal was curved to a 1.25-inch radius of curvature. The (001) crystal orientation will allow spectrum measurements to be made from approximately 0.6 to 10 keV. The potassium K-absorption edge at 3.6 keV produces a decrease of approximately a factor of four in the efficiency at higher energies. However, this should not preclude spectral measurements in the 3.6 to 10 keV band if there is sufficient energy in this spectral region. If higher energy measurements are designed, a graphite or LiF crystal can be prepared for use in the same spectrograph. The graphite curved crystal would allow spectral measurements over approximately the 2 to 30 keV energy range, and a LiF crystal would allow measurements from approximately 5 to 60 keV.

X-ray calibrations of the crystal and measurements of the dispersion of the spectrograph were made using a 60-KV, full-wave rectified, dc x-ray machine manufactured by North American Philips, Inc., with a copper target.

The crystal calibrations were broadband irradiations with measurements of the diffracted energy. The spectral intensity of diffraction patterns were compared with similar patterns from other KAP crystals that had undergone detailed energy point-by-point calibrations.

It has been found from calibrations of numerous KAP crystals* that the crystal-to-crystal efficiency falls within a ± 20% band. Thus, at least for the initial measurements at MSN, detailed crystal calibrations were not warranted, especially in view of the often limited life of the fragile curved KAP crystals. The spectral efficiency of KAP crystal is shown in Figure 2.

The dispersion of the spectrograph for each of the two film planes was determined directly from the diffraction pattern using the K fluorescent x rays from the copper anode of the x-ray machine and the silver and bromine L-edge absorption in the film as reference points. The spectrograph dispersion for both film planes is shown in Figure 3. The two KAP crystals supplied to MSN had different orientations resulting in slightly different dispersion curves. Thus, dispersion curves for each of the crystals are provided for the rear film plane. The slight difference in the curves for the near film plane did not warrant a separate representation. As a further aid to data reduction Figure 4 provides a sketch of one side of the interior of the spectrograph with approximate energy positions noted.

*Conversations with Dr. Burton Henke, University of Hawaii, and Dr. T. A. Boster, Lawrence Livermore Laboratory, and a variety of field test reports from the Lockheed Palo Alto Research Laboratories.

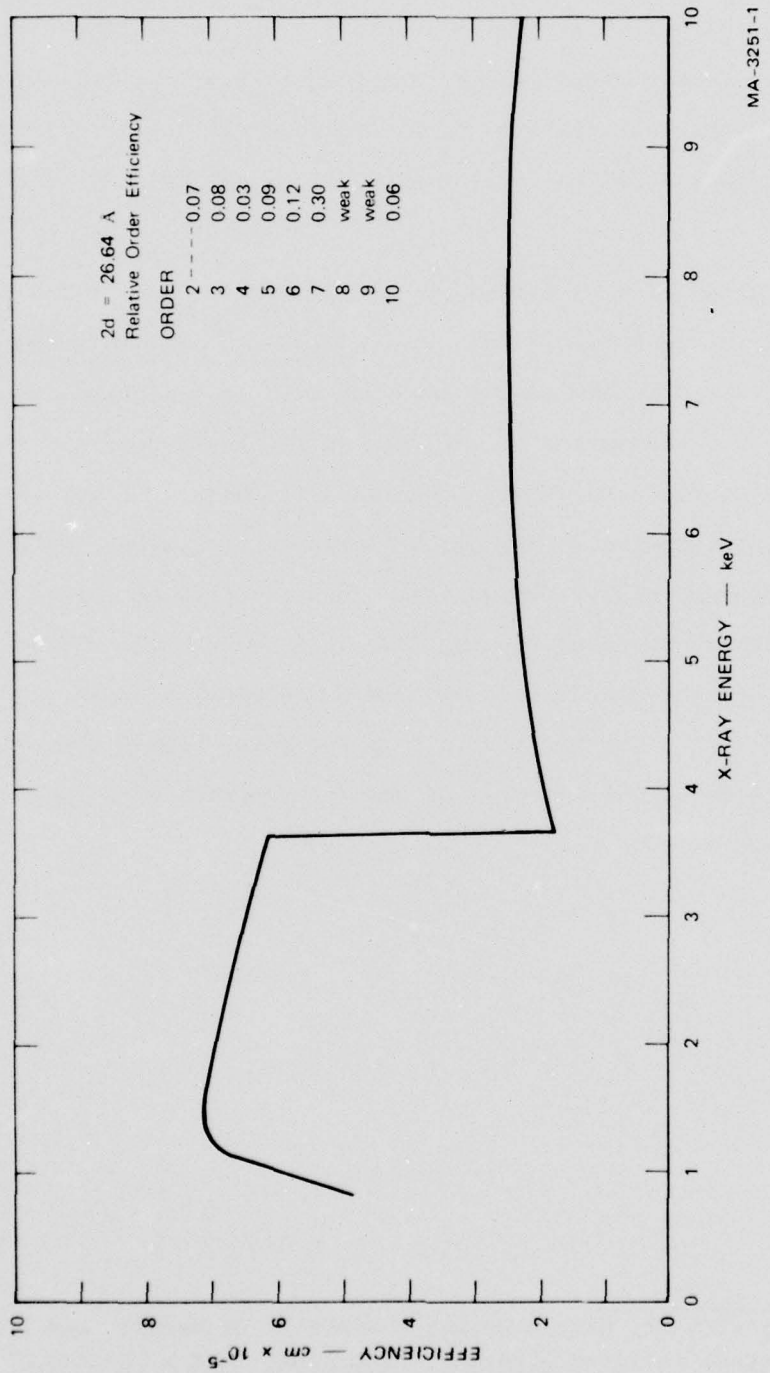


FIGURE 2 KAP SPECTRAL EFFICIENCY

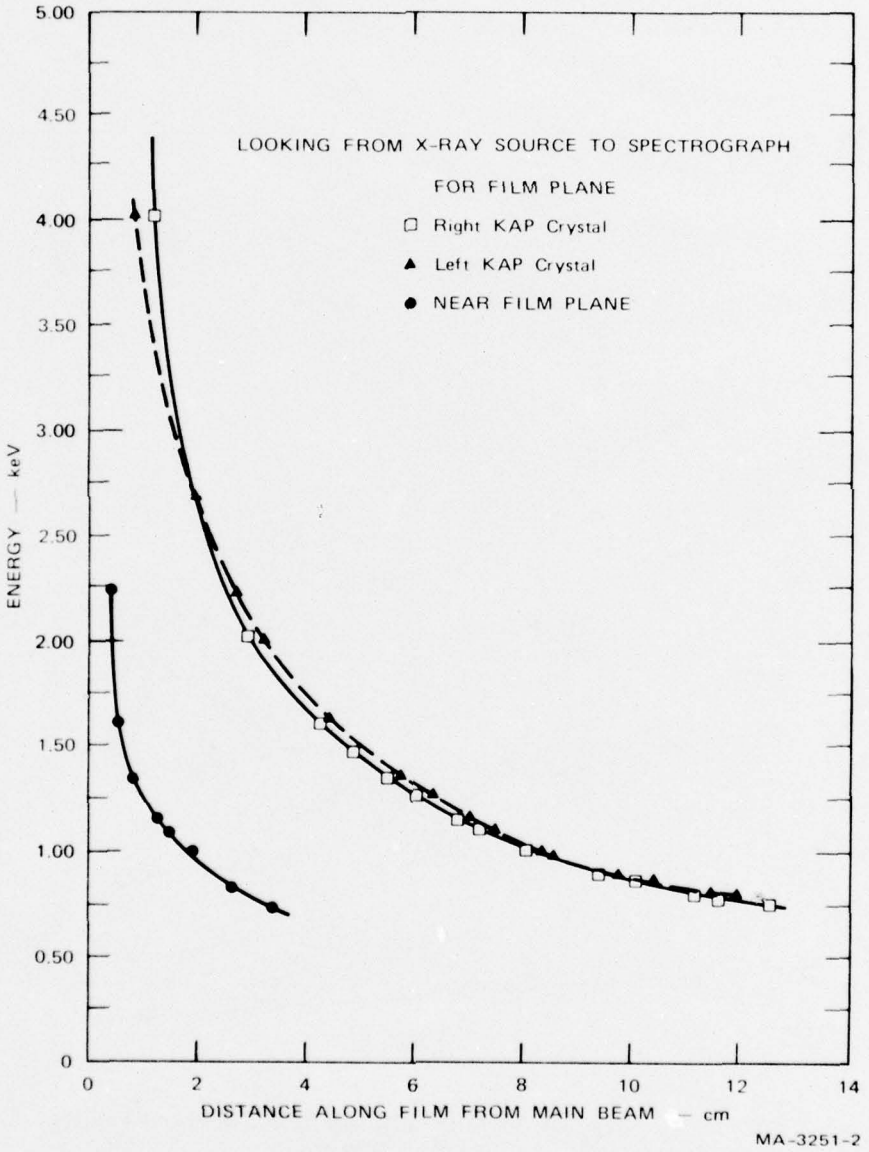


FIGURE 3 DISPERSION CURVES FOR MSN KAP SPECTROGRAPH

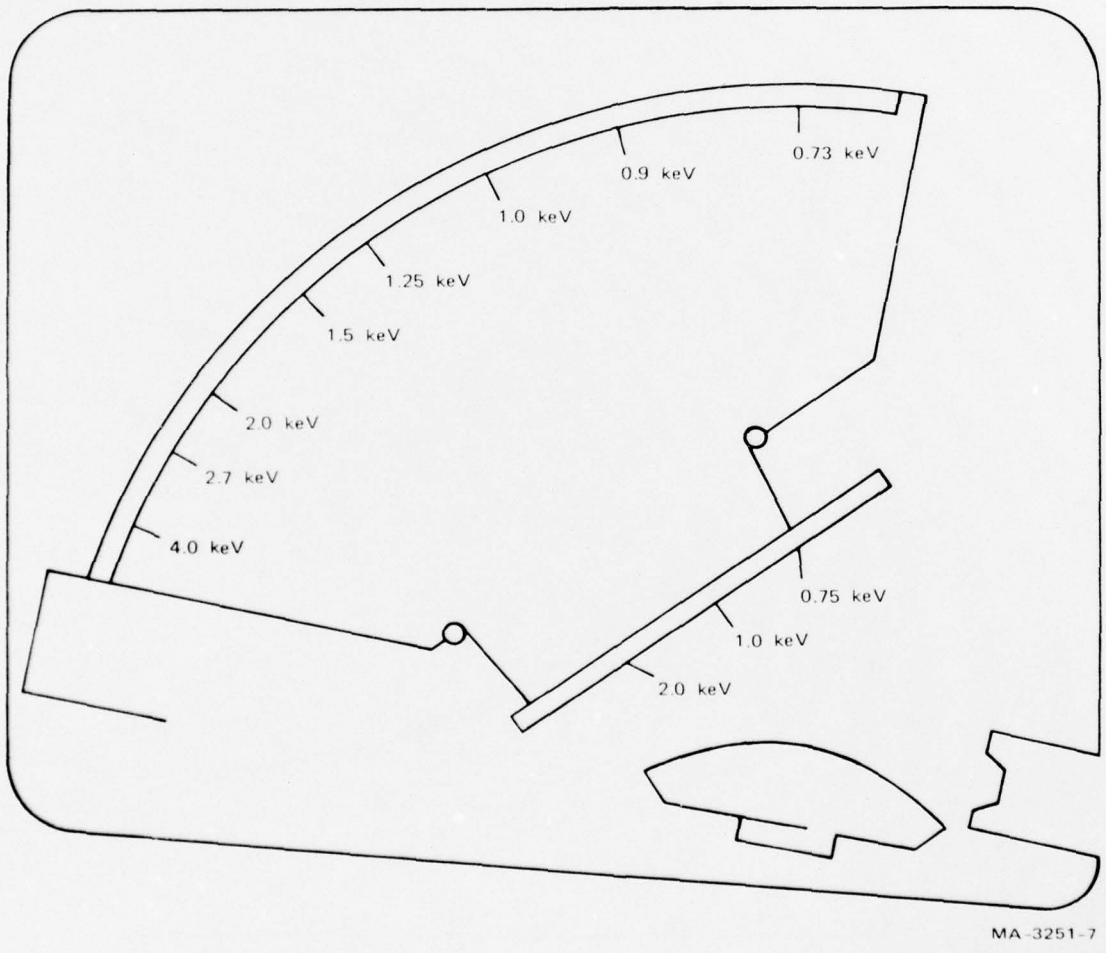


FIGURE 4 SKETCH OF ONE SIDE OF SPECTROGRAPH WITH ENERGY POSITIONS NOTED

Thermopile Calorimeters

General Description

A thermopile calorimeter is a rugged x-ray detector that provides an absolute measurement of the incident fluence with high sensitivity. A principal advantage of this detector is that it is not sensitive to the x-ray spectrum (i.e., it has a flat response) and is therefore relatively easy to calibrate.

A typical thermopile calorimeter is sketched in Figure 5, and a photograph of a MSN thermopile calorimeter is shown in Figure 6. Each element in the mosaic absorber is electrically isolated from its neighbors. The thermocouples attached to each element are series connected. Thus, a signal level results that equal to that of a single thermocouple multiplied by the number of junctions. For example, thermopile calorimeters with 100 junctions per square inch can be constructed.

MSN Thermopile Calorimeters

Two gold absorber thermopile calorimeters were designed and supplied to MSN. The thermopile calorimeters each had 100 junctions and used Chromel-Constantan thermocouples attached to each of the gold buttons. Each gold button was 0.093 inch in diameter and 0.002 inch thick; the surface dimensions of the calorimeters were 1.375 x 1.150 inches. The 0.002-inch thickness of the gold buttons is sufficient to be essentially totally attenuating ($\sim$ 99.3%) to 25-keV x rays.

The sensitivity of the calorimeters is given by,

$$I = 2.16\ \Delta V \qquad (11)$$

where I is the incident x-ray fluence in joules/cm^2 and ΔV is the measured equilibrated voltage in volts.

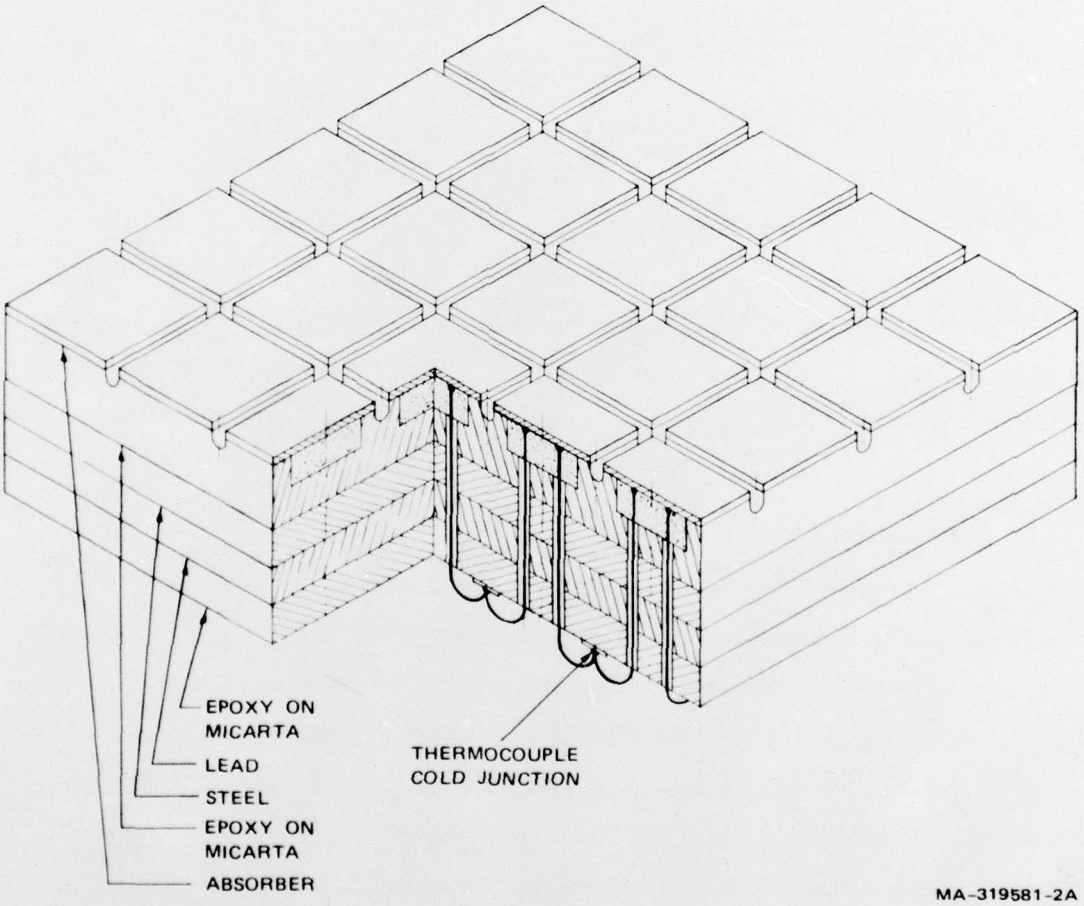


FIGURE 5 SKETCH OF TYPICAL THERMOPILE CALORIMETER

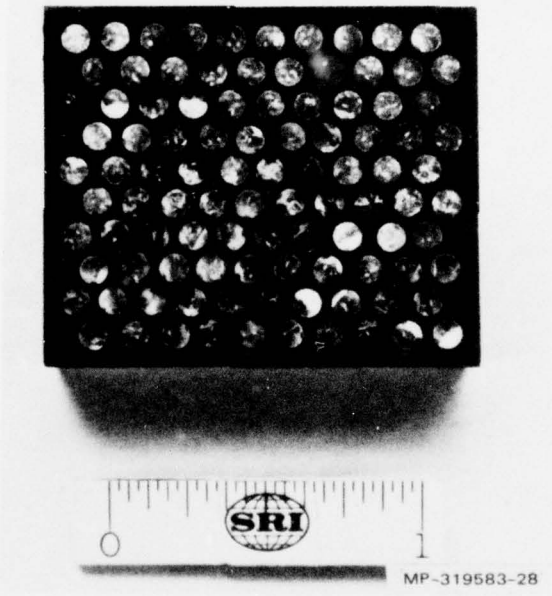


FIGURE 6 MSN THERMOPILE CALORIMETER

20

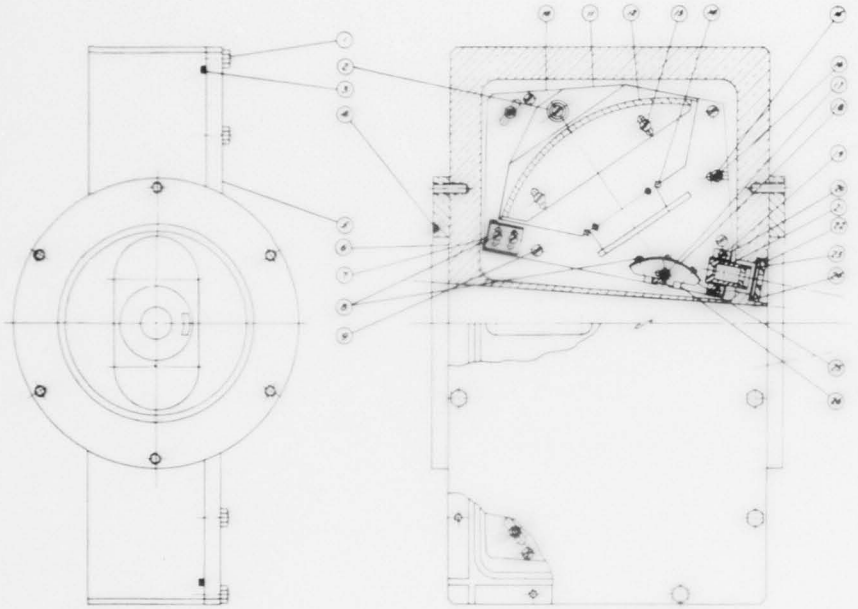
SPECTROGRAPH AND CALORIMETER ASSEMBLIES

Spectrograph Assembly

The spectrograph assembly is shown schematically in Figure 7 and a photograph of the completed unit in Figure 8. It consists of two sets of spectrograph components in a single vacuum-tight aluminum housing measuring approximately 8 inches along the axes of the laser and plasma source, 13 inches transversely, and 3 inches high. Flanges are provided fore and aft to mate with the existing MSN hardware. The spectrograph units are located off axis with a tapered pass-through between them to accommodate the laser beam. The basic components are a light-tight window, a collimator assembly to define the irradiated area, a curved crystal mount, and an x-ray trap all in a line, and film planes at two distances from the crystal. All these components are mounted on a common base plate that can rotate to vary the axis of the unit $\pm$ 2.5° from the design angle of 9° relative to the laser/plasma source axis. As a result the distance between the spectrograph assembly and the plasma source can be varied from about $3\frac{1}{2}$ to $6\frac{1}{2}$ inches while maintaining proper alignment.

Circular discs of aluminized Mylar cemented to fiber washers will be provided as the light-tight windows, although other materials can be substituted readily if desirable. The window is shielded, except for a $\frac{1}{4}$-inch-diameter center portion, by a primary collimator between the window and the source, but if the window is damaged it can easily be removed and replaced. The primary collimator serves also to restrict x-radiation into the chamber to an area where scattering can be contained.

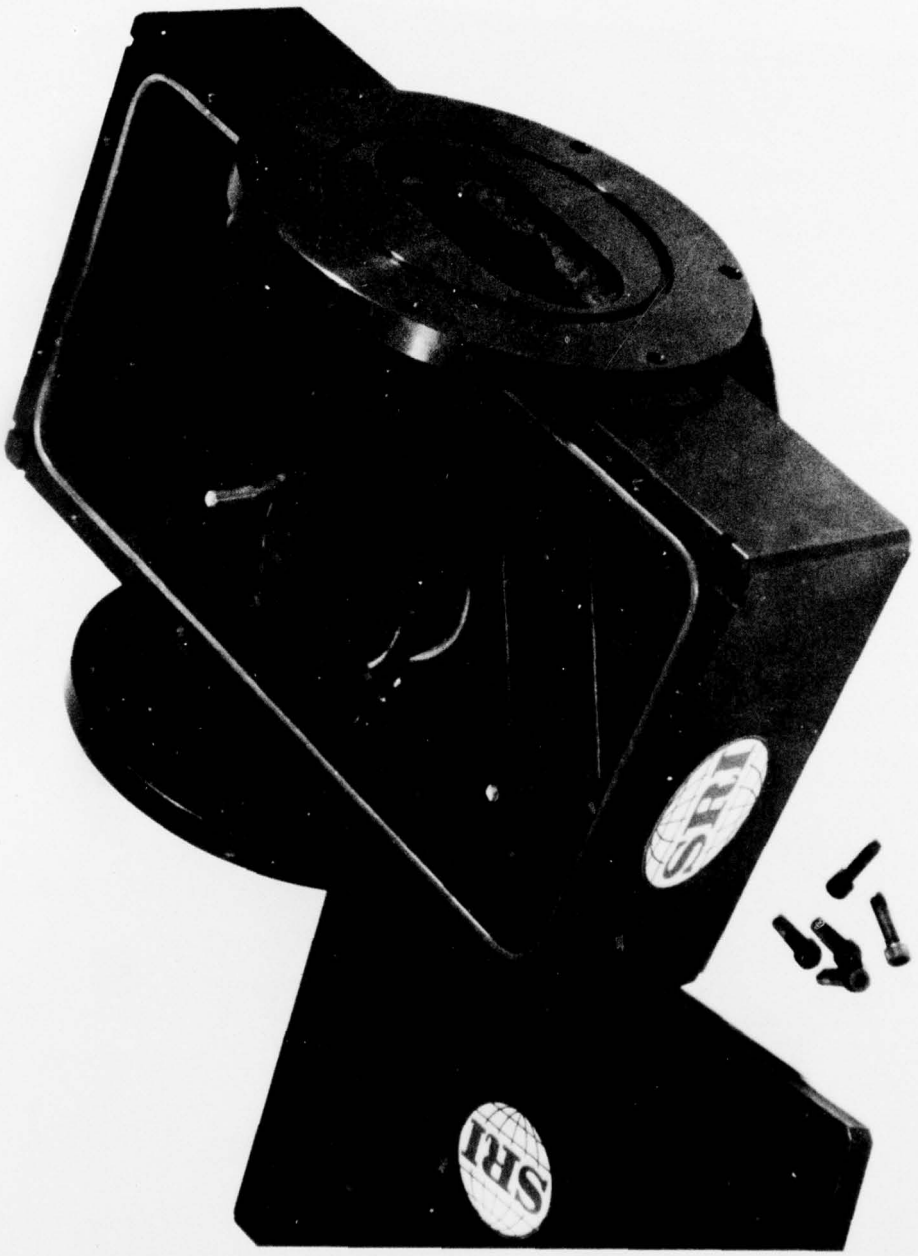
The main collimator assembly is located directly behind the light tight window. The irradiated area is defined by two 3/16-inch-diameter apertures 5/8-inch apart in tandem in a cylindrical housing 1 inch long.



1	Comm. Item	#10-32 x 3/4 Hex. Hd. Cap Screw	12
2	Comm. Item	South Co. #67 Retractable Screw	2
3	Comm. Item	O'Ring - 1/8 Custom Fit	1
4	Comm. Item	O'Ring #2-244	1
5	C-3251-13	Cover	1
6	D-3251-8	Housing	1
7	B-3251-14	X-Ray Trap	2
8	Comm. Item	#4-40 x 3/16 Fill. Hd. Mach. Screw	8
9	Comm. Item	#6-32 x 3/8 Bind. Hd. Mach. Screw	8
10	C-3251-2	Mounting Plate	2
11	C-3251-3	Film Holder	2
12	B-3327-9	Film Retainer	2
–	B-3251-5-A	Alt. Film Retainer	2
13	Comm. Item	#6-32 x 3/16 Bind. Hd. Mach. Screw	4
14	Comm. Item	1/8 Dia. x 1/4 Lg. Dowel Pin	4
15	Comm. Item	1/4 Dia. x 3/4 Lg. Spacer - #8-32 Th'd	4
16	Comm. Item	#8-32 x 5/8 Set Screw	4
17	Comm. Item	#6-32 x 11/16 Sock. Hd. Cap Screw	2
18	A-3251-16	Crystal Retainer	4
19	Comm. Item	#4-40 x 1/4 Fill. Hd. Mach. Screw	4
20	A-3251-9	Collimetor Holder	2
21	A-3251-10	Collimetor	2
22	A-3251-12	Primary Collimetor	2
23		Light Tight Window	2
24	Comm. Item	O'Ring #2-020	2
25	B-3251-15	Crystal Holder	2
26	B-3251-11	Crystal Positioner	2
–	Comm. Item	#4-40 x 1/4 F.N. Mach. Screw	2

MA-3251-3

FIGURE 7 SCHEMATIC OF MSN SPECTROGRAPH



MP-3251-4

FIGURE 8 MSN SPECTROGRAPH

PRECEDING PAGE BLANK-NOT FILMED

The forward end of the cylinder projects into the chamber wall to within about $\frac{1}{4}$ inch of the primary collimator. Its inside diameter is large enough to trap any x-radiation coming through the primary collimator. Secondary scattering to sensitive regions of the spectrograph is inhibited by the encircling chamber wall.

The base of the curved crystal mount is designed with three degrees of freedom (axial, transverse, and rotational) to permit maximum utilization of the crystal surface. The x-ray trap is a thin walled rectangular box at the rear of the chamber in line with the collimator and crystal assemblies. It can be adjusted transversely so that its side wall on the film plane side coincides with the edge of the radiation zone.

The film holder assembly is designed to hold a film strip on either of two surfaces. One is curved with a 4-inch radius (centered on the crystal mount) forming an arc through about 80^{o}; the second is a $2\frac{1}{2}$-inch-long plane surface $1\frac{1}{4}$ inches from the center of the crystal mount and forming an angle of 45^{o} with the collimated beam axis. The film strip, on either surface, can be adjusted laterally for proper positioning with respect to the irradiated zone. The film holder assembly is positioned precisely by dowel pins and held in place by a captive knurled knob. It can be removed and replaced without the use of tools and without disturbing its alignment or that of any other components.

The two film planes allow a trade-off between resolution and sensitivity. If the x-ray output of the source is sufficient for adequate exposure of the film, the rear film plane will be used. If initial experiments show that the x-ray output is insufficient, use of the film

plane nearest the crystal will give approximately a threefold increase in sensitivity with a corresponding decrease in resolution.

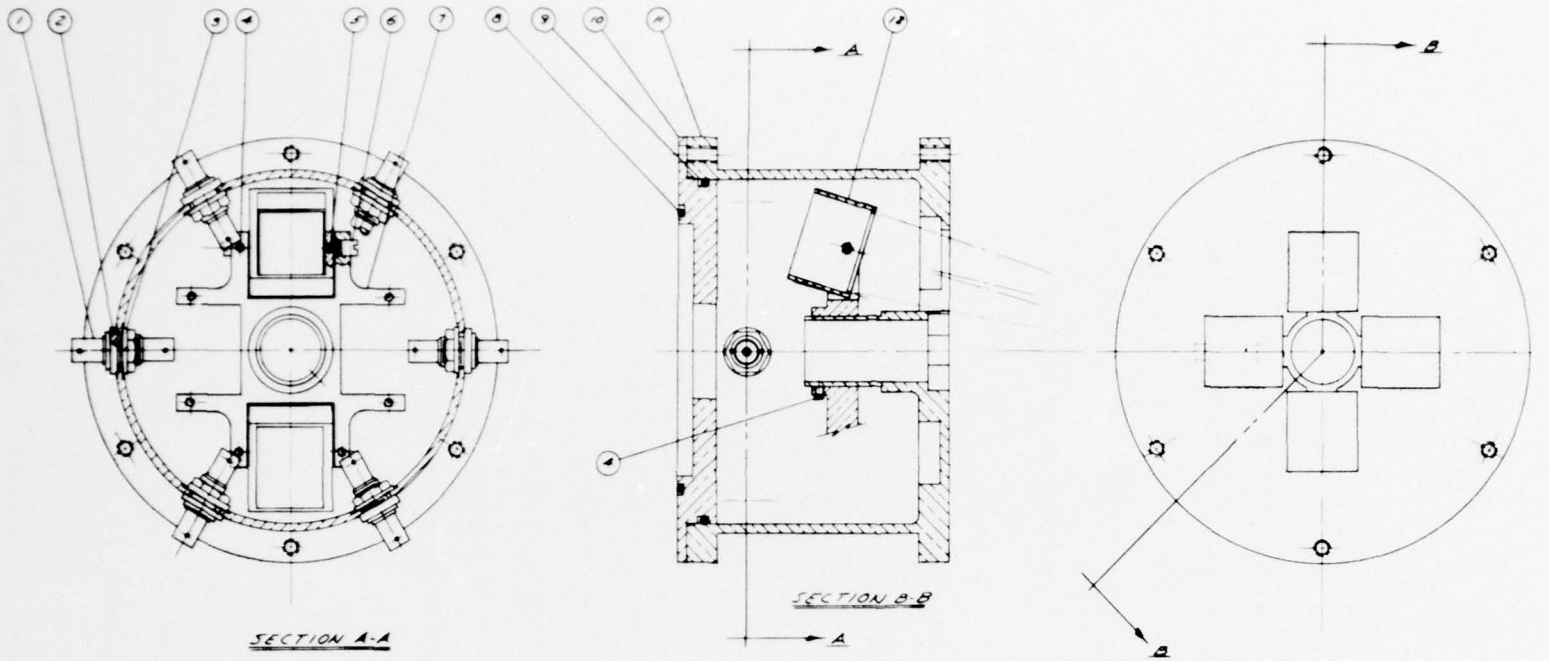
The base plate to which all the basic components are attached is supported at four points by machine screws in threaded holes to provide vertical adjustment and leveling. The pivot point for rotational alignment is a dowel pin located under the collimator assembly. When the plate has been positioned properly, it is locked in place by two adjustable fasteners threaded into the base of the chamber.

All aluminum parts were black anodized and steel parts blackened to inhibit light reflection.

Thermopile Calorimeter Assembly

The thermopile calorimeter assembly is shown schematically in Figure 9, and a photograph of the completed unit with two mounted thermopile calorimeters is shown in Figure 10. The assembly comprises a vacuum-tight cylindrical housing, 6-3/4-inch diameter overall by $4\frac{1}{2}$ inches long, enclosing a mounting ring to accommodate four detectors with provisions for adjusting each unit independently. The sealing surface at each end of the housing is compatible with the matching surface of the existing MSN units, and six hermetically sealed BNC type bulkhead adapters (UG 492 D/U) are provided. The outer shells of the adapters are insulated from the chamber walls, providing 12 conductors each insulated from all the others.

As in the spectrograph assembly, an unobstructed pass-through is provided for the laser beam, and the detectors are mounted off axis in a symmetrical four-station array. Each station is irradiated through a separate port in the forward wall of the chamber. Although each detector can be rotated to face any point on the axis from zero to infinity, the limit on port size imposed by the O-ring seal in the matching flange restricts the effective range for complete exposure of the thermopile

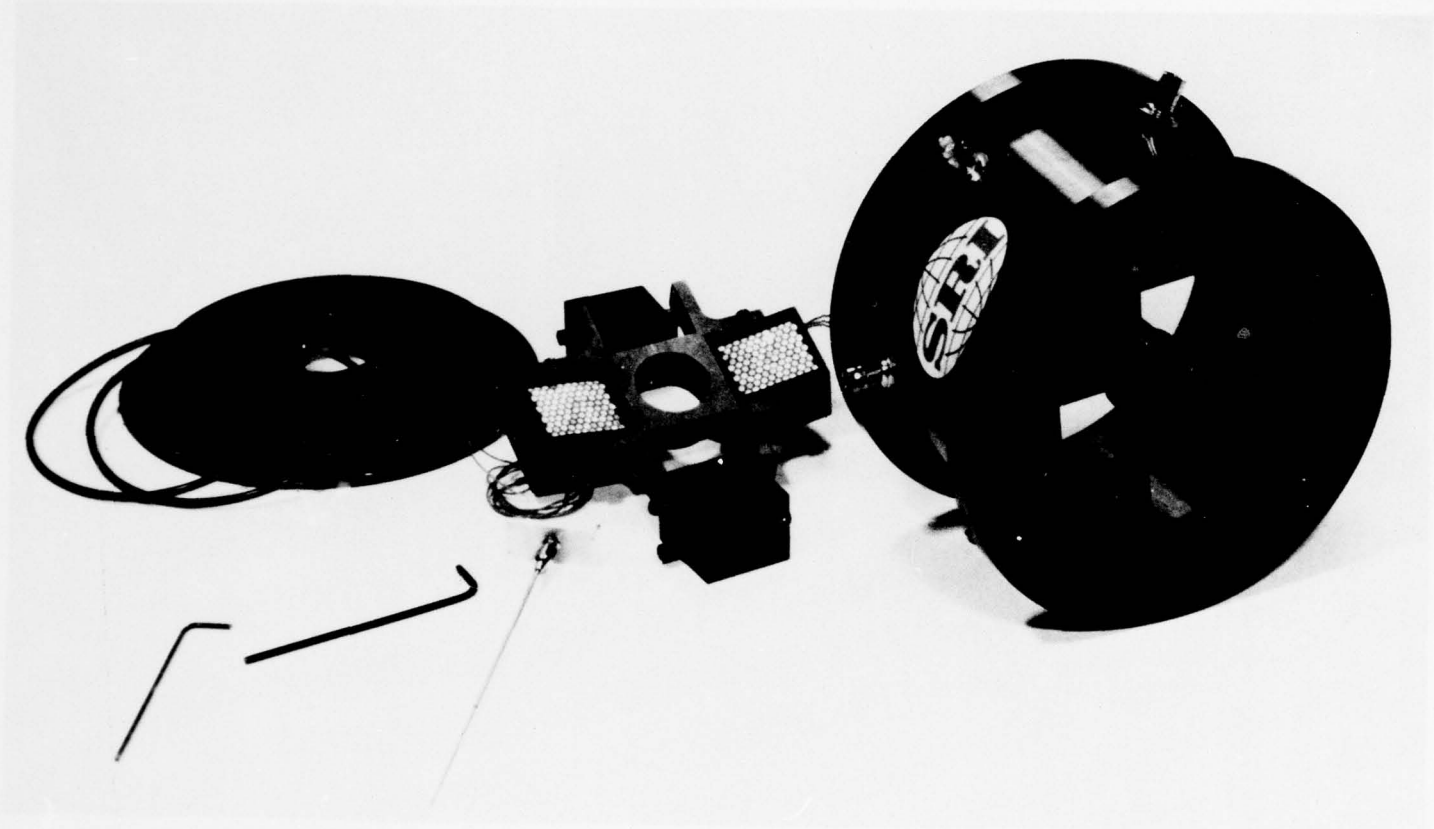


1	Comm. Item	Bng. Adapter #KC-99-38	6
2	B-3251-105	Seal Ring (O'Ring #2-016)	6
3	B-3251-105	Insulating Washer	6
4	Comm. Item	#6-32 x 1/4 Set Screw	9
5	Comm. Item	#8-32 x 3/8 Set Screw	8
6	Comm. Item	1/4 Dia. x 3/8 Lg. Spacer - #8-32 Int. Th'd	8

7	C-3251-101	Cassette Mounting Ring	1
8	Comm. Item	O'Ring #2-244	1
9	Comm. Item	O'Ring #2-252	1
10	C-3251-103	Seal Ring	1
11	C-3251-104	Housing	1
12	A-3251-102	Thermopile Cassette	4

MA-3251-5

FIGURE 9 SCHEMATIC OF MSN THERMOPILE CALORIMETER ASSEMBLY



MP-3251-6

FIGURE 10 MSN THERMOPILE CALORIMETER ASSEMBLY

detectors from a minimum of about 2 inches to a maximum of about 8 inches ahead of the housing. This range can be extended by blanking off a known portion of the detector surface area and compensating the response curve accordingly.

A fixture has been provided for manually aligning each detector station separately.

29

SUMMARY AND RECOMMENDATIONS

A curved crystal spectrograph with provision for the simultaneous use of two crystals was designed and provided to MSN. The delivered instrument contained a KAP crystal curved to a 1.25-inch radius of curvature.

A thermopile calorimeter assembly was also prepared for MSN use. This instrument has provisions for four thermopile calorimeters along with Ross or K-edge filters for the calorimeters. The calorimeter mounts can also accommodate active detectors such as the RCA scintillator-photomultiplier detectors currently in use at MSN. Two 100-junction thermopile calorimeters with 0.002-inch-thick gold absorbers were supplied in the calorimeter assembly.

SRI staff visited MSN and participated in instrument installation and initial experimentation. However, since the instrumentation will be used for continuing experimentation by MSN and supplemented by other measurements, the results of the x-ray measurements will be reported separately by MSN.

If progress in the development of the laser-augmented theta pinch x-ray source warrants more detailed x-ray measurements, it is recommended that the instrumentation described here be supplemented with:

- A second crystal, either graphite or LiF, to enable measurements over an extended x-ray energy range.
- Two additional thermopile calorimeters with K-edge or Ross filters to enable accurate band spectral measurements.
- A pinhole plate and film plane that could be substituted in the spectrograph for either of the curved-crystal collimator platforms to enable spatial resolution of the plasma x-ray source.

DISTRIBUTION LIST

DEPARTMENT OF DEFENSE

Defense Documentation Center
Cameron Station
12 cy ATTN: TC

Director
Defense Intelligence Agency
ATTN: DTICI, Robert I. Rubenstein

Director
Defense Nuclear Agency
3 cy ATTN: STTL, Te h. Library
ATTN: STSI, Archives
ATTN: RAEV
ATTN: STVL
ATTN: DDST

Dir. of Defense Research & Engineering
Department of Defense
ATTN: S&SS (OS), John B. Walsh
ATTN: George R. Barse

Commander
Field Command
Defense Nuclear Agency
ATTN: FCPR

Director
Interservice Nuclear Weapons School
ATTN: Doc. Con. for LTC Byfield D. Gordon

Chief
Livermore Division, Field Command, DNA
Lawrence Livermore Laboratory
ATTN: FCPRL

DEPARTMENT OF THE ARMY

Chief C-E Services Division
US Army Communications Command
ATTN: CEEO-7, Wesley T. Heath, Jr.

Commander
Harry Diamond Laboratories
ATTN: DRXDO-RBH, Stewart S. Graybill
ATTN: DRXDO-TI, Tech. Lib.
ATTN: DRXDO-NP

Commander
US Army Foreign Science & Tech. Center
ATTN: P. A. Crowley

Commander
US Army Materiel Dev. & Readiness Command
ATTN: DRCDE-D, Lawrence Flynn

Commander
US Army Nuclear Agency
ATTN: ATCN-W, LTC Leonard A. Sluga

Commander
US Army Test & Evaluation Command
ATTN: DRSTE-EL, Richard I. Kolchin

DEPARTMENT OF THE NAVY

Director
Naval Research Laboratory
ATTN: Code 7750, J. Davis
ATTN: Code 7701, Jack D. Brown
ATTN: Code 2627, Doris R. Folen
ATTN: Code 7770, Gerald Cooperstein

Commander
Naval Surface Weapons Center
ATTN: Code WR43
ATTN: Code WA501, Navy Nuc. Prgms. Off.
6 cy ATTN: Code WX21, Tech. Lib.

DEPARTMENT OF THE AIR FORCE

AF Weapons Laboratory, AFSC
ATTN: CA, Arthur H. Guenther
ATTN: SUL
ATTN: DYS, W. Baker

ENERGY RESEARCH & DEVELOPMENT ADMINISTRATION

University of California
Lawrence Livermore Laboratory
ATTN: John Nuckolls, A Div. L-545
ATTN: Tech. Info., Dept. L-3

Los Alamos Scientific Laboratory
ATTN: Doc. Con. for J. Arthur Freed
ATTN: Doc. Con. for Donald R. Westervelt

Sandia Laboratories
ATTN: Doc. Con. for 3141 Sandia Rpt. Coll.
ATTN: Doc. Con. for 5240, Gerald Yonas

OTHER GOVERNMENT AGENCIES

Department of Commerce
National Bureau of Standards
ATTN: Sec. Officer for Appl. Rad. Div.,
Robert C. Placious

DEPARTMENT OF DEFENSE CONTRACTORS

Aerospace Corporation
ATTN: Richard Crolius, A2-Rm. 1027
ATTN: V. Josephson
ATTN: S. P. Bower
ATTN: R. Mortensen
ATTN: Library
ATTN: J. Benveniste

Battelle Memorial Institute
ATTN: David A. Dingee

The Boeing Company
ATTN: Aerospace Library

Charles Stark Draper Laboratory, Inc.
ATTN: Kenneth Fertig

PRECEDING PAGE BLANK-NOT FILMED

DEPARTMENT OF DEFENSE CONTRACTORS (Continued)

General Electric Company
TEMPO-Center for Advanced Studies
ATTN: DASIAC

Jaycor
ATTN: Eric P. Wenaas

M. I. T. Lincoln Laboratory
ATTN: Leona Loughlin, Librarian, A-082

Mathematical Sciences Northwest, Inc.
ATTN: Alan L. Hoffman
ATTN: Edward A. Crawford

Maxwell Laboratories, Inc.
ATTN: Alan C. Kolb
ATTN: Peter Korn

DEPARTMENT OF DEFENSE CONTRACTORS (Continued)

Mission Research Corporation
ATTN: Conrad L. Longmire

Mission Research Corporation-San Diego
ATTN: V. A. J. Van Lint

Physics International Company
ATTN: Doc. Con. for Philip W. Spence
ATTN: Doc. Con. for Ian D. Smith
ATTN: Doc. Con. for Sidney D. Putnam
ATTN: Doc. Con. for Charles H. Stallings

Pulsar Associates, Inc.
ATTN: Carleton H. Jones, Jr.

R & D Associates
ATTN: Leonard Schlessinger

Science Applications, Inc.
ATTN: Nelson Byrne

Simulation Physics, Inc.
ATTN: Roger G. Little

Systems, Science & Software, Inc.
ATTN: Andrew R. Wilson

Texas Tech. University
ATTN: Travis L. Simpson